Wave transmission through permeable structures in Demak Indonesia

A design study with the numerical model SWASH

M. Alferink

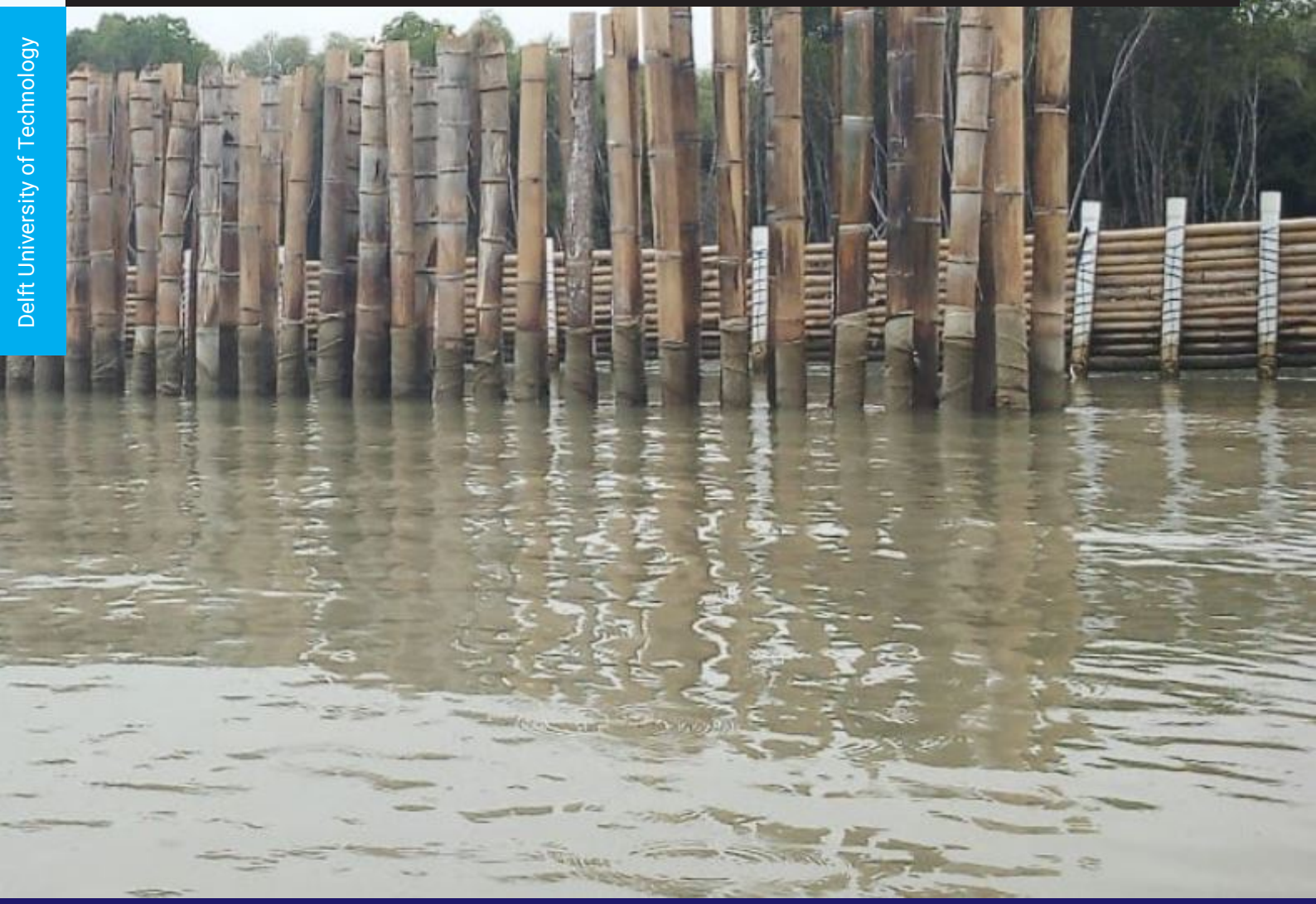

Delft University of Technology

TU Delft Delft University of Technology

Challenge the future

Wave transmission through permeable structures in Demak Indonesia

A design study with the numerical model SWASH

by

M. Alferink

To obtain the degree of Master of Science
at the Delft University of Technology,
to be defended publicly on Wednesday January 12, 2021 at 02:30 PM.

Student number: 4744799

Project duration: February 31, 2021 – January 12, 2022

Thesis committee:

ir. Alejandra Gijon Mancheno ,	TU Delft, daily super visor
Prof. dr. ir. Ad Reniers ,	TU Delft, chair
Prof. dr. ir. Han Winterwerp ,	TU Delft
Ass. Prof. dr. ir. Bas Hofland ,	TU Delft
Dr. ir. Tomohiro Suzuki,	Flanders Hydraulics Research

TU Delft

Preface

This thesis is the last part of my study at the TU Delft, which started in Arnhem nine years ago with my bachelor at the HAN. Actually it started a bit earlier, as a little boy I liked to build dams in small creeks and this curiosity in understanding the interaction of natural flows with structures eventually lead me to this thesis. I really enjoyed the subject and modelling work that came along with, which was sometimes frustrating but eventually worked out.

This thesis would not have been possible without the effort of some people who helped me along the way. First of all, I want to thank Alejandra Gijón Mancheno who was my daily supervisor during my thesis. In our weekly meetings we discussed a lot about how to improve and interpret the results, you always came up with a useful hint to improve it. Thanks for all effort and time you put into it, it really improved the report. I also want to thank my chair Ad Reniers for the guidance during my thesis and the feedback you gave on my report, it really improved the structure of the report. Next to this I want to thank my other committee members, who each guided me in their own field of expertise. I want to thank Tomohiro Suzuki for all questions I could ask about SWASH and guiding me with the processing methods. I want to thank Bas Hofland for discussions about the designs and the useful feedback on my report. I want to thank Han Winterwerp who helped me to understand the conditions in Demak better.

Further, I want to thank my study friends as doing my thesis during Covid times was not easy, but I could always rely on you during my thesis and other parts of my study.

Last but not least, I want to thank my family for their support and believe in me during my study. Thanks for giving me feedback and doing a grammar check even when it was not your cup of tea. I want to thank Erik Scherpbier for motivating me to choose Civil Engineering, I really liked that trip on the back of your motorbike along the Delta works. I specially want to thank my girlfriend Fay who supported me through my thesis and with whom I could discuss anything at anytime.

Marijn Alferink

Delft, January 2022

Summary

The coastline of Demak, Indonesia has been eroded during the last 15 years. To restore the natural coastal protection which existed out of mangroves forest, permeable dams, consisting of bamboo poles with a brushwood filling, have been built to attenuate the waves and facilitate sedimentation behind the dams and thus creating a habitat for mangroves. However these designs required a lot of maintenance, so a new type of design is proposed without a filling of brushwood, containing only vertical bamboo poles. Next to this the possibility to include aquaculture in the design is proposed.

Therefore this study assesses the wave transformation by the new designs in Demak, Indonesia with the numerical wave model SWASH. In order to do that first the hydrodynamic conditions are analyzed to obtain the design conditions for the structures, and then SWASH is validated against laboratory experiments to find the right drag coefficient values.

The design wave conditions are based on the local water depth, offshore wave heights and periods and local bathymetry. The offshore waves are based on a dataset from WaveWatch III, which compares well with measurements of a local storm event. The dataset of WaveWatch III is filtered and extrapolated to determine the wave conditions for return periods(R) of 1 and 5 years. This resulted in offshore waves with H_{m0} = 2.08 and 2.39 m, and T_p = 6.9 and 7.5 s respectively. The water level is mainly influenced by the tidal elevation and the surge levels. The surge levels are obtained from a risk assessment of the coast of North Java (Willemsen et al., 2019), which vary between 0.63 to 0.68 m for R = 1 and 5 years respectively. The tidal levels are determined using the water depth measurements of two transects from Van Domburg et al. (2018) and analysed with Matlab tool Utide by Codiga (2011), resulting in a spring tidal range of 85 cm and a neap tidal range of 50 cm.

Four different configurations from the experiments of Jansen (2019) are used to validate SWASH: single row, longitudinal(the spacing in flow direction is longer than the lateral spacing), open uniform and dense uniform configuration. These configurations are modelled in the numerical wave model SWASH by use of the vegetation module. The most influential factors are: the drag coefficient, the way to describe mass conservation and the number of stems(cylinders) per m^2. For the drag coefficient the bulk drag coefficient of Gijon Mancheno et al. (2021) is used, which contains factors for sheltering, blockage and the KC state of the flow. For the densely packed configurations the bulk drag coefficient proved to have a better agreement than the drag coefficient of a single cylinder. The sensitivity to the number of stems per m^2 is small when implementing the longitudinal configuration as an average amount of stems per m^2 or by specifying the individual rows of the configuration and so locally increasing the number of stems. Three methods of describing the mass conservation in SWASH are evaluated: by means of a cross sectional approach that is expressed by the blockage factor in the bulk drag coefficient Gijon Mancheno et al. (2021), by a volumetric approach due to activating the porosity in SWASH which means that the blockage factor cannot be included in the drag coefficient and by a combination of these two. For the longitudinal configuration the best agreement is found the cross sectional approach and for the single row configuration the best agreement is found by the volumetric approach.

Once SWASH is validated, the designs of several structures are investigated. Firstly, a design consisting out of two rows of bamboo poles is considered where the spacing between the rows is varied to find an optimum distance. The transmission rate E_t/E_i decreased from 75% to 55% with a spacing s_x = 0.42 m to 5.8 m, larger spacings did not result in less transmission. If one wants to be conservative at least three rows are needed to have a lower transmission rate of 50 %. When mussels are considered, the structures have to be placed in deeper water as mussels can only grow between MLWS and 40 cm above the bed. To provide enough space for mussel growth, the poles have to be placed more sparsely. The effect of a larger water depth in combination with a limited pole length and sparse structures is larger than the extra drag and frontal area provided by mussels, especially since they did not cover the whole pole length, and resulted in high transmission rates. It is thus recommended to, or place a high number of rows of mussel poles or place a few rows without mussels followed by poles for mussels. This decision however also depends on benefits that mussel poles may bring and the cost of the materials, therefore a cost/benefit analysis is required.

This thesis found an efficient design that can be used in reducing wave attenuation along muddy coasts without the need of a brushwood filling. Hereby it provides an economically and user friendly alternative with respect to the current design, as it requires less material and maintenance.

Contents

List of Figures

List of Tables

List of Symbols

α	Proportionality parameter	-
α_d	damping factor (Dalrymple et al., 1984)	-
α_z	Fraction of a certain layer over the water depth	-
α_{bot}	Bottom slope	-
$\Delta\theta$	Directional spreading of waves	°
η	Surface elevation	m
γ	Breaking parameter	-
ν	Kinematic viscosity	m^2/s
ρ	Density	kg/m^3
σ	Radian frequency	rad/s
τ	Shear stress	N/m^2
θ	Wave direction	°
ζ	Water surface	m
A	Area	m^2
a	Wave amplitude	m
b	Spacing of the plants	m
b_v	Vertical spacing between plants	m
c	Wave celerity	m/s
C_D	Drag coefficient	-
c_g	Wave group celerity	m/s
C_M	Inertia coefficient	-
C_m	Added mass coefficient	
$c_{b.fr.}$	Bottom friction coefficient	$s/m^{1/3}$
$C_{d,b}$	Bulk drag coefficient	-
$C_{d,s}$	Drag coefficient for a single cylinder	-
D	Diameter	m
D_e	External diameter	m
e	Relative roughness height	-
E_d	Dissipated wave energy	-
E_i	Incident wave energy	-
E_r	Reflected wave energy	-
E_t	Transmitted wave energy	-

f	Frequency	Hz
f_b	Blockage factor	-
F_d	Drag force	N
f_s	Sheltering factor	-
f_{KC}	KC factor	-
g	Gravitational constant	m/s^2
H	Wave height	m
h	Water depth	m
H_0	Incident wave height before vegetation	m
H_{m0}	Significant wave height	m
k	Wave number	1/m
K_d	Dissipation coefficient	-
K_r	Reflection coefficient	-
K_t	Transmission coefficient	-
K_v	Damping factor	-
KC	Keulegan-Carpenter number	-
L	Wavelength	m
L_p	Peak wave length, belonging with the peak wave period	m
n	Porosity	-
n	Wave group number	-
N_s	Number of storms	Storms/yr
N_v	Number of stems with a horizontal orientation	Stems
N_{stems}	Number of stems with a vertical orientation per m^2	$Stems/m^2$
N_{Ursell}	Ursell number	-
q	Specific discharge	m^2/s
R	Return period	year
Re	Reynolds number	-
s	Height of vegetation above the bottom	m
s_0	Wave steepness	-
s_x	Center to center spacing in flow direction	m
s_y	Center to center distance perpendicular to flow direction	m
T	Wave period	s
t	time	s
T_p	Peak wave period	s
$T_{1/3}$	Significant wave period	s
$U10$	Wind velocity at a height of 10 m above the water surface	m/s
u	Flow velocity	m/s

u_∞	Undisturbed flow velocity	m/s
U_{wind}	Wind velocity in x direction	m/s
u_w	Flow velocity under a wave	m/s
V_{wind}	Wind velocity in y direction	m/s
x	Position	m
ü	Flow acceleration	m/s^2

1 Introduction

1.1. Problem definition

Mangroves can be found on muddy coasts in the tropics around the world and offer various ecosystem services such as water quality improvement and coastal protection (Barbier et al., 2011), (Temmerman et al., 2013), as is illustrated in Figure 1.1. Mangroves attenuate waves (Quartel et al., 2007) and trap sediment between their roots. Therefore they mitigate coastal erosion and protect the hinterland from flooding.

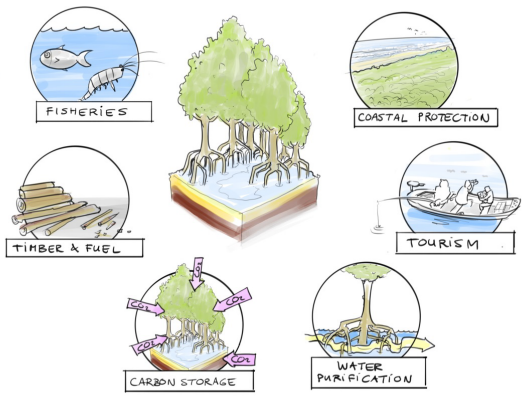

Figure 1.1: The ecosystem services that a mangrove forest could provide (Tonneijck et al., 2015)

Over the past decades mangrove areas have been deforested for aquaculture such as fish ponds and shrimp farms (Hamilton & Casey, 2016), which reduces the protective effect. This study focuses on a location at the coast of Demak, Java, Indonesia, which was largely deforested during the 20th century. Extensive groundwater extraction in the nearby city of Semarang causes high subsidence rates in the area (Abidin et al., 2013). As a consequence the coast has retreated several hundreds of meters, as is shown in Figure 1.3.

Restoration

At deforested coastlines, the loss of mangroves can result in a retreating coastline. Restoring the vegetation requires reducing wave action, ensuring there is a flux of sediment towards the coastline, and enhancing trapping in a natural way (Winterwerp et al., 2013). Furthermore, if human interventions have altered the hydrology, it should also be restored. Also if the seedling availability is low planting could be considered (Winterwerp et al., 2013).

In attempts to restore the original ecosystem, mangroves have been replanted at locations where they once stood. However, the restoration schemes have had mixed results (Primavera & Esteban, 2008; Kodikara et al., 2017). These mixed success rates have been attributed to not considering the ecological requirements of mangrove species (Lewis, 2005). Mangroves grow at the intertidal area, in brackish water and with limited wave action (Lewis, 2005), and if human action or natural action have altered such parameters, they should be restored to enable vegetation recovery.

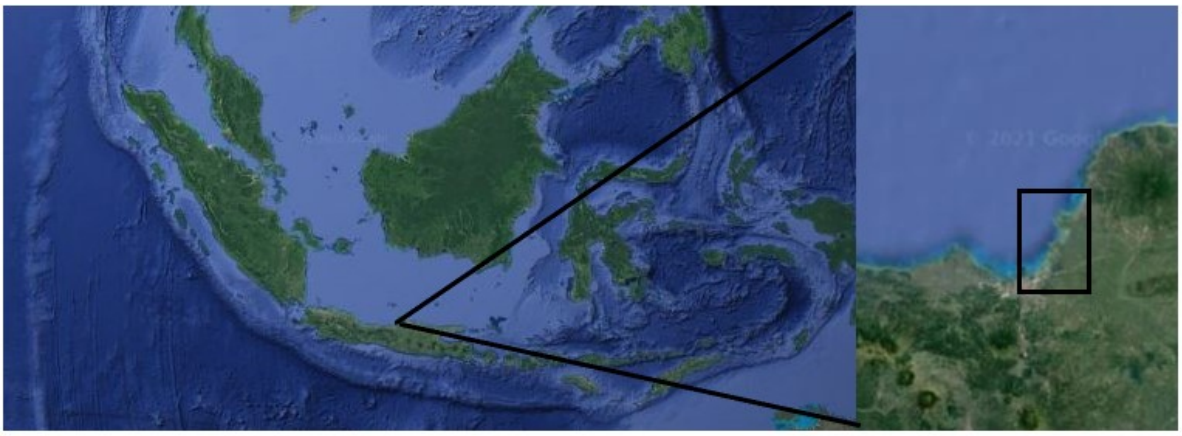

Figure 1.2: Indonesia with on the right the coast of Demak on the island of Java. From Google Earth, available via https://earth.google.com/web and accessed at 3-12-2021

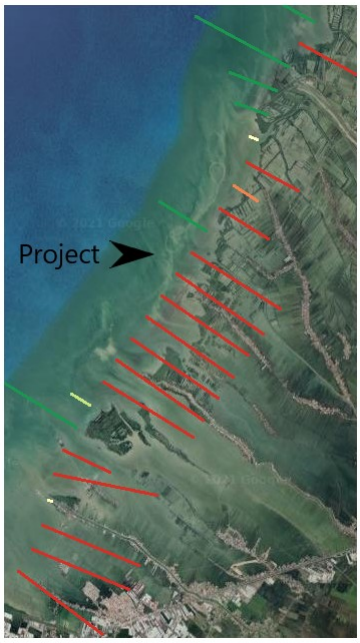

Figure 1.3: The red bars present erosion (3 m/yr or more) and the green bars present accumulation of sediment (3 m/r or more).The retreat of the coast in the period of 1985 - 2016 in the Aquamonitor available via https://aqua-monitor.appspot.com/?datasets=shoreline.

For successful restoration of the coastline several factors need to be considered. Winterwerp et al. (2013) suggests the following strategy:

1. Restore the onshore flux of sediment
2. Enhance trapping of fine sediment in a natural way
3. Reduce wave heights
4. Restore hydrological conditions
5. Plant proper mangroves species if there is no natural propagule present

In 2013 a Building with Nature Pilot was started in Demak, Indonesia in which structures were built to enhance mangrove restoration, an idea inspired by the brushwood dams that have been applied for centuries in NW Europe to trap sediment and gain land from the sea (Winterwerp et al., 2020).

In a healthy muddy mangrove coast the sediment balance is determined by the tidal and wave forcing. In general the waves stir the sediment (mud) up and the tides transport it on- or offshore. The large waves stir up the sediment in the foreshore whereas small waves only stir up sediment near the shoreline. Due to this, large waves can erode sediment from deeper areas, which is then deposited by the tide at the nearshore, whereas small waves only cause erosion near the shoreline.

The permeable structures in Demak, Indonesia were built to attenuate waves but without blocking the sediment transport by the tide. These structures cause an initial 50 cm of accretion but the subsidence rates in the area were too high to be compensated (Winterwerp et al., 2020). These permeable dams are made out of bamboo poles and filled with brushwood as is shown in Figure 1.4.

Figure 1.4: Sideview of permeable dam filled with brushwood. With on the left sheltered area and on the right is the open sea. From Winterwerp et al. (2020)

Since the start of the pilot in 2013 the structures have been updated with new materials and different configurations. As the bamboo poles were being eaten by shipworm, poles made out of pvc and filled with concrete were tested in 2016. Also the brushwood filling has been adjusted, as it deteriorated fast, with a wrapping of old nets and ropes around the bundles of brushwood to extend the lifetime (Tonneijck et al., 2015).

MuMaCo project

A new pilot study will be conducted in Demak, Java, Indonesia from the village of Timbulsloko see Figure 1.5, this is called the MuMaCo project (Mud Mangrove Coast). In this area multiple structures will be tested, to investigate the performance in terms of wave damping and aquaculture. This thesis is part of the MuMaCo project and investigates some of the structures they proposed.

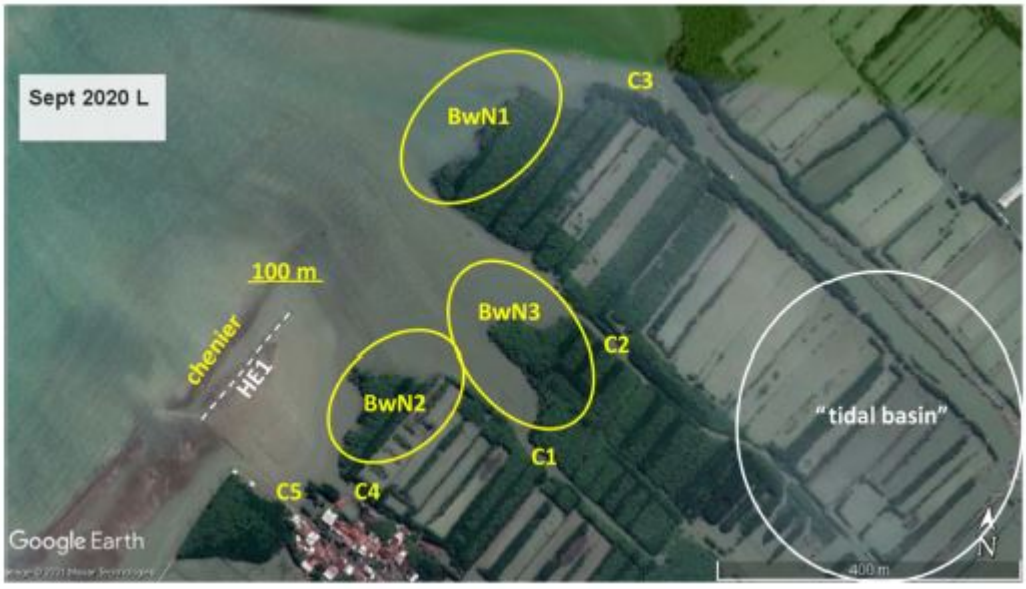

Figure 1.5: MuMaCo project area, showing in the left corner the village of Timbulsloko. The three yellow circles area the test areas, due to budget limitations only BwN1 will be used.

Four types of configurations are proposed, combining wave damping and aquaculture:

1. Bamboo fences: a fence consisting out of vertical poles in one or multiple rows without mussels
2. Mussel poles: bamboo fences with a mussel growth on the poles
3. Long and/or shortline: vertical poles with ropes in between where the mussel culture is attached to
4. Compound structure: vertical concrete-filled pvc piles with horizontal bamboo bars in the intertidal area, below low water space for mussel cultures.

This thesis investigates the first two designs: the bamboo fences and the mussel poles.

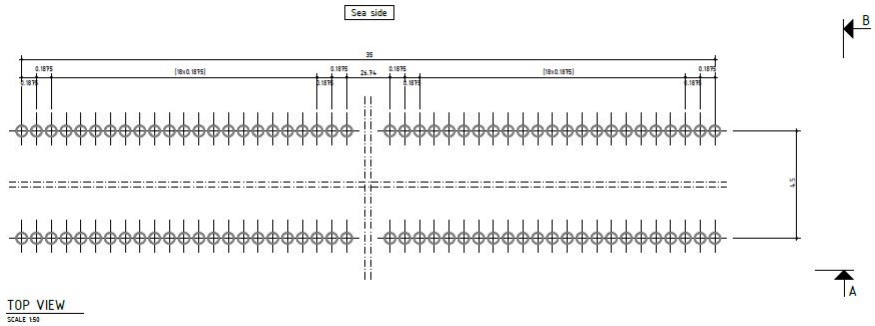

Figure 1.6: Top view of the bamboo fence configuration as proposed by the design team of the MuMaCo project, consisting out of two rows of bamboo poles.

Aquaculture and wave dissipating structures

An important part of the restoration of the mangroves by the Building with Nature consortium is to support a sustainable way of living for Demak community. In such, restoration of the mangroves is combined with developing an aquaculture that is sustainable for its surroundings (Tonneijck et al., 2015). A recent study by Rejeki et al. (2021) shows that the introduction of a new type of aquaculture, the production of green mussels, is feasible at the Demak coast.

Optimisation of wave dissipation

To obtain calm water where sediment can settle a certain amount of wave energy has to pass the structures to transport the sediment there. There is no specific information about which amount of energy has to be transmitted through the structures to transport enough sediment. However there is a field measurement campaign carried out in Vietnam which has comparable circumstances (Albers et al., 2013). They reported transmission coefficients of K_t =0.7-0.8 for submerged stiff brushwood structures and 0.5-0.6 for emerged structures, where K_t is defined as $K_t = H_t/H_i$. It resulted in a sedimentation of 17 centimeters after 7 months. In terms of energy this gives transmission rates of E_t/E_i = 50 - 64 % for submerged cases and 25 - 36 % for emerged cases.

The experiments of Haage (2018) and Jansen (2019) suggested that rows of bamboo poles without a filling can maximise the dissipation per element depending on the separation in the wave direction. In order to fully optimize the designs the optimal distance between the poles is investigated, furthermore, the effect of a design with multiple rows is examined. The presence of mussels could also change the rates of wave dissipation by the bamboo poles. Excluding the loss of the brushwood filling could not only reduce the maintenance costs but also reduce the material costs compared to the existing designs. Including mussels and removing the brushwood filling could thus reduce the costs of the structure. However, incorporating this changes requires assessing their impacts on the structure performance.

The row separation will not only influence the dissipation but also the interaction between the incoming and reflected waves at the different rows of structure, which in turn may influence the wave dissipation. It is hypothesized that for a row separation of a quarter of the wave length, the reflected wave from the second row interacts with transmitted wave behind the first row, therefore resulting in wave resonance which would result in more dissipation and thus less wave transmission behind the second row.

Aside from the wave transmission, the structural stability of the structure is studied as the focus in this thesis is more on the high waves during the NW monsoon as these activate more sediment in the foreshore. However the corresponding hydraulic design conditions were not defined in previous studies.

1.2. Research goal

This section defines the objective of this thesis, and states with which research question this is accompanied.

Objective: This thesis aims to design structures formed by vertical poles, without brushwood filling, combined with mussel aquaculture and therefore investigates how the placement of rows of bamboo poles affects wave dissipation, and what could be the potential effect of integrating mussel growth on the structure performance. It evaluates the wave transmission of the different designs by means of the results of Albers et al. (2013).

Therefore the research question is the following:
Which structure designs consisting of rows of bamboo poles can cause transmission rates of 50 to 64 % of the incident wave energy?

This question is subdivided into several sub-questions:

1. What are the hydraulic design conditions for the structures in Demak, Indonesia?
2. How many rows are needed to have a transmission rate lower than 50 % of the incoming wave energy?
3. How does the reflection between rows change the transmission rates behind the structures?
4. How does the structural stability change for different designs?
5. How much do the mussels contribute to the drag force on a pole and how does this affect the wave transmission of the structures?

1.3. Scope and approach

1.3.1. Approach

There are several knowledge gaps that need to be addressed before the structures can be designed. First of all, the hydraulic design conditions are unknown and to obtain this information, observations from the BioManCo project of waves, water levels and local bathymetry will be used for this purpose. Next to this the performance of the model with which the interaction with the waves will be studied, SWASH, needs to be validated. This will be done with laboratory experiments of Jansen (2019). In Figure 1.7 the consecutive steps are shown that need to be taken to analyse the designs and relate back to the objective of this thesis.

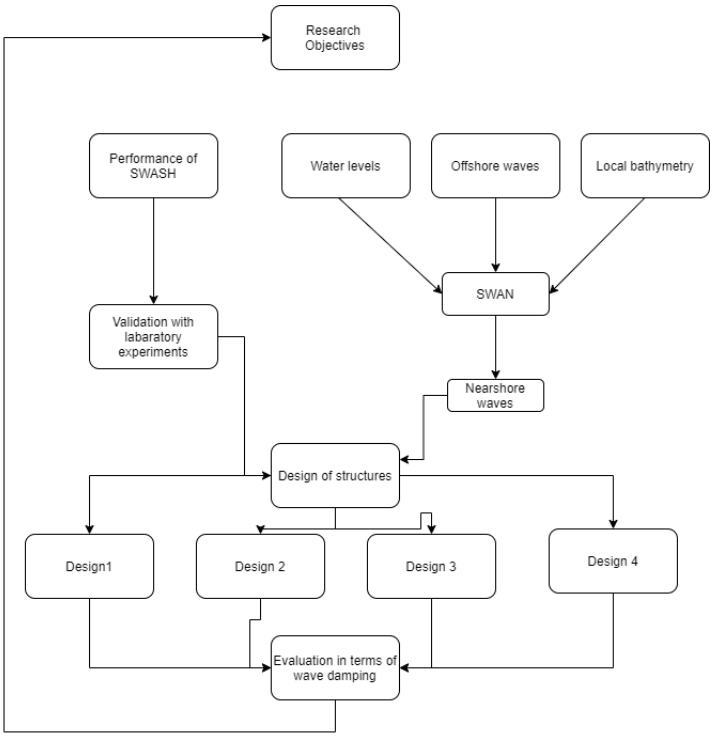

Figure 1.7: Flow chart of this thesis. At this point in the report the research objective is stated and to design the structures SWASH needs to be validated and the hydraulic design conditions needs to be defined.

1.3.2. Scope

The focus of this thesis is on the wave transmission of the different designs. The optimisation of the design would imply an analysis of the costs of the materials and the benefits that the aquaculture may bring, this however falls outside of the scope of this thesis.

The following physical processes are simplified:

- Regular waves are used instead of a full wave spectrum
- The presence of currents is neglected
- The sediment transport itself is not modelled/calculated but represented by the wave transmission
- The bamboo poles are assumed to be rigid and any motion or vibrations are neglected.
- The bathymetry is assumed to be alongshore uniform

2

Literature study

2.1. Introduction

The literature study starts with a description of the wave attenuation by structures in Section 2.2. Then it explains the relation between flow conditions and drag and inertia coefficients in Section 2.2.2. In Section 2.2.3 several approaches that explains wave dissipation by structures are shown. Section 2.2.4 focuses on the effect of the structural configuration on wave dissipation. Section 2.2.5 explains the effect of wave non-linearity on wave dissipation. Section 2.2.7 explains about aquaculture.

2.2. Wave attenuation by structures

2.2.1. Wave interaction with structures

The interaction between waves and a structure can be described in terms of a transfer of energy, which can be described by an energy balance:

$$E_i = E_r + E_t + E_d \tag{2.1}$$

Where:

- E_i is the incident wave energy
- E_r is the reflected wave energy
- E_t is the transmitted wave energy
- E_d is the dissipated wave energy

The energy relates to the wave height according to Equation: E = $\frac{1}{8}\rho g H^2$, where ρ is water density [kg/m^3], g is the gravitational acceleration [m/s^2] and H is the wave height [m]. The terms E_i, E_r and E_t can thus be obtained from the wave height components measured before and after the structure. This requires separating the incident and reflective wave components from the measured surface elevation. The dissipated energy, E_d, cannot be measured and is either obtained by the energy balance, Equation (2.1) or by estimating the hydrodynamic work done by a cylinder, defined as the product of a force acting on a cylinder and the flow velocity. The hydrodynamic forces at a cylinder in a wave flow are often described by the Morison Equation (Morison et al., 1950). These forces consist of a drag component and an inertia component, as is shown in Equation 2.2.

$$F = \frac{1}{2}\rho C_D D u|u| + \rho C_M A \ddot{u} \tag{2.2}$$

Where:

- ρ is the density of water in [kg/m^3]
- C_d is the drag coefficient
- D is the diameter of the cylinder in [m]
- u is the flow velocity in [m/s]

- ü is the flow acceleration in [m/s^2]
- A is the cross-sectional area of the cylinder ($\pi D^2/4$) in [m^2]
- $C_M = C_m + 1$, is the inertia coefficient and C_m being the added mass coefficient

This equation is semi-empirical as the drag and inertia coefficient have to be determined from measurements. The equation does not include diffraction so it only applies for slender structures in such that the diameter is small compared to the wave length: $D/L < 0.05$, where L is the wave length and D is the diameter of the cylinder. The drag coefficient under steady flows depends on the Reynold number (Re).

$$Re = \frac{uD}{\nu} \tag{2.3}$$

Where:

- ν is the kinematic viscosity in [m^2/s]

For Re > 300 the flow develops a fully turbulent wake in steady flows (Sumer & Fredsoe, 2006). The increase in drag on the flow is caused by the vortices in flow regimes with KC>1.1 and the wake that develops for Re > 300 (Sumer & Fredsoe, 2006). Under waves (oscillating flow) C_d also depends on the Keulegan-Carpenter number(KC) which indicates the ratio of drag over inertia forces.

$$KC = \frac{uT}{D} \tag{2.4}$$

Where:

- T is the wave period in [s]

Where for linear waves the flow velocity, u_w, under a wave is the following:

$$u_w = \frac{2\pi}{T}\frac{H}{2}\frac{cosh(k(h+z))}{sinh(kh)} \tag{2.5}$$

Where:

- H is the wave height in [m]
- k is the wave number in [1/m]
- $h + z$ is location of interest in the water column, with z = -h at the bottom and z=0 at the water level

For oscillatory flows, like waves Figure 3.2 of (Sumer & Fredsoe, 2006) shows, for Re = 1000, the different flow regimes that influence C_d and C_m. Sumer and Fredsoe (2006) roughly estimates drag dominance for KC >20-30 and for smaller KC numbers inertia dominance.

Both C_D and C_m have been found to vary with C_D taking values between $C_D = 0.7 - 2.36$, and C_m varying between C_m= 0.70 and 2.60 for a single cylinder (Keulegan & Carpenter, 1958).

2.2.2. Drag and inertia coefficients

Drag and inertia coefficients vary as a function of cylinder arrangement (Etminan et al., 2019), for porous structures (where the porosity varied between n = 0.98 - 0.78 due to the cylinder arrangement) Etminan et al. (2019) identified the processes of blockage and sheltering. Porosity is defined as follows:

$$n = A_c/A \tag{2.6}$$

Where A_c is the conveyance area and A is the total area (including the structure) in [m^2]. On the one hand, relatively smaller lateral spacings cause flow acceleration between cylinders, an effect denoted as blockage. This increase in velocity results in larger hydrodynamic forces acting on the cylinders. If the drag coefficient (also denoted as bulk drag coefficient, C_{db}) is derived from the velocities measured upstream from the array flow acceleration between the cylinders increases, as the local velocity between cylinders is larger than the upstream value. On the other hand, small downstream spacings favour sheltering, which means that downstream cylinders are in the wake of upstream cylinders. Sheltering reduces the velocities acting on downstream elements and decreases their bulk drag coefficient (as sheltering reduces the local velocity compared to the upstream flow). In Figure 2.1 both processes are illustrated. For dense regular cylinder arrays, the net effect on the bulk drag coefficient will depend on the relative size of the lateral and streamwise spacings (Gijon Mancheno et al., 2021). For sparse staggered arrangements with porosities larger than n = 0.78 Etminan et al. (2019) observed that sheltering can be neglected.

Gijon Mancheno et al. (2021) suggests that the bulk drag coefficient can be determined by the factors f_b, f_{KC} and f_s for the range of KC = 10 -21, which describe the effect of blockage, KC state and sheltering, respectively. Their model has the following limitations:

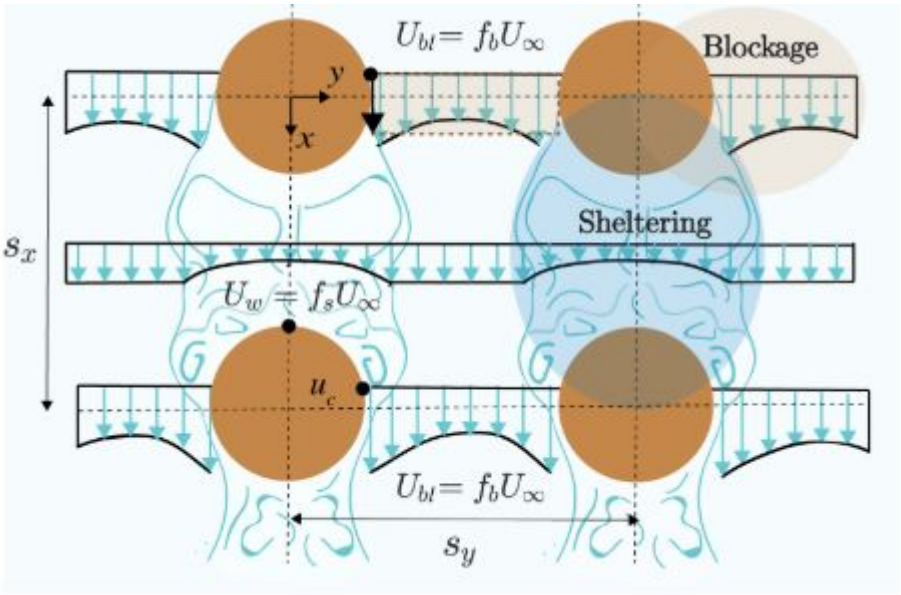

Figure 2.1: Sketch of blockage and sheltering effect (Gijón Mancheño et al., 2021). Where sheltering is the reduction of flow velocity on a downstream cylinder and blockage is the acceleration of the flow due to a constricted flow area. U_b is the flow velocity effected by blockage, f_b is the blockage factor, U_∞ is the unaffected flow velocity in front of the structure, U_w is the flow velocity in the wake of the cylinder, s_x is the center to center distance in flow direction and s_y is the center to center distance in lateral direction.

- to predict c_s a turbulence model is needed, and Gijon Mancheno et al. (2021) provided values that are applicable in a very narrow range of conditions. c_s is an empirical coefficient fitted through the measurement of Jansen (2019) to express the turbulent intensity of the wave conditions
- c_r neglects the influence of varying wave properties, as it is assumed that wave reflection is only a function of the geometry. c_r is an empirical coefficient that is fitted through the experiments of Jansen (2019).
- the wake flow does not describes changes in the flow as function of s_y which would be the case for staggered configurations.

2.2.3. Wave dissipation

Wave dissipation is given by the work done by the hydrodynamic forces on the cylinders. Dalrymple et al. (1984) developed an expression to estimate the wave attenuation through a vegetation field, assuming that:

- the vegetation can be schematized as vertical cylinders
- the flow is undisturbed by the presence of the vegetation
- the flow can be represented by using linear wave theory
- the work done by the skin friction is negligible
- the dissipation is only due to the drag force

The wave attenuation is given by:

$$\frac{H}{H_0} = \frac{1}{1+\alpha_d x} \tag{2.7}$$

Where:

- H_0 is the incident wave height before the vegetation [m]
- α_d is a damping factor
- x is the location inside the vegetation starting from the edge [m]

$$\alpha_d = \frac{2C_D}{3\pi}\frac{D}{b}\frac{H_0}{b}(sinh^3(k(z+h)) + 3sinh(k(z+h))\frac{4k}{3sinh(kh)(sinh(2kh)+2kh)} \tag{2.8}$$

Where:

- b is the spacing of the plants [m]

For the wave attenuation by horizontal orientated cylinders, such as the brushwood filling of some of the structures in Demak, Indonesia, Suzuki et al. (2019) developed an expression which also takes into account the vertical velocities, as unlike for vertical cylinders, the work done by the vertical forces is not negligible for cylinders with a horizontal orientation.

The expression is based on Mendez and Losada (2004) and Suzuki et al. (2012) and is extended to express the dissipation in the vertical direction. For the case of regular waves the expression for wave transmission through horizontal orientated cylinders is given by:

$$\frac{H}{H_0} = \frac{1}{1+\beta x} = K_v \tag{2.9}$$

Where H and H_0 are the local and incident wave height, β is as Equation 2.10 (see below) and K_v is the damping coefficient (Mendez & Losada, 2004).

$$\beta = \frac{4}{9\pi} C_D b_v N_v (\frac{gk}{2\sigma})^3 \frac{sinh^3(k\alpha_z d) + 3sinh(k\alpha_z d) + cosh^3(k\alpha_z d) - 3cosh(k\alpha_z d) + 2}{3kcosh^3(kd)} \tag{2.10}$$

Where:

- b_v is the vertical spacing in [m]
- α_z is the fraction of a certain layer over the water depth

2.2.4. Effect of structure configuration on wave dissipation

Permeable(porous) structures can have different configurations and as result may give different energy dissipation rates. This has been the topic of two recent theses at TU Delft (Jansen, 2019; Haage, 2018). They studied the effect of vertical and horizontal orientated cylinders under the loading of waves in a wave flume. Their results supported Equation (2.10), and showed that placing a structure in an horizontal orientation increases wave dissipation compared to a vertical orientation for deep water waves. For shallow water conditions, the vertical orbital velocities become negligible and horizontal and vertical structures produce similar wave attenuation.

Jansen (2019) studied also the dissipation rate per element by measuring forces and velocities at the scale of individual poles. Jansen (2019) studied four configuration types, see Figure 2.2, with both a horizontal and vertical orientation. He found that the most effective configuration, in both vertical and horizontal, is the longitudinal (see Figure 2.2) which consist of dense rows of cylinders with a long streamwise spacing.

This configuration is the most effective per element as it squeezes the flow (blockage) and it has space in streamwise direction to develop a wake so the downstream elements are not sheltered. The uniform dense configuration is so densely packed that the downstream cylinders are in the wake of the upstream cylinders and thus they have a reduced drag force compared to sparsely placed rows. The staggered configuration has a reduced wave attenuation efficiency because there is less flow acceleration (blockage) between the elements compared with the longitudinal configuration. Cylinders in a staggered arrangement experiences less sheltering than the longitudinal configuration which is favourable in terms of maximising the drag force. The spacings in streamwise and lateral (perpendicular to the stream direction) are thus both important factors that influence the efficiency of a configuration, this process is illustrated in Figure 2.3.

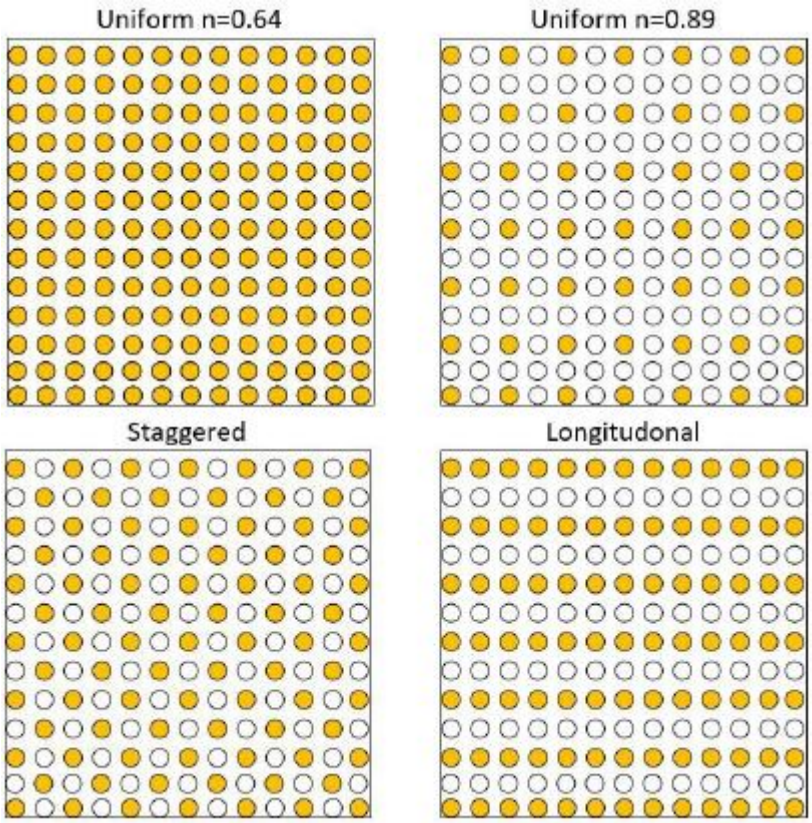

Figure 2.2: Four different configurations from (Jansen, 2019) with waves coming from the bottom. The uniform dense (n = 0.64), uniform open (n=0.89) and longitudinal will be used later in the validation of SWASH.

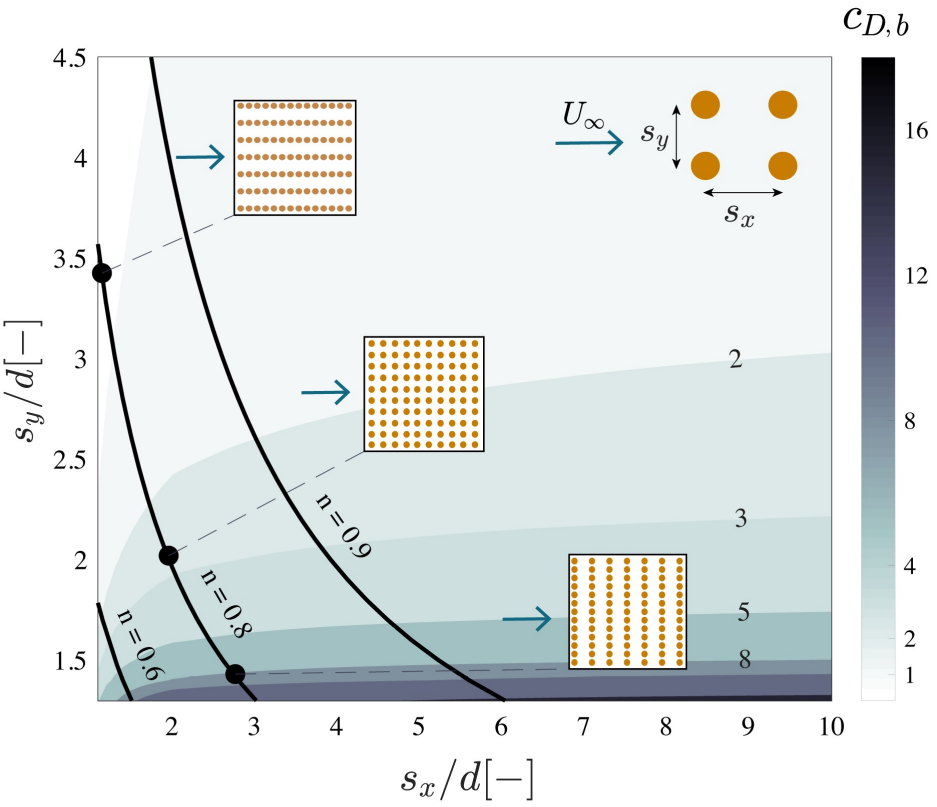

Figure 2.3: Bulk drag coefficient vs. relative spacing in x and y direction as function of the diameter of the cylinders. The lines indicate a constant volumetric porosity and show that for the same porosity, the drag coefficient can significantly vary depending on the placement of the cylinders in x and y direction (Gijón Mancheño et al., 2021)

2.2.5. Effect of wave non-linearity on wave dissipation

The theses of Haage (2018) and Jansen (2019) described an experimental set up based on field measurements from Demak, Indonesia by Witteveen+Bos and the BioManco project. They explained their results by use of linear wave theory where the waves they produced in the wave flume were not linear. In most of the experiments of wave attenuation by vegetation linear wave theory is used, but that may be not representative for the real live situations. Phan et al. (2019) has studied the effect of non linear waves, they compared laboratory tests with the numerical model SWASH and found that an increasing non-linearity of the waves, described by the Ursell number, increased also the wave attenuation. The Ursell number represents the degree of non-linearity of the waves and can be determined with the following formula:

$$N_{Ursell} = \frac{HL^2}{d^3} \tag{2.11}$$

A year earlier Dao et al. (2018) already concluded that for an increasing Ursell number the transmission coefficient decreased and thus the wave attenuation increased. They studied the transmission of waves through a permeable structure, in their case a fence, and analysed them by means of the Ursell number and the ratio of the width of the fence to the peak wavelength. They showed that for a larger ratio the wave transmission rates were lower which indicates that relative short waves are damped more efficient than long waves by a fence. Both Dao et al. (2018) and Phan et al. (2019) show that the behaviour of non-linear waves can be explained by the order of non-linearity but the physical process behind this is still not well understood.

2.2.6. Effects of current on wave dissipation

The coast of Demak can be classified as microtidal (Tas et al., 2020), but the modelling study by Smits (2016) suggests that the currents may play a significant role in the morphodynamic development of the area. Hu et al. (2014) conducted experiments with wave and currents to investigate the effect on wave dissipation by vegetation. They studied the situation where waves and currents have the same direction. Their work suggest that the effect of currents on wave dissipation depends on the ratio of u_c/u_w, in which u_c is the current velocity. Measured currents nearby existing structures were small compared to the wave induced velocity. However, structures are planned to be built nearby creeks where the influence of currents may be larger due to the larger water depth and the continuous inflow of water.

The thesis of Borsje (2018) provides information about the local currents and interaction with the existing permeable dams. The current design of the dams causes that the flows parallel to the dam are usually stronger than going through the dam, as flowing along the dam has less resistance. He also found that at places where waves are more dominant there is no flow through the permeable dams as the wave-induced Stokes flow is stronger than the rising tide.

2.2.7. Mussels

The main goal of the Building with Nature consortium is to bring back the mangroves to create a natural protected coastline but also at the same time provide a sustainable way of living. One of the alternatives could be by mussel aquaculture and specifically the farming of the green mussel, which is a native species Siddal (1980).

The green mussel grows fast and the adult size is approximately 8-10 cm (Soon & Ransangan, 2014), the marketable size is approximately 6 cm after six months (Rajagopal et al., 1998) in India. In Indonesia Rejeki et al. (2021) reported a marketable size of 3-5 cm after 2-3 months.

Rejeki et al. (2021) suggested that it is possible to grow green mussels at the coast of Demak, even in shallow depths (0.4 -0.7 m MSL) whereas other studies (Soon & Ransangan, 2016) and (Sallih, 2005) would rate any depth under 2 m unfavourable. They used two methods, shown in Figure 2.4: traditional stakes and the longline method. The traditional method by growing mussels on stakes can only be carried out in limited water depth as harvesting is done on feet. The long line method has a wider range and can for instance also be applied at rafts in a sheltered area (Soon & Ransangan, 2016).

Mussels require minimum water depths of 0.4-0.7 m in low tide, which would translate to 0.9-1.2 m with respect to MSL to avoid that they are emergent during spring tide. Another requirement is that in the early livestages of the mussel, the mussel is prone to predation in a zone of 30 to 40 cm away from the bottom.

The structures of the previous project (built between 2015-2020) were originally designed to be at MSL, whereas the structures of the MuMaCo project will have to be placed below MSL to enable mussel aquaculture. This could affect the structure performance, but this has not been yet investigated.

The effect of a cylinder covered with mussels on the flow can be divided in the following:

- Due to the irregular surface, the roughness increases with respect to a smooth pole

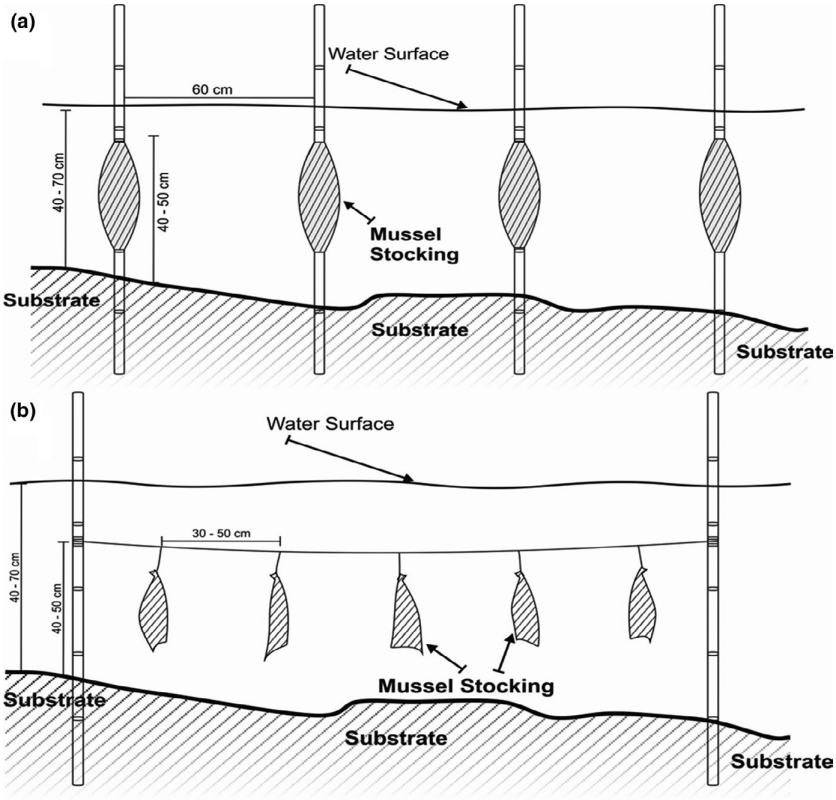

Figure 2.4: Two methods of growing green mussels, (Rejeki et al., 2021).

- The increased diameter of the total pole causes that the flow has to travel a larger distance around the pole, this facilitates therefore lower KC numbers and dependent on the flow regime could give larger inertial forces.

These effects are however not uniform over the length of the pole as they depend on the density of the mussel and as mentioned earlier in this section they only are present between 40 cm above the bed and under MLWS.

One of the assumptions of wave dissipation method of Dalrymple et al. (1984) is that skin friction is negligible however when the cylinder is subject to growth of aquatic species like mussels or kelp for instance than the roughness of the cylinder surface becomes important. The roughness of a surface can be described in terms of the relative roughness height:

$$e = \frac{\Delta D}{D_e} \tag{2.12}$$

Where ΔD is the distance between the solid volume and the edge of the outer cylinder and D_e is the diameter of the external cylinder. For the case of a steady flow the drag coefficient of a rough cylinder drops from C_d = 1.4 to 1.1 when the flow regime changes from subcritical (Re = 10^4) to transcritical (Re=10^6), whereas for a smooth pole C_D drops from 1.4 to 0.5(critical) and then increases to 0.8 (transcritical) (Sumer & Fredsoe, 2006).

Next to the roughness of surface also the amount of mussels on the surface is important, for different amount of densities Theophanatos (1988) reports C_d values ranging from C_D = 1.0 to 1.25 with a surface cover ranging from 20 % to 100 %.

As mussels are filter feeders, they exchange water with their surroundings to gain nutrients. Plew et al. (2009) reported that no added roughness was measured in their experiments due to the exchange of water. They tested this by towing a rope full with mussels through a flume, where the towing speed varied between 0.05 and 0.4 m/s.

3

Methodology

3.1. Introduction

The research methods of this thesis are:

(1) Determination of the design conditions for the structures. For this purpose, model data of WaveWatch III is validated against short-term wave buoy measurements in Demak. Once the WaveWatch data proved to be representative of the wave conditions of Demak, it is analyzed to determine the design conditions. Surge levels are obtained from model results of Willemsen et al. (2019), and tidal levels are based on the measurements of Van Domburg et al. (2018) with the tidal constituents from Tas et al. (2020).

(2) The SWAN model, which is applied to propagate offshore waves to the location of the permeable structures, is validated with the data of Van Bijsterveldt and Bouma (2021).

(3) Computing nearshore wave transformation through structures with SWASH. SWASH is validated with the data of the experiments of Jansen (2019), and several scenarios are calculated to compare which structure designs satisfy the requirement of 50-64% transmission.

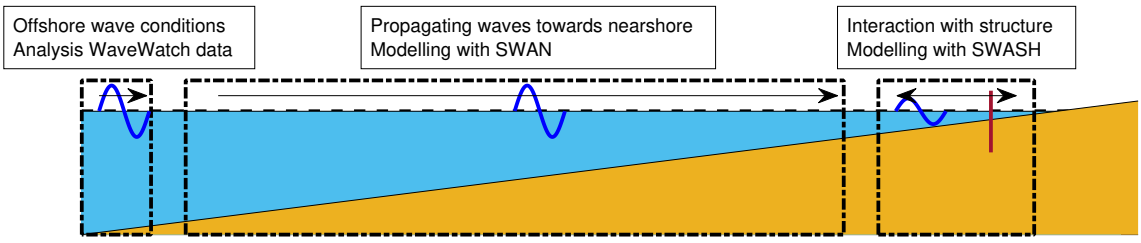

Figure 3.1: Overview of the different steps of this thesis, with from left to right: the offshore boundary analysis, the use of SWAN for propagating the offshore design waves to the nearshore, the domain of SWASH with which the interaction with waves and structure is modelled.

3.2. Design conditions analysis

This sections starts with an analysis of the offshore in Section 3.2.1, then the water elevation and the processes behind this like surge and the tide are identified in Section 3.2.2.

3.2.1. Offshore waves

Defining the design conditions requires analyzing time series of local offshore wave conditions for several years. Firstly, the existing datasets are identified and compiled in a repository. The main sources of data are:

- Predictions by the WaveWatch III model by NOAA over the period of 2007 – 2019
- Measurements of Van Bijsterveldt and Bouma (2021)

The offshore measurements of Van Bijsterveldt and Bouma (2021) were done over periods between November and December in 2017 and 2018, during the NW monsoon with a wave buoy, the WaveDroid (Tas et al., 2020). The WaveDroid was located 5.5 km offshore around a depth of 12 m. The data provided by the WaveDroid consists of the following:

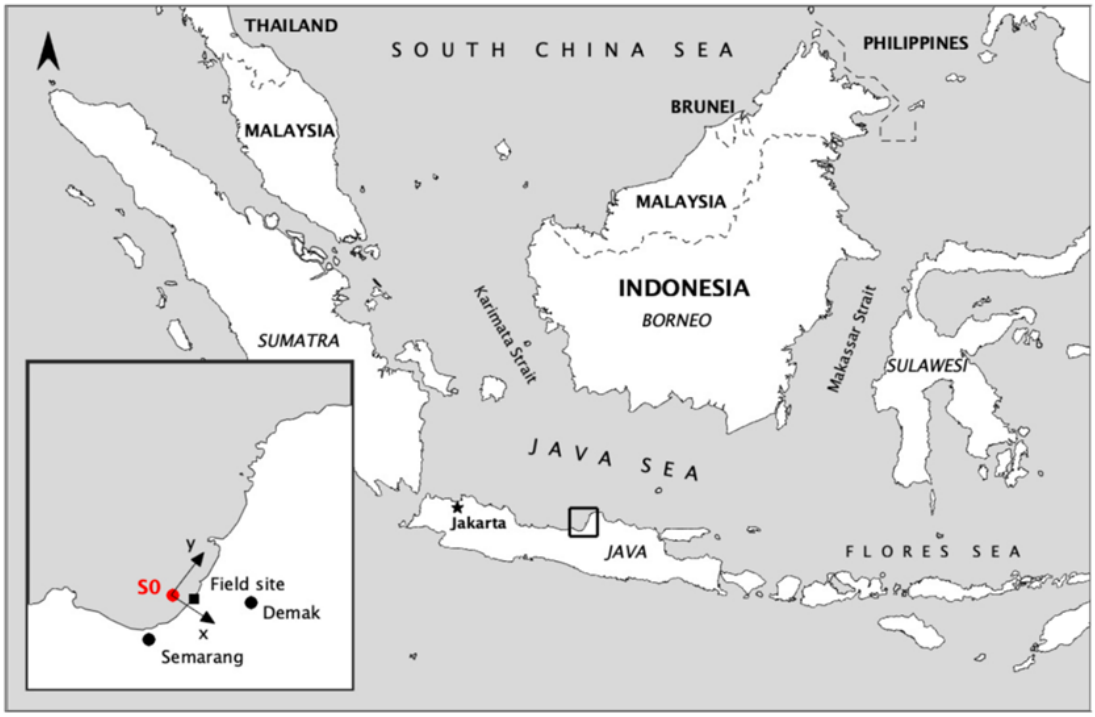

Figure 3.2: Location of the WaveDroid by Tas et al. (2020), located approximately 5.5 km offshore with a depth 12 m MSL.

- The significant wave height H_{m0} in [m]
- The peak wave period T_p in [s]
- The wave direction in rad with respect to North
- The 1D energy spectrum in [m^2/Hz]
- The 2D energy spectrum in [m^2/Hz per rad]

The WaveWatch III predictions contain the following parameters:

- The significant wave height H_{m0} in [m]
- The significant wave period $T_{1/3}$ in [s]
- The wave direction in degrees with respect to North
- Wind velocity in U_{wind} in [m/s]
- Wind velocity in V_{wind} in [m/s]

The WaveWatch III data is interpolated at the location of the WaveDroid, see Figure 3.2. In the period from November - December 2017 a comparison is done between the WaveWatch III data and the measurement of the WaveDroid as in this period quite a large storm was measured. The field measurements were characterized by peak periods whereas the WaveWatch III predictions are defined by wave periods belonging to the significant wave heights. As the spectrum itself is not available but only the H_{m0} and the T_p, T_p can be transformed to $T_{1/3}$ for an unimodal wind spectrum (Holthuijsen, 2007):

$$T_p \approx \frac{T_{1/3}}{0.95} \tag{3.1}$$

In order to calculate the design conditions, the wave data from WaveWatch III is filtered in terms of wave direction, wave height and the occurrence between certain high wave heights in time.

Wave filtering on wave direction

The coastline of Demak has a shoreline normal of 301 degrees (Nautical), therefore only the waves that fall inside a certain bandwidth of this shoreline angle have a significant impact on the coastline. Three bandwidths are tested: a narrow bandwidth of 290-310 degrees, an average bandwidth of 280 -320 degrees and a wide bandwidth of 270 -330 degrees.

Wave filtering on wave height and duration

After the wave conditions are selected based on the wave direction in the previous steps, the wave conditions have to be further filtered based on wave height as the focus of this study is on the higher waves. This is done with a Peak over threshold (P.o.t.) method, where the peaks are the waves that are higher than a chosen threshold. This method also uses a threshold in time, which represents the minimum time between successive storms. Determining the thresholds is a sensitive process, because with a low duration a storm could be selected twice or with a low wave height threshold there would be too much scatter. However, with high thresholds the amount of data for the statistical analysis would result in a too high standard deviation.

Van den Bos (2018) suggest that the thresholds should be selected in such manner that the number of storms per year is between 2 and 10. The minimum time between successive storms is varied between 48 and 96 hours, as 1 one day is assumed to be too short between two storms and 5 days is assumed as too conservative. The wave height threshold is varied between 1 and 1.5 m.

Extrapolation of the filtered dataset

The Peak over threshold method produces a dataset of wave heights. For design purposes it is important to be able to tell which wave height belongs to which return period. This is done by using four different distributions functions: Exponential, Weibull, Gumbel and Generalised Pareto. The Equations of the distributions are provided in Appendix A. The predictions of the distributions are compared against the dateset of the P.o.T. method in terms of RMSE. Where the RMSE is the following:

$$RMSE = (\frac{1}{n}\sum_{n}^{1}(H_{data} - H_{distr})^2)^{0.5} \tag{3.2}$$

Where:

- H_{data} and H_{distr} are the wave height from the P.o.t. dataset and the used distribution
- n, is the number of wave heights

If the Generalized Pareto distribution is used then the uncertainty can be estimated with a Bootstrap method (Van den Bos, 2018). In the Bootstrap method a new dataset is created with the same size as the original dataset, so for example if 66 waves are selected from the Peak over threshold method then the Bootstrap also creates a dataset of 66 waves. A dataset is then created by selecting random samples with replacement from original dataset, so some waves may occur twice or none at all. Then this new dataset can be fitted through the extreme value distribution. In order to characterize the uncertainty, this process is repeated 1000 times to obtain a distribution of all datasets. From this point on the mean and standard deviation can be found from this data.

To check the sensitivity of the minimum time between successive storms, the results of the three different durations are compared along the same wave height threshold, that of H_{m0} = 1.3 m To check the sensitivity of the wave height threshold, this is varied along the same duration (48 hours) with the values of H_{m0} = 1.2 m and 1.4 m.

Associating wave period with wave heights

In order to fully define the design wave conditions, a wave period needs to be associated to the wave height values derived from the previous Section. A correlation in wave steepness can be used to link the wave period to the predicted wave heights from the Generalized Pareto distribution, where the wave steepness is:

$$s_0 = \frac{2\pi}{g}\frac{H}{T^2} \tag{3.3}$$

This is rewritten to the form of:

$$a = \frac{\sqrt{H}}{T} \tag{3.4}$$

3.2.2. Water level

In order to define the water levels in Demak, Indonesia measurements by of the BioManCO project are analyzed and compared with the studies of Tas et al. (2020) and Smits (2016). The measurements were done at the seaward end of two transects, see Figure 3.3, approximately 500 m offshore around an average depth of 1.25 - 1.5 m MSL. The measurements were collected by BioManCo(2018) and analyzed by Van Domburg et al. (2018) in November – December 2017.

The measurements are processed with the use of the Matlab tool UTide of Codiga (2011). This tool needs the following input:

Figure 3.3: Location of transects A (Accreting) and E(Eroding) Van Domburg et al., 2018, where the most seaward measurement locations are used for the water level analysis.

- Time series of a water level
- Location of the water level input in the form of a latitude
- The names of the tidal constituents which are present in the area

The surge levels are based on Willemsen et al. (2019) for the coast of North Java, where they translated surge levels from a oceanic model to a coastal model and divided the coast of Java in several segments. The segments near Semarang will be used for the surge levels at the project location.

3.3. SWAN

SWAN is used to simulate wave propagation from the location of the WaveDroid, see Figure 3.2 to the location of the structures in the nearshore, which corresponds with a distance of approximately 5.5 - 6 km. SWAN is a third generation wave model that propagates waves to the nearshore. The governing equations are:

$$\frac{\partial E(f,\theta;x,y,t)}{\partial t} + \frac{\partial c_{g,x} E(f,\theta;,x,y,t}{\partial x} + \frac{\partial c_{g,y} E(f,\theta;x,y,t}{\partial y} = S(f,\theta;x,y,t) \tag{3.5}$$

The first term describes the rate of change of energy in a grid cell over time, the second and third term describe the in- and export of energy of a grid cell and the fourth term describes the sources and sinks of energy.

Where:

- f are the frequencies in a variance density spectrum [Hz]
- θ is the direction of the wave components of the spectrum in [°]
- x is the horizontal position of the spectrum
- t is the time

Where S presents the difference source/sink terms, for instance whitecapping or wind.

3.3.1. Model setup

Bathymetry

The bathymetry implemented in SWAN is based on measurements from the BioManCo project, shown in Figure 3.4, it was measured with a CTD device. For simplicity this bathymetry is assumed as a constant slope of 1:500 from a depth of -12 to 0 m MSL, Figure 3.4 shows that is assumption is valid for the depth of -12 to -1 m MSL. From -1 m MSL the slope turns from 1:500 to almost flat. Due to a constant slope the presence of cheniers (alongshore orientated sand lenses) is neglected, which is a conservative approach as the cheniers are acting like a temporary submerged breakwater.

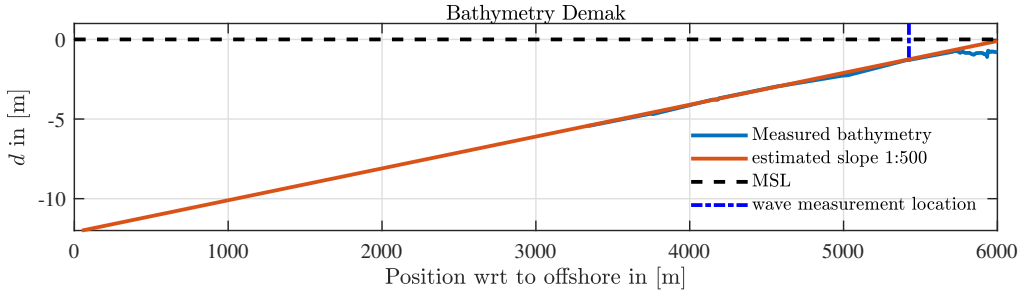

Figure 3.4: Bathymetry Demak, Indonesia measured in the BioManCo project (or Bijleveldt 2021b) with a CTD device. The wave measurements are those of the BioManCo project along two transects, see (Van Domburg et al., 2018)

Figure 3.5 shows that the depth lines are almost parallel, therefore the coast is assumed to be alongshore uniform.

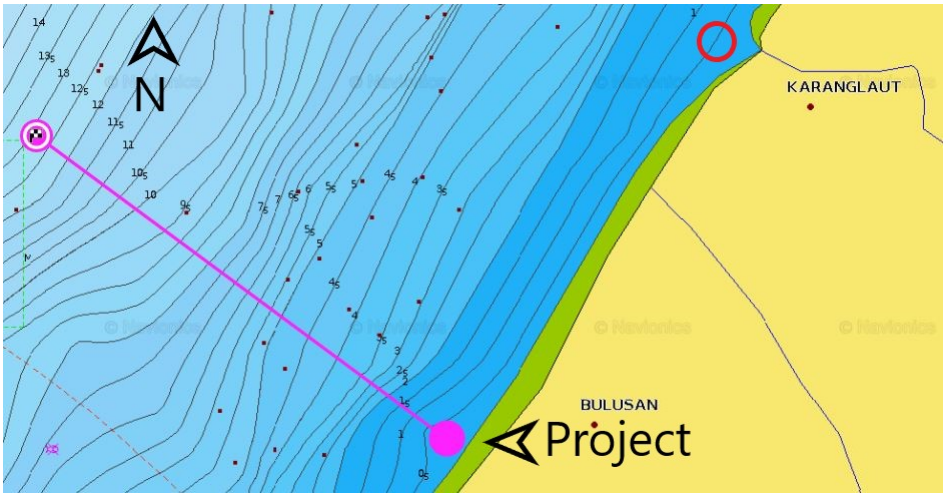

Figure 3.5: Bathymetry of project area, with in pink approximately the direct line from the offshore location of the WaveDroid to the project location, accessed via Navionics Chartviewer https://webapp.navionics.com/

Grid

A 2D square grid is used with a width and length of 6 km, the space discretisation in x direction (shorewards) is 10 m and in y direction (alongshore) 100 m. For the wave spectrum a directional grid of 72 directional bins of 5 degrees each is used. The wave frequency range is between 0.04 and 1 Hz.

Boundary conditions

Waves are imposed at the offshore boundary, consisting of H_{m0}, T_p wave direction and a directional spreading. The T_p is chosen as the waves in the peak of the spectrum contains the most energy and are therefore the limiting conditions. The wave direction is constant and perpendicular to the coast. The directional spreading is set constant for the whole simulation but is varied to check the sensitivity. The wave characteristics are the measurements of a wave buoy, the WaveDroid placed by Tas et al. (2020), located at approximately 5.5 km offshore around a depth of 12 m. At the land boundary SWAN uses a no flux boundary.

Physical parameters

The following processes are activated in SWAN:

- Breaking
- Wave-setup
- Triads
- White capping
- Friction

The following processes are not activated or taken into account:

- Diffraction
- Wave dissipation by mud

Output

To be able to compare the SWAN-simulations with the measurements from the BioManCo project, the output is generated at the same average depth as the measurements where taken, see Figure 3.4 for overview. The output of SWAN consists out of the wave height and wave period along the computational grid. To make it into a timeseries, individual files are generated for each timestep.

3.3.2. Calibration

SWAN is calibrated to reproduce the same wave characteristics during the storm event around 1 December 2017. The parameters that are used in the calibration are: the breaking parameter, wind velocity, directional spreading and friction.

3.4. SWASH

SWASH is a numerical model that can simulate non-hydrostatic, free -surface, rotational and transport phenom in one, two, or three dimensions (SWASH Manual). The governing equations are the shallow water equations(SWE) including a non-hydrostatic term, these are shown below:

$$\frac{\partial \zeta}{\partial t} + \frac{\partial hu}{\partial x} = 0 \tag{3.6}$$

$$\frac{\partial u}{\partial t} + u\frac{\partial u}{\partial x} + g\frac{\partial \zeta}{\partial x} + \frac{1}{h}\int_d^\zeta \frac{\partial q}{\partial x} dz + cf\frac{u|u|}{h} = \frac{1}{h}\frac{\partial h\tau_{xx}}{\partial x} \tag{3.7}$$

Where:

- ζ is the surface elevation in [m]
- g is the gravitational constant, 9.81 [m/s^2]
- q is specific discharge in [m^2/s]
- c_f is a friction parameter
- τ is the shear stress in [N/m^2]

3.4.1. Experiment setup

For the validation of SWASH the second set of experiments in the study of Jansen (2019) is used. In his thesis he studied the effect of wave dissipation by permeable structures by means of experiments in the wave flume in the laboratory of the Hydraulic department of Delft University of Technology. He based the setup on the physical characteristics of the system in Demak, Indonesia.

The wave conditions that are used in the experiments have a constant wave height and the wave period is varied to have different waves. In the Table 3.1 the characteristics of the waves are summarized. Where:

- c, is the wave celerity in [m/s]
- n, is the wave group number
- c_g, is the group velocity in [m/s]
- kd, is the relative wave number
- N_{Ursell} , is the Ursell number as in Equation 2.11.

T	H	h	L	k	c	n	c_g	kd	N_{Ursell}
[s]	[m]	[m]	[m]	[1/m]	[m/s]	[-]	[m/s]	[-]	[-]
1	0.13	0.55	1.527	4.11	1.53	0.55	0.84	2.26	1.82
1.25	0.13	0.55	2.23	2.82	1.78	0.64	1.14	1.55	3.89
1.5	0.13	0.55	2.92	2.15	1.94	0.72	1.40	1.18	6.66
1.75	0.13	0.55	3.57	1.76	2.04	0.79	1.60	0.97	9.96
2	0.13	0.55	4.22	1.49	2.11	0.83	1.75	0.82	13.91
3	0.13	0.55	6.68	0.94	2.23	0.92	2.05	0.52	34.87

Table 3.1: Wave conditions used in experiments by Jansen (2019)

The wave experiments were carried out in the flume of TU Delft and which has the following dimensions: length of 40 m, width of 0.76 m. The permeable structure is located at a distance of 18.2 m from the wavemaker and at the end of the flume there is a wave absorber that should minimize the reflections. The distance from the wavemaker to the permeable structure is 18.2 m and from the model to the wave absorber 15.8 m. The wave absorber has a 1:3 slope to absorb the waves. The experiments were measured with four wave gauges, located as in Figure 3.6. The timeframe in which the waves are measured is so defined that the reflecting waves from the back of flume do not interfere with measurements, see Figure 3.7 for visualization.

The waves that Jansen used were non-linear, which is shown by the Ursell number in the last column of the Table 3.1. Non-linear waves can be described by Stokes' theory or by cnoidal wave theory. Stokes' theory is applicable up to N_{Ursell} <10 and cnoidal wave theory for N_{Ursell} >26, however both apply equally well for the range 10 < N_{Ursell} < 26 (Holthuijsen (2007)). Stokes' theory works essentially as the sum of higher harmonics with the basic harmonic whereas cnoidal wave theory are expressed as Jacobian elliptic functions, this last one can only be implemented in SWASH as a timeseries.

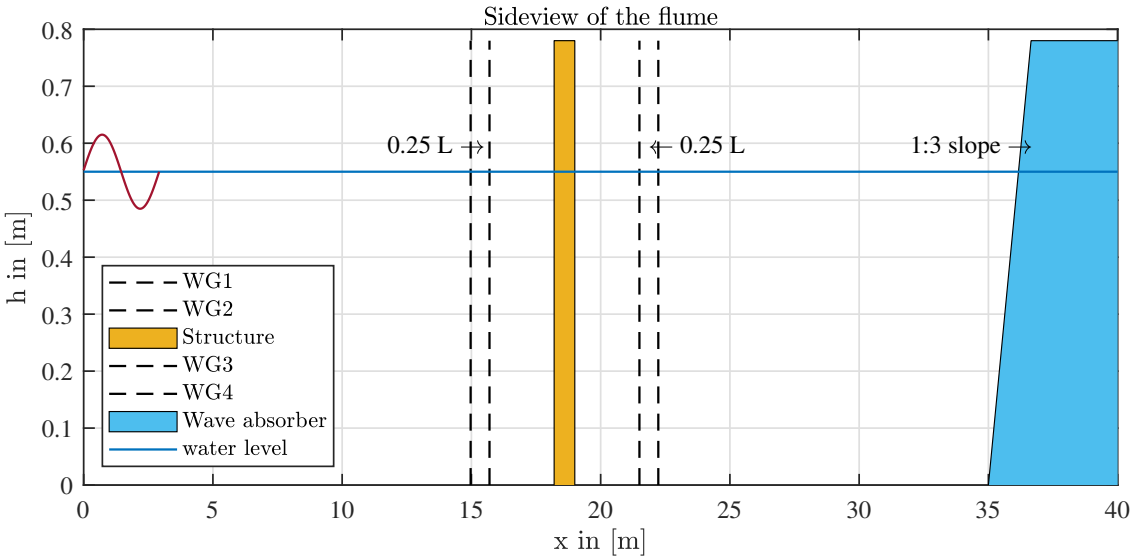

Figure 3.6: Side view of the flume and the set up of the wave gauges from (Jansen, 2019). Waves are coming from the left (x= 0), with the structure at x =18.2 and a wave absorber at x = 35 m. There are two sets of wave gauges in front and behind the structure.

3.4.2. Model setup - Experiments Jansen (2019)

Input

The wave input is defined by a constant weakly reflective boundary on the left side of the flume.

Grid

A non-stationary 2DV setup is used. The computation grid is 35 m long with an additional length for the sponge layer which is three times the wave length. The sponge layer is needed to absorb the waves, otherwise they would reflect from the end of the numerical flume. The space discretization is 2.5 cm and is kept constant along all wave conditions, which gives for the shortest wave 60 grid points per wavelength where 50 grid points is the minimum for accuracy reasons (SWASH manual). For the dispersion of primary waves, either linear or the first harmonic of a non-linear wave, the following accuracy ranges are suggested for the number of layers see Table 3.2.

K	Range	Error
1	kd < 0.5	1 %
1	kd < 2.9	3 %
2	kd < 7.7	1 %
3	kd < 16.4	1 %

Table 3.2: accuracy ranges for number of layers and kd number, (SWASH Manual)

When a wave spectrum is used as input or when the waves are non-linear, Table 3.3 is used to estimate the required number of layers over the depth to determine which frequency can be simulated accurately. The Table shows the maximum frequencies up to a depth of 1 m but the wave flume has a depth of 0.55 m. The maximum frequency increases with a decline of the depth. So for a water depth of 0.55 m and the higher harmonic of T = 1 s which gives 2 Hz, 3 layers should be accurate.

d (m)	K =1	K =2	K =3
1	0.82	1.37	2.00
5	0.37	0.61	0.89
...	...	...	...
100	0.08	0.14	0.20

Table 3.3: Cut off frequency as relation of depth and number of layers, (SWASH Manual)

As the flume has no sloping bottom, the water depth is constant across the domain and equal to 0.55 m. Friction is neglected as the distance over which the waves travel is small and the bottom of the wave flume is assumed to be smooth. Turbulence is not activated.

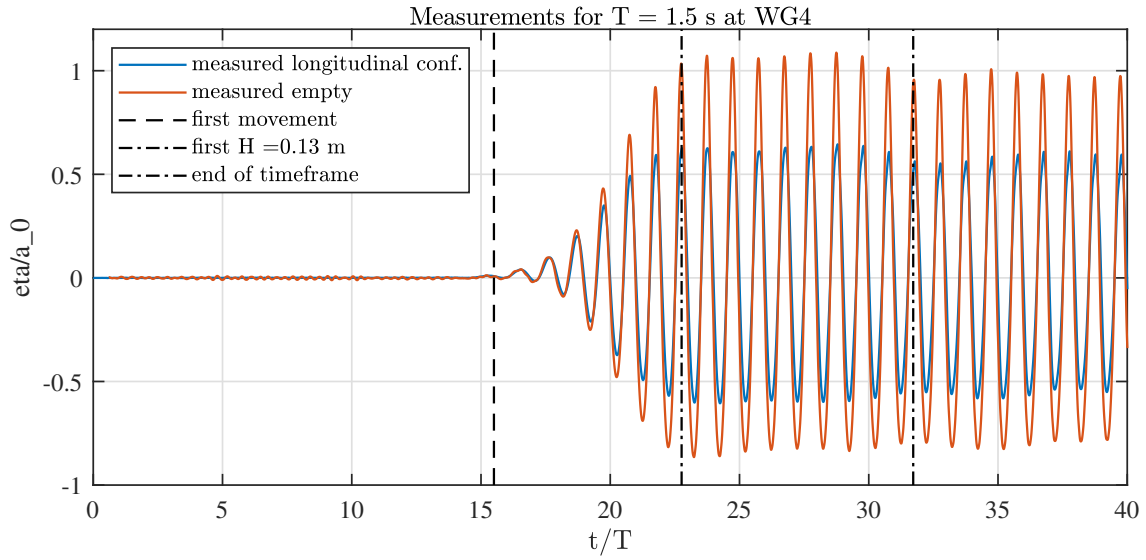

Figure 3.7: The following timeframe is used to process the measured timeseries of the physical experiments of Jansen (2019), as the timeframe is restricted due to waves reflecting from the physical wave absorber at the end of flume as this did not work perfectly. The blue line indicates the measured water surface for the longitudinal configuration and red line is without any structure in the flume, the timeframe indicates a period from when the wave height reach a value of 0.13 m to the point that the reflected waves reach the measuring location.

T	kd	f1	f2	K	K	K
[s]	[-]	[Hz]	[Hz]	Table 3.2	Table 3.3	definitive
1	2.26	1	2	2	3	3
1.25	1.55	0.8	1.6	2	3	3
1.5	1.18	0.67	1.33	2	2	2
1.75	0.97	0.57	1.14	2	2	2
2	0.52	0.33	0.67	2	1	2

Table 3.4: Number of layers per wave condition

The Keller-Box scheme is used for accurately determining the vertical pressure gradient, which is advised for the propagation of short waves. A non-hydrostatic pressure mode is selected with the iterative solver BiCGSTAB that solves the solution of the Poisson pressure equation. As preconditioner the ILU is chosen with a default of maximum 500 iterations, which is more robust for very short or high waves. To improve the rate of converge for the preconditioner a weighting factor of alfa = 0.55, which should lead to the optimal convergence (manual swash). For the relative accuracy of the right-hand side of the Poisson pressure equation the default of 0.01 is used and with respect to the initial residual the default of 0.0 is used.

3.4.3. Vegetation module

The location of the configurations in the wave flume is as in Figure 3.6, 18.2 m from the wavemaker boundary.The different configurations can be implemented in SWASH with the vegetation module, see Figure 3.8 for an top view. They cover the full width (0.78 m) of the flume and cover a length of 0.76 m in stream-wise direction. The cylinders are 4 cm in diameter and emergent. SWASH defines vegetation as an amount of cylinders over a certain area by the following parameters:

- Height of cylinders in [m]
- Number of stems(cylinders) per m2 , [N_{stems}/m^2]
- Diameter of cylinder in [m], D
- Bulk drag coefficient, $C_{d,b}$
- The added mass coefficient , C_m
- Porosity, n
- In case of horizontal and vertical orientated cylinders, the vertical drag force can be included

The porosity in SWASH is defined as follows:

$$n = A_c / A = 1 - N_{stems} 0.25 \pi D^2 \tag{3.8}$$

Where A_c is the flow conveyance area and A is the total area. The effects of porosity are included in the shallow water equations by replacing u with u/n in such that the ambient flow is characterized by the pore velocity (Suzuki et al., 2019). The momentum equation, Equation 3.7 becomes then the following:

$$(1 + C_m(1-n))\frac{\partial(\frac{u}{n})}{\partial t} + n\frac{\partial(\frac{u}{n})^2}{\partial x} + n(g\frac{\partial \zeta}{\partial x} + \frac{\partial q}{\partial x}) + \frac{1}{2} C_D \frac{h_v}{h} N_{stems} \frac{u}{n} |\frac{u}{n}| = 0 \tag{3.9}$$

The cylinders can be implemented by a grid, that defines the density of plants per grid point with a default value of 1. The plants grid has the same dimensions as the computational grid to have the same amount of grid points as the computational grid.

The bulk drag coefficient is based on the method of Gijon Mancheno et al. (2021). The drag force in the Morrisons Equation 2.2 relates to u^2 and can be expressed as an empirical bulk factor:

$$F_d \sim C_d * u_\infty^2 \sim C_{d,b} * u_c^2 \tag{3.10}$$

Where:

- $C_{d,s}$ is the drag coefficient of a single cylinder
- u_∞ is the flow undisturbed velocity in [m/s]
- $C_{d,b}$ is the empirical bulk drag coefficient
- u_c is the characteristic flow velocity influenced by the structure in [m/s]

The characteristic flow velocity u_c represents how the velocity changes between a group of cylinders and is defined according to Gijon Mancheno et al. (2021):

$$u_c = u * f_{kc} f_s f_b \tag{3.11}$$

Where the factors f_{kc}, f_s and f_b are determined as below in Equations 3.12, 3.13 and 3.14.

To account for the effect of blockage in the structure, where blockage is calculated using mass conservation through a cross-section of the structure, the following equation is used:

$$f_b = \frac{1}{1 - D/s_y} \tag{3.12}$$

Where:

- s_y is the center to center distance between two adjacent cylinders perpendicular to the flow direction(lateral) in [m]

Sheltering of the wakes by the upstream cylinders is calculated according to:

$$f_s = 1 - \frac{c_s}{s_x / D} \tag{3.13}$$

Where:

- c_s is an empirical coefficient dependent on the turbulent intensity
- s_x is the center to center distance between two adjacent cylinders in flow direction

The KC state of the flow is expressed in the following factor:

$$f_{KC} = 0.012 KC + 0.44 \tag{3.14}$$

Both porosity and $C_{d,b}$ describe conservation of mass, but the porosity refers to mass conservation over a fluid volume, and the blockage factor refers to mass conservation over a cross-sectional flow surface. They are thus related to each other, but result in different values of flow acceleration. When the porosity is activated in SWASH, $C_{d,b}$ should be adjusted to avoid accounting for the porosity twice.

3.5. Wave propagation through a permeable structure

3.5.1. Boundary conditions

Before the case with a structure is simulated, the situation without a structure is simulated to validate the propagation of the waves. As input for the boundary conditions two theories are tested, the use of the stream theory by Fenton (1988) and Stokes' theory. As input for SWASH a time series is created with Fenton (1988). Stokes' theory can be implemented in SWASH by means of defining the separate Fourier components. Table B.1 shows the parameters that are used as input.

3.5.2. Wave transformation through structures

To model the wave transformation through the structures the vegetation module is used in SWASH, see Section 3.4.3. There are four configurations that are studied, see Figure 4.30.

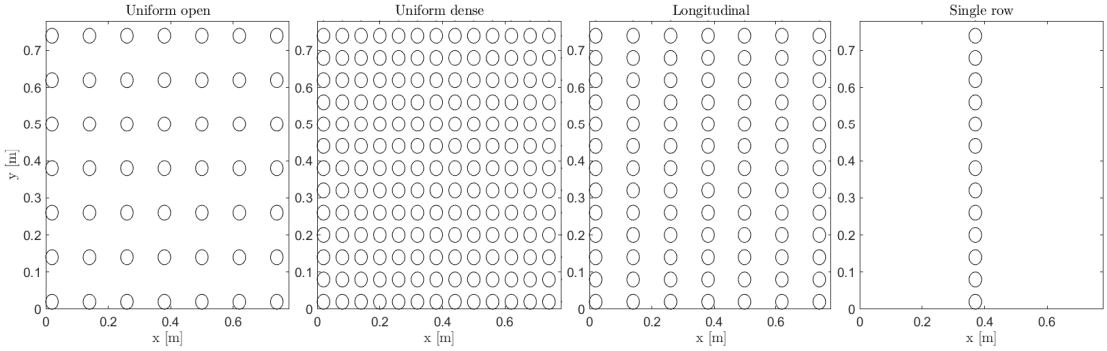

Figure 3.8: Topview of the used configurations, with from left to right: the uniform open conf., the uniform dense conf., the longitudinal conf. and the single row conf. Waves are coming from the left.

There are three important variables that can be adjusted to schematize a structure: the bulk drag coefficient, the porosity and the cylinder density. The vegetation module is tested by increasing the complexity in consecutive steps:

1. The choice of which drag coefficient fits with which configuration, the configurations are implemented as block so the cylinder density uses an average value and the porosity is not activated so the mass conservation is through the blockage factor(cross-sectional wise)

2. For the case of the longitudinal configuration, which is the most non-uniform, the effect of a varying cylinder density is studied. The porosity is not included so mass conservation works via the blockage factor.

3. Three methods of describing the mass conservation are studied for the longitudinal and single row configuration, as these have the most resemblance with design structures.

Table 3.5 describes the geometric parameters as input for the vegetation module in SWASH.

Parameters	Height	D	s_y	s_x	f_b	f_s	C_m
Units	[m]	[m]	[m]	[m]	[-]	[-]	
Longitudinal conf.	1	0.04	$1.5D$	$3D$	3	0.73	1
Open uniform conf.	1	0.04	$3D$	$3D$	1.5	0.73	1
Dense uniform conf.	1	0.04	$1.5D$	$1.5D$	3	0.47	1
Single row conf.	1	0.04	$1.5D$	[-]	3	[-]	1

Table 3.5: General geo metric parameters of the four configurations that are used in the validation of SWASH.

Effect of cylinder density

The structure can be implemented as one block or as multiple separate blocks(row by row). This does not affect the total number of stems but it does change the number of stems locally, as is shown in Figure 3.9.

Assuming that the structure is implemented as a block then the number of stems are implemented in vegetation module as the averaged amount of stems over the whole structure. For the row by row grid, the area of one row is defined as the diameter of one cylinder times the width of the flume. Table 3.6 shows the

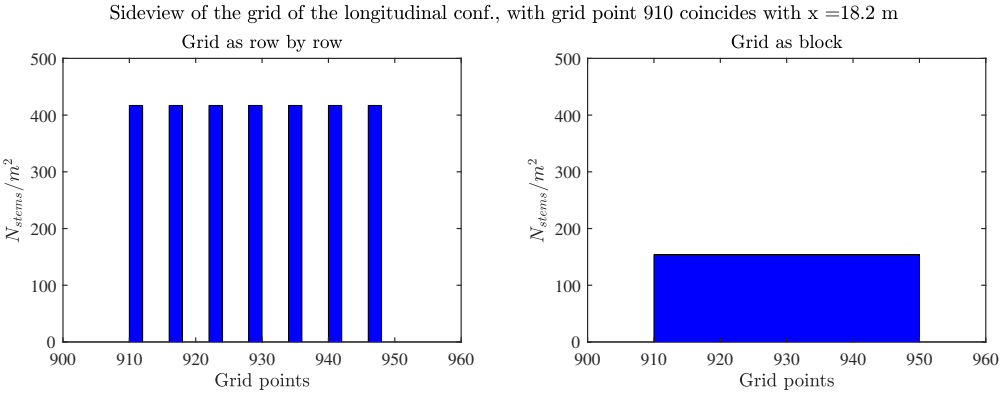

Figure 3.9: Sideview of the plants grid of the longitudinal configuration, with on the left) as row by row and on the right) as one block

Configuration	N_{stems} as block	n_{avg}	nr. of rows	N_{stems} per row	N_{stems} per row	n_{row}
	$/m^2$	[-]	[-]	[per row]	$stem/m^2$	[-]
Longitudinal	154	0.81	7	13	417	0.46
Uniform open	83	0.89	7	7	224	0.72
Uniform dense	285	0.64	13	13	417	0.46

Table 3.6: Porosity and number of stems per m^2 for the block grid or row by row grid

parameters that are used for the configurations. The number of stems are taken from thesis of Jansen (2019) and divided by the length and the width of the permeable structure to have the amount of stems per m2.

In Table 4.9 the bulk drag coefficients for the three configurations are presented.

T [s]	1	1.25	1.5	1.75	2	3
KC	10.43	11.17	12.32	13.65	15.14	21.47
f_{KC}	0.56	0.57	0.59	0.60	0.62	0.70
C_d single cylinder	2	2	2	2	2	2
$C_{d,b}$ longitudinal conf.	3.87	4.05	4.35	4.71	5.14	7.27
$C_{d,b}$ open uniform conf.	0.48	0.51	0.54	0.59	0.64	0.91
$C_{d,b}$ dense uniform conf.	1.01	1.06	1.13	1.23	1.34	1.90

Table 3.7: Full $C_{d,b}$ values for the three configurations of Jansen (2019) that are used to validate SWASH

Conservation of mass

In this last step, two configurations are selected which resemble most of the designs, the structures formed by one or more rows of bamboo poles in Chapter 1. The single row configuration from Jansen (2019) is used as setup for the single fence and mussel pole designs. The longitudinal configuration is used as setup for the designs with two rows or more. For these two configurations the different ways of describing the conservation of mass in SWASH is studied. The porosity ensures that mass conservation is preserved in a porous media, however in the C_b, d of Gijon Mancheno et al. (2021) the blockage factor also describes mass conservation. The conservation of mass is studied with three cases:

1. By using the full $C_{d,b}$ from Gijon Mancheno et al. (2021) without the porosity activated
2. By excluding the f_b in $C_{d,b}$ and with porosity activated, assuming that the flow conservation is defined over the fluid volume.
3. By using a $C_{d,b}$ reduced by a factor n^2 with the porosity activated, in such that it nullifies the term $C_D \frac{1}{n^2}$ in the momentum equation, see Equation 3.9, and thus where flow conservation is defined over the cross-section of the flume instead of the full fluid volume.

Tables 3.8 and 3.9 show the drag coefficient per case for the two configurations.

Case:	f_b	f_s	n	T :	1	1.25	1.5	1.75	2	3
full $C_{d,b}$	3	0.73	0.46	$C_{d,b}$	3.87	4.05	4.35	4.71	5.14	7.27
reduced $C_{d,b}$	[-]	0.73	0.46	$C_{d,b}$	0.14	0.15	0.16	0.17	0.17	0.17
$C_{d,b}\ n^2$	3	0.73	0.46	$C_{d,b}$	0.82	0.86	0.92	0.99	1.09	1.54

Table 3.8: The drag coefficients for three cases for the longitudinal configuration: full $C_{d,b}$ where $C_{d,b} = C_{d,s}(f_b f_s f_{KC})^3$, reduced $C_{d,b}$ where $C_{d,b} = C_{d,s}(f_s f_{KC})^3$ and $C_{d,b} n^2$ where the full $C_{d,b}$ is multiplied with the porosity n^2

Case:		T	1	1.25	1.5	1.75	2	3
full $C_{d,b}$		9.48	10.0	11.59	11.66	11.66	11.66	
reduced $C_{d,b}$		0.35	0.37	0.41	0.43	0.43	0.43	

Table 3.9: The drag coefficients for three cases for the single row configuration: full $C_{d,b}$ where $C_{d,b} = C_{d,s}(f_b f_s f_{KC})^3$, reduced $C_{d,b}$ where $C_{d,b} = C_{d,s}(f_s f_{KC})^3$

3.6. Processing methods: Performance with an imposed reflection

There are several methods that can be used to process the simulations of SWASH and the measurement data of Jansen (2019). In order to understand the accuracy and uncertainty of a certain method, the methods are tested with an imposed reflection. Section 3.6.1 describes the methods that require surface elevation timeseries as input. Section 3.6.2 describes the method that requires a flow velocity and surface elevation timeseries as input.

3.6.1. Processing methods based on surface elevation

To determine the reflection, transmission and dissipation two methods are taken into account that are based on surface elevation: Goda and Suzuki (1976) and Mansard and Funke (1980). For the method of Goda and Suzuki (1976)is a script available from Tu Delft Hydraulics called Refreg. For Mansard and Funke (1980) a script is written. There is also a script available for the method of Zelt et al. (1993) from the Tu Delft Hydraulics but this did not work for the case of regular waves. The methods are evaluated by comparing an imposed reflection coefficient with a measured reflection coefficient.

The method of Goda and Suzuki (1976) requires two wave gauges in front of the structure, the wave gauges should be at least one wave length away from the structure to prevent the noise of non-linearties in the signal. However Dean (1984) explained that these non-linearties are in fact evanescent waves and these are insignificant three times the water depth away from the structure. Goda and Suzuki (1976) assumes that the waves can be described by the use of linear wave theory.

Goda and Suzuki (1976) requires that the separation between the wave gauges is in the range of $\Delta l = 0.05 - 0.45L$ with an optimum of L/4. Where L is the wave length of the regular wave. The incident and reflective wave can be described by the general form:

$$\eta_i = a_i cos(kx - \sigma t + \varepsilon_i) \tag{3.15}$$

$$\eta_r = a_r cos(kx + \sigma t + \varepsilon_r) \tag{3.16}$$

The method of Mansard and Funke (1980) uses a least squares approach to determine the incoming and reflected spectra. It requires three wave gauges, at which the water level is measured simultaneously. It assumes that at every wave gauge signal exists out of an incident wave, a reflected wave and a noise signal. By applying a least squares method, in essential the incoming and reflected wave are solved for which the noise signal is kept at a minimum. The spacing of the wave gauges has the following requirements:

- the distance between wave gauge 1 and 2 should not be half a wave length
- the distance between wave gauge 1 and 3 should not be an integer of the distance between wave gauge 1 and 2

Therefore the following spacings are recommended:

- the distance between wave gauge 1 and 2, $x_{12} = L_p/10$, where L_p is the wave length belonging with peak period of the measured spectra
- the distance between wave gauge 1 and 3, $L_p/6 < x_{13} < L_p/3$ and $x13 \neq L_p/5$ and $x_{13} \neq 3L_p/10$

The equations that are used to determine this are in more depth described in Appendix E.

The difference between the method of Goda and Suzuki (1976) and Mansard and Funke (1980) is that the last method uses more wave gauges which gives a higher accuracy in case of irregular waves, this can also be seen in the study of Zelt et al. (1993). Where Zelt et al. (1993) is an expansion of the method of Mansard and Funke (1980). However for the case of regular waves the improved frequency range and the less critical probe spacing that Mansard and Funke (1980) provides will hardly make a difference as there is only one wave condition. This however has to be studied in case of non-linear waves in which the higher harmonics can also be important. Therefor the methods are evaluated in four steps:

1. Comparison for linear waves
2. Comparison for non-linear waves
3. Wave conditions of the experiments by Jansen (2019)
4. Conclusion

Linear waves

First a set of wave conditions is generated with H = 0.10 , d = 0.8 m and T varies between 1 and 1.5 s with steps of 0.025 s. This results in a dataset of 20 waves with a maximum N_{Ursell} of 2, which can then be treated as linear waves. The surface elevation is composed out of an incoming wave and a reflective wave. The reflected wave is defined as:

$$\eta_r = K_{r,i} * \eta_i \tag{3.17}$$

where:

- $K_{r,i}$ is the imposed reflection coefficient
- η_i is defined as

$$\eta_i = \frac{H}{2} cos(\frac{2\pi}{T} + kx) \tag{3.18}$$

Non-linear waves

A time series is generated using the method of Fenton (1988). Wave conditions are H = 0.10 m, d = 0.8 m and T varies between 1.5 and 3 s with steps of 0.05 s. The N_{Ursell} varies between 2 and 13.

Wave conditions as in experiments Jansen (2019)

In this step the wave conditions of experiments of Jansen (2019) are used to create a time series using Fenton (1988). This means that H = 0.13 m, d = 0.55 m and T varies between 1 and 3 s. The number of harmonics is set to 2.

3.6.2. Processing method based on surface elevation and flow velocity

In the earlier sections of this chapter, the processing methods of Goda and Suzuki (1976) and Mansard and Funke (1980) were described. However these can not measure the wave conditions for the real case in Demak as these are too non-linear, therefore another method has to be used. The method that is used is from the thesis of Dekkers (2018) where he extended the method of Hughes (1993), to the range of cnoidal waves and undular bores. The method is based on a colocated measuring device which measures at the same location the flow velocity and the surface elevation and is first described in Guza and Thornton (1980). It assumes the following:

- all waves are of constant form
- both the period and the wave height of the incident wave are known
- all harmonics at the multiples of the primary frequency are bound to the incident primary wave
- all reflected waves are linear waves and follow the linear dispersion relation
- there is no interaction between the incident and reflected waves

Based on these assumptions, the total surface can then be approximated as the following:

$$\zeta = \zeta^+_{primary} + \sum_{n=2}^{N} \zeta^+_{n,bound} + \sum_{n=2}^{N} \zeta^-_{n,free} \tag{3.19}$$

Where:

- ζ^+ is the incident wave
- ζ^- is the reflected wave

Usually K_t is used as expression for the transmission rate, as the rate of the transmitted wave height over the incoming wave height. As for cnoidal waves the higher harmonics are important in describing the waves, it is more appropriate to use a transmission rate in terms of density energy spectrum, E_t/E_i. Where E is the sum of the incoming, reflected or transmitted wave energy over the frequency range.

The method of Hughes (1993) requires no spacing as long as it is not in the zone of the evanescent waves as Dean (1984) showed, which is a distance of 3 times the water depth. So the output location in front of the structure is 5 times the water depth plus 0.25 L as is shown in Figure 3.10 and 3.11. The output location behind the structure is 5 times the water depth.

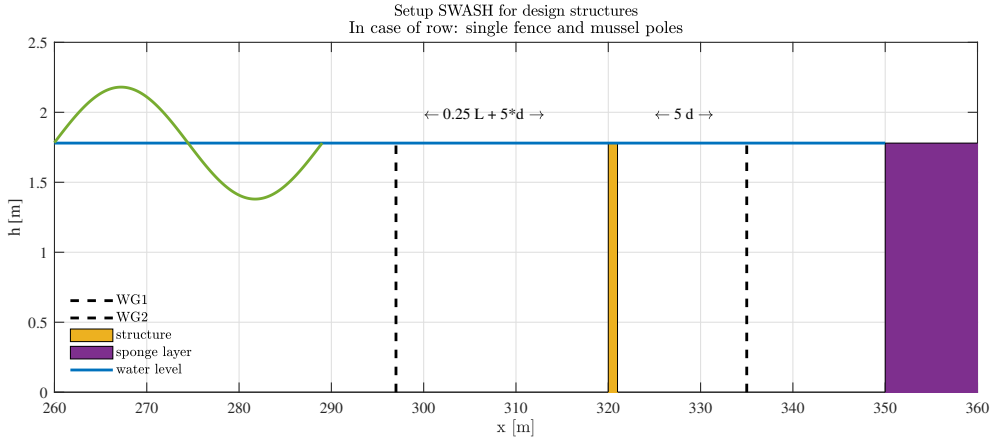

Figure 3.10: Setup of output locations for processing method in case of single fence and mussel poles

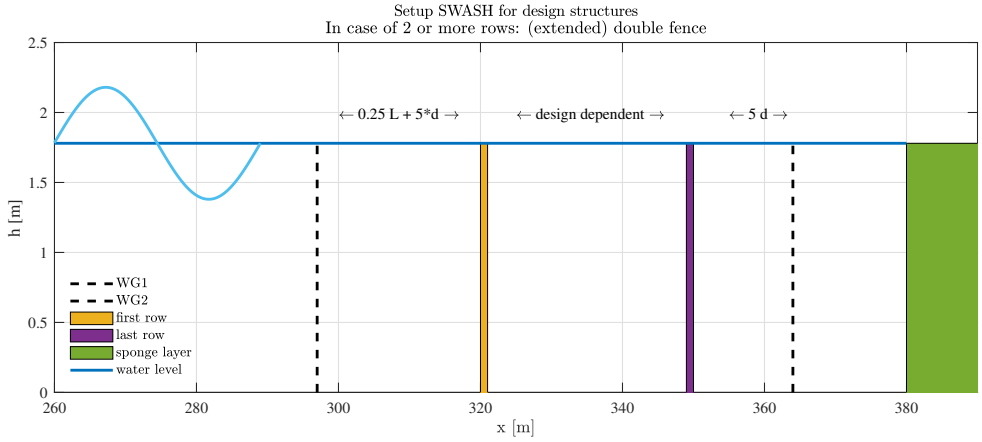

Figure 3.11: Setup of output locations for processing method in case of 2 or more rows.

3.7. Design

In Section 1.1 there are four types of designs proposed: bamboo fences, mussel poles, long/short line and a compound structure. Of these four types, the first two are selected for further studying. The other two designs are not taken into account as the schematization in SWASH requires too much simplicative assumptions to speak of the same design with respect to reality. Therefore the bamboo fences and mussel poles are further developed into four different designs:

1. Single fence, consisting of a single row of bamboo poles.This design enables to study the interaction of waves with an unsheltered structure.
2. Double fence, consisting of two rows of bamboo poles placed with a variable distance s_x. This design enables to study the effect of an increasing row spacing on the wave interaction and how a structure could be able to capture a resonance pattern between two rows of poles.
3. Extended double fence, consisting out two to seven rows of bamboo poles. This design enables to study the effect of multiple rows with a certain row spacing on the transmission of the waves.
4. Mussel poles. This design enables to study the interaction of waves with mussels on vertical poles.

The wave conditions consist of three scenarios:

- Daily wave conditions
- Wave conditions with a return period of 1 year, which is more realistic for the transmission of the waves
- Most extreme wave conditions, resulting in a return period of 5 years

3.7.1. Model setup - Design structures

Grid and boundary conditions

The structures in SWASH are located 10 times the wavelength from the wave making boundary. The boundary condition is a weakly reflective water level time series using Fenton (1988) to have regular waves, as the waves are highly non linear they consist out of 10 harmonic components to accurately describe the shape of the wave. The water depth is constant along the grid and it depends on: the depth with respect to MSL, the surge level and tide. A space discretization of 5 cm is used along with 2 equidistant layers in the vertical, the time step is 0.0001 seconds.

To test the performance of the wave propagation and specifically the higher harmonics the number of equidistant layers is varied as the space discretization is limited by the diameter of the bamboo poles, which is 14 cm. Therefore the space discretization is kept at 5 cm and the number of layers is increased stepwise. A higher number of layers will increase also the computational time.

According to Table 3.3 1 layer should already give an accuracy up to approximately the fourth harmonic, as most of the energy is in the first few harmonics this seems accurate enough. Qua dispersion of the primary components both depths require one layer according to Table 3.2 for an error of 1 %. However by using a weakly reflective boundary condition the higher harmonics could reflect of the structure and then re-reflect of the left boundary if the dispersion is not modelled with enough accuracy. This can be improved by increasing the space discretization, dx, or the amount of layers, however the dx is limited to the size of the bamboo poles. So therefore the dx is kept at 5 cm while the amount of layers is set to two layers in the vertical. As the simulated waves are cnoidal, the waves should not deform and the wave height should be constant along the grid up to the point where the structure is located. This is evaluated on the following output locations: x = 2 L (64 m), 3 L(96 m).

In Table E.2, the characteristics for the reflecting higher harmonics are presented, where assumed is that they propagate following the linear dispersion relation. This is for the wave condition with a return period of 1 year.

Drag coefficient

When using the method of Gijon Mancheno et al. (2021) the calculated $C_{D,b}$ does not reach the steady flow values as in the measurements from other studies such as Chakrabarti (1982), since their measurements covered KC values between 10-22, and they thus did not reach conditions comparable to steady flow. Even for the smallest relative spacing s_x/D = 1.1 of Chakrabarti (1982), the measurements stabilize at an average of C_d = 10 for KC up to 65. This is due to the factor f_{KC}, see Equation 3.14, which assumes a linear relation between KC and the $C_{D,b}$. As KC increases it describes no longer waves but currents and the $C_{d,s}$ (C_d for a single cylinder) should stabilize (Sumer & Fredsoe, 2006, Chapter 4).

In the experiments of Gijon Mancheno et al. (2021) it is observed that from a KC = 13.65 the measured drag coefficient does not increase anymore. The model that they developed would increase the $C_{b,d}$ as it is linearly coupled to the KC number and as the design wave conditions have a KC number around 49-58, the $C_{b,d}$ would be unreasonable high. Therefore the increase in f_{kc} is limited by setting the f_{kc} for values higher than 13.65 as the same as that of KC =13.65.

3.7.2. Stability of the design

The stability of the various designs is evaluated by means of the maximum force. The forces on front poles of the structure are calculated with Equation 2.2 as these are the most exposed. The flow velocity is assumed to be uniform over the height and equal to flow velocity at the water surface, which is a conservative approach. The following are not taken into account:

- Breaking waves. With the top of the poles at the level of MHW + surge of 1 year, the only waves in this study that can give an extra force due to wave breaking are the daily wave conditions. However these are also the most mild wave conditions, so it is not expected that this will lead to substantially higher forces.
- The poles are slender (D/L < 0.05), therefore the difference of water level over the pole is assumed to be negligible
- Influence of currents, since the measured currents were below 0.3 m/s at the location of the structures

The maximum waves that give the maximum force on the poles are calculated using the Battjes and Groenendijk (2000) method for shallow water conditions. The maximum wave is chosen to be $H_{0.1\%}$.

3.7.3. Design performance

The designs have various functions, so to determine the performance and the variability the functions are separately assessed. The designs are assessed on the following functions:

1. Wave damping
2. Available surface for mussels
3. Stability

3.7.4. Mussel poles

Theophanatos (1988) states that the increase in drag force by marine growth is dependent on the following: orientation to the flow, non-uniform thickness, distribution, percentage surface cover, size of marine growth and overall thickness. It is however not possible to specify all these parameters in SWASH as only the diameter and the drag coefficient can be used. Therefore the following assumptions/simplifications hold:

- orientation to the flow is neglected as this would mean that the individual mussels can be specified and this is not possible in SWASH,
- the thickness, distribution and percentage surface cover are assumed to be uniform over the length of the pole where the mussels can be present, so between MLWS and below 40 cm from the bed mussels are for 100 % present but outside these two levels none at all.
- the size of the mussels can vary during their lifetime, as the mussels are regularly harvested the size of the mussel at a certain time is assumed to be uniform as it is assumed they all grow with the same rate.

Combining these assumptions it is assumed that the effect of mussels can be represented by a round surface with a increased drag coefficient with respect to a smooth surface.

4

Results

4.1. Introduction

This chapter contains the results of this thesis. It starts with an analysis of the hydraulic boundary conditions in Section 4.2. Then it describes the performance of several methods that process the output of SWASH in Section 4.3.Section 4.4 describes the calibration of SWAN. In Section 4.5 the results of the validation of SWASH are presented. In Section 4.6 the wave transmission of the various designs is explained.

4.2. Boundary condition analysis

Defining the design conditions requires analyzing time series of local offshore wave conditions for several years. Firstly the existing datasets are identified and compiled in a repository. Section 4.2.1 presents a comparison between wave data from WaveWatch III and local wave measurements from Van Bijsterveldt and Bouma (2021). Section 4.2.2 explains which waves are selected from the data of the WaveWatch III. Section 4.2.3 shows how these selected waves are extrapolated for defining the offshore design wave height. Section 4.2.4 explains how the design wave period is determined. Section 4.2.5 presents the offshore design waves.

4.2.1. Validation of WaveWatch predictions

The two periods of measurements of the Wavedroid are used to validate the 12.5 years of WaveWatch data. The following figures are for the period of November - December 2017 as in this period there was quite a large storm measured. The other period of measurements, in 2018, contains only measurements of mild wave conditions.

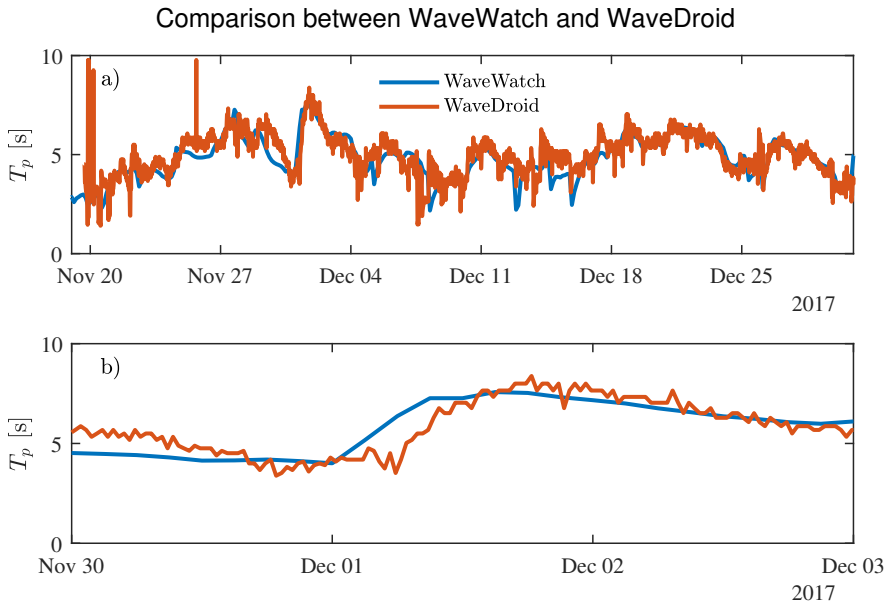

Figure 4.1: Peak periods measured by the WaveDroid and predicted by WaveWatch. a) T_p from 19 November until 30 December, b) T_p around storm event of 1 December. There is a good agreement observed between the data from WaveWatch 3 and the WaveDroid

As shown in Figure 4.1 predictions and measurement show the same pattern. The measurements show generally higher values, reaching up to 8 a 8.5 seconds, whereas the WaveWatch predictions shows maximum values up to 7.5 seconds, so the predictions slightly underestimate the peak period.

The measurements of H_{m0} show a good agreement with the predictions from WaveWatch, see Figure 4.2.

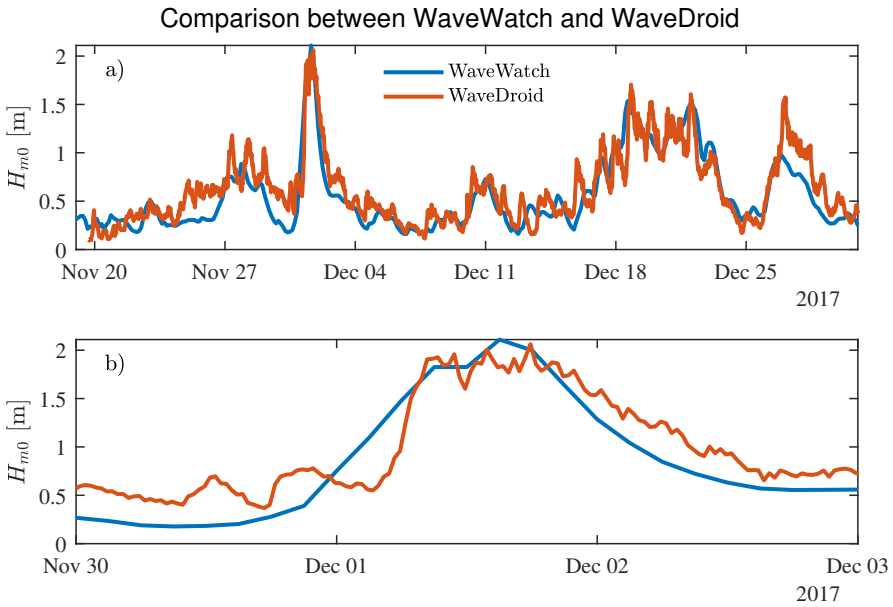

Figure 4.2: H_{m0} measured by the WaveDroid and predicted by WaveWatch. a) H_{m0} from 19 November until 30 December, b) H_{m0} around the storm of 1 December. The data from WaveWatch has in general a good agreement with the measurements.

The WaveWatch wave direction is quite constant around 300 degrees around this period whereas the measurements show a more fluctuating pattern around a slightly higher wave direction, see Figure 4.3. This fluctuating pattern is due differences in the frequency of the datapoints, the WaveDroid generates output every 0.5 hrs whereas the WaveWatch predicts every 3 hr. This causes that the WaveDroid captures the local sea/land- breeze, which occurs daily in the afternoon, but this process is not included in the WaveWatch data.

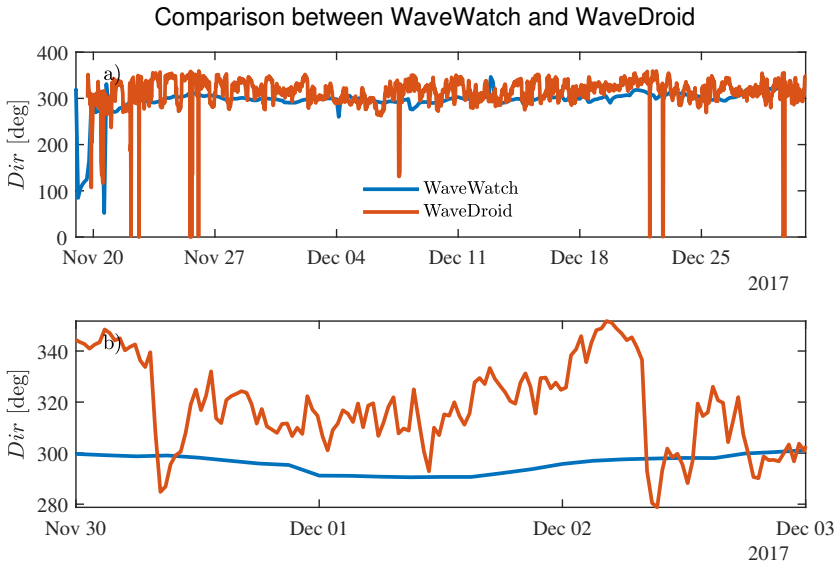

Figure 4.3: Wind direction(Nautical) measured by the WaveDroid and predicted by WaveWatch, for a period of a) 20 November -31 December and b) 30 November - 3 December. The wave direction by WaveWatch has a more constant value than the measurements by the WaveDroid, which shows a more fluctuating pattern. This comes due to frequency of the datapoints.

Although the WaveWatch data does not include local wind waves, it does reproduce well the monsoon conditions (which are much larger in Demak, and thus define the structure design) and therefore the WaveWatch data is considered suitable for the statistical analysis of the extreme conditions.

4.2.2. Selecting the relevant storm wave conditions

WaveWatch predicts waves in all directions but only the waves that could reach the coast of Demak are relevant. The coast of Demak has a shoreline normal of 301 degrees (Nautical). From the Figure 4.4 it can be clearly seen that there is a peak around 300 degrees with high waves. A bandwidth of 40° around the shore normal is selected to cover the most severe wave conditions over the years.

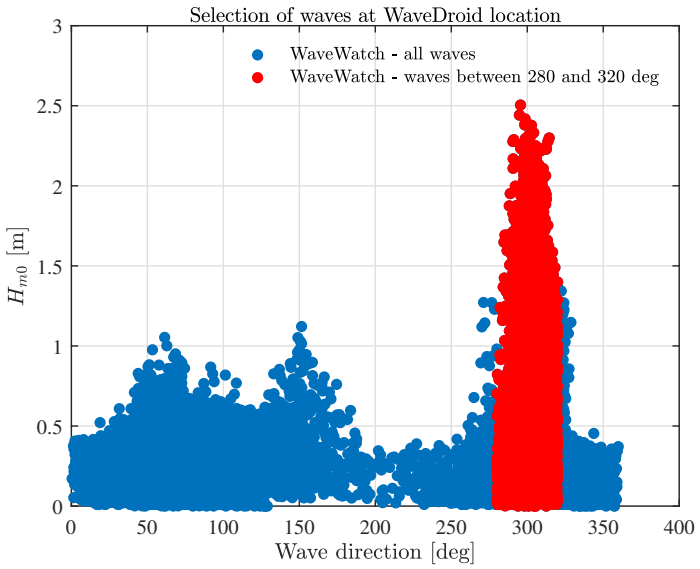

Figure 4.4: Wave heights and wave directions from 2007-2019 from WaveWatch, with a band width of 40 °. There are clearly three peaks visible around 50, 150 and the largest around 300 degrees. The last one is the relevant one and contains the waves that can reach the coast of Demak.

The band width is assumed to be 280-320 but to verify if the selected direction is sensitive to changes, the band width is varied to 290-310 and 270-330 degrees. For the case of 270 – 330 degrees the number of storms per year is exactly the same as for the case of 280 – 320, $N_s = 6.88$. This indicates that within this wider ranger there are no storms that have been missed and which could have be relevant for determining the wave characteristics offshore.

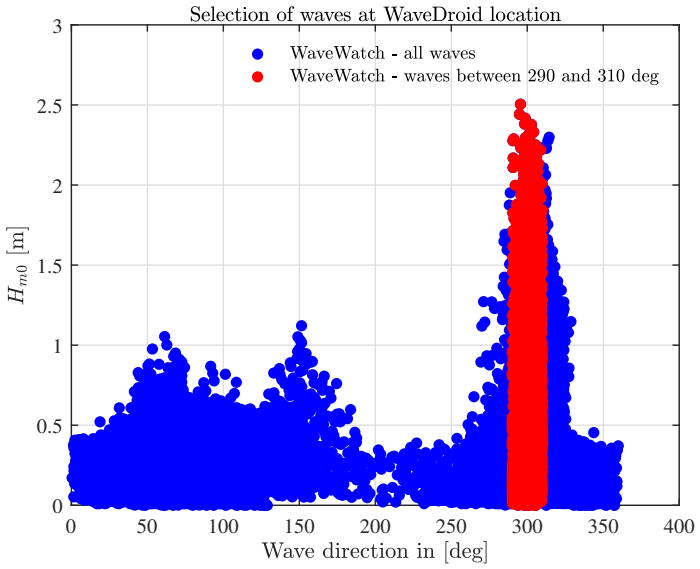

Figure 4.5: Wave heights and wave directions with a band width of 20° instead of 40°. There are clearly some of the higher waves missing with this narrow band width.

For the case of 290 – 310 degrees the number of storms per year (6.16) is slightly lower and the result of this is shown in Figure 4.5. It can be seen in Figure 4.5 that due to the smaller band width waves up 2.2 m approximately are missed out if this range is selected for further use. By reducing the band width a consider-

able fraction of extreme storm events are neglected. Therefore, we use the range between 280 – 320 degrees for further analysis.

After the wave conditions are selected based on the wave direction in the previous steps, the wave conditions have to be further filtered based on wave height. Table 4.1 shows the results of the Peak over threshold method for the different combinations of wave height and the period between successive storms. It can be seen that all of the combinations of the periods between successive storms and wave height threshold (except D= 48, H = 1.0) fall in the recommended range of Ns = 2- 10.

Threshold H	N_s for D =48 hrs	N_s for D =72 hrs	N_s for D =96 hrs
[m]	[storms/year]	[storms/year]	[storms/year]
1.5	4.96	4.32	3.84
1.4	6	5.2	4.64
1.3	6.88	5.76	5.12
1.2	8.24	6.56	5.76
1.1	9.6	7.36	6.4
1	10.96	8.32	7.36

Table 4.1: Number of storms for different thresholds in time and wave height. D in this case is the duration between two successive storms.

4.2.3. Extrapolation of the dataset

The Peak over threshold method produces a dataset of wave heights. For design purpose it is important to be able to tell which wave height belongs with which return period. This is done by using four different distributions functions: Exponential, Weibull, Gumbel and Generalised Pareto. The equations of the distributions are provided in Appendix A. The predictions of the distributions are compared against the dataset of the P.o.t. method in terms of RMSE, see Equation 3.2.

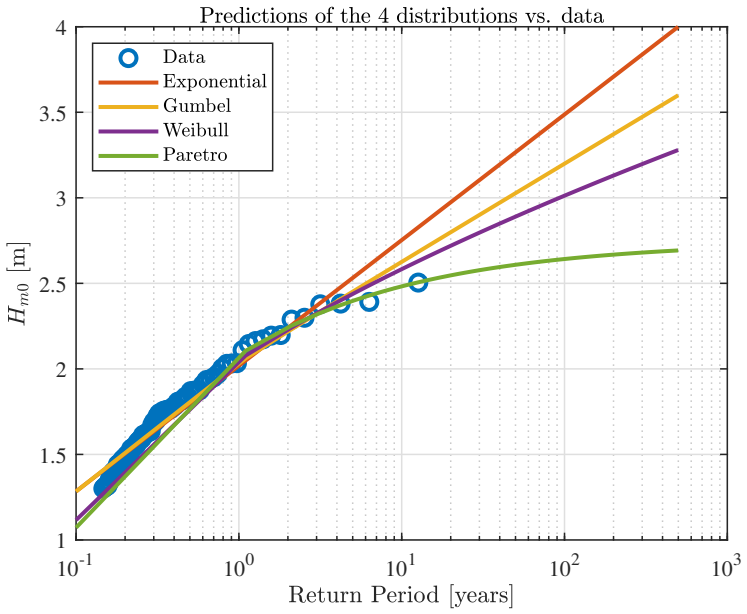

Figure 4.6: Performance of 4 distributions against the data from P.o.t., where the Pareto distribution(green) has the best fit.

As can be seen in Figure 4.6 the Generalised Pareto distribution has the best fit.

Distribution	RMSE	A	B	α
General Pareto distr.	0.0184	0.6249	1.3261	-0.4
Weibull distr	0.0225	0.5374	1.2360	1.57
Gumbel	0.0349	0.2486	1.5755	[-]
Exponential	0.0688	0.3189	1.4033	[-]

Table 4.2: The performance of the 4 distribution functions with descending RMSE, where A, B and α are the parameters as in Equation A.3

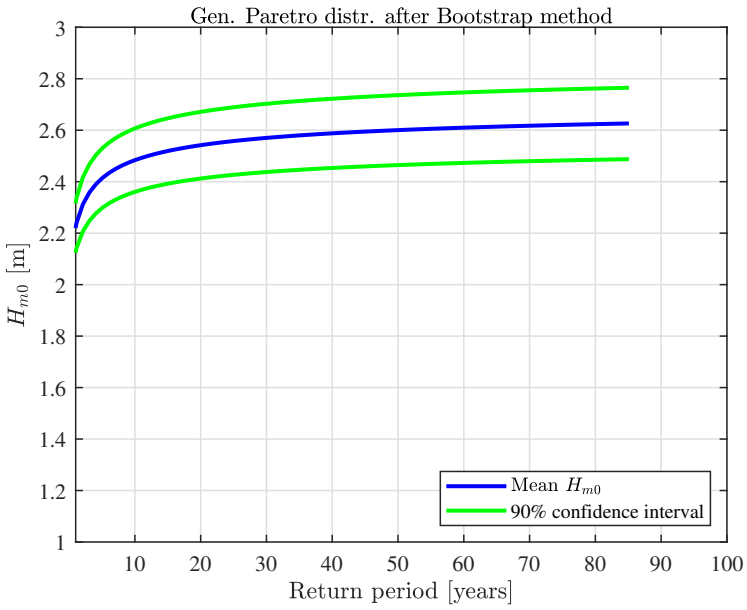

Figure 4.7: Prediction of wave height with 90 % confidence interval

To check the sensitivity of the time between successive storms the results of the three different times between successive storms are compared along the same wave height threshold, that of H_{m0} = 1.3 m. For the largest return period the wave heights only differ a few cm's corresponding to a maximum difference of 5.3%. To check the sensitivity of the wave height threshold, this is varied along the same time between successive storms(48 hours) with the values of H = 1.2 m and 1.4 m. For the three different thresholds the confidence intervals only differ a few cm's. See Appendix A for more information. So as a result the data of a time between successive storms of 48 hours and a wave height threshold of 1.3 m is used for the offshore wave characteristics.

4.2.4. Wave periods

In order to fully define the design wave conditions, a wave period needs to be associated to the wave height values derived from the previous section. The selected wave heights after the Peak over threshold method correspond with wave periods between 5 and 7.5 seconds, which can be seen in Figure 4.8.

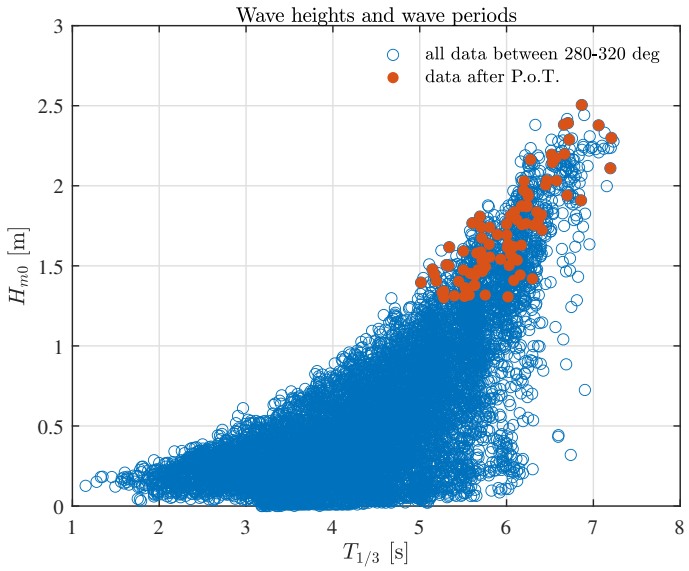

Figure 4.8: Selected wave heights and periods after P.o.t.

By fitting the predictions of WaveWatch through the Equation 3.4 a value for a is found, a = 4.6317 with a standard deviation of 0.2335, see Figure 4.9 for visualisation. This gives a wave steepness of 0.03 which is

according to Van den Bos (2018) in range between developed wind sea and short swell sea-states.

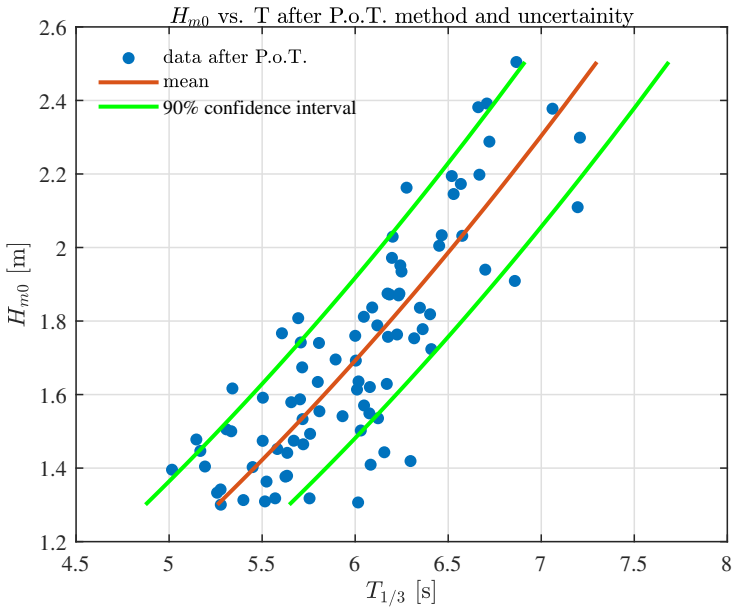

Figure 4.9: Set of wave heights and wave periods after the Peak over threshold within a 90% confidence interval.

4.2.5. Offshore design waves

In Table 4.3 the wave periods and wave heights for each return period can be found to summarize the wave characteristics that are used for the design storm conditions.

R	H_{m0}	St. dev.	Lower bound.	Upper bound.	T_p	Lower bound.	Upper bound.
[years]	[m]	[-]	[m]	[m]	[s]	[s]	[s]
1	2.08	0.0483	2.00	2.16	6.9	6.6	7.4
5	2.39	0.0671	2.28	2.50	7.5	7.0	7.9
10	2.47	0.0724	2.35	2.59	7.7	7.3	8.0
15	2.51	0.0749	2.39	2.63	7.7	7.3	8.1
20	2.53	0.0765	2.41	2.66	7.7	7.3	8.1
50	2.59	0.0805	2.46	2.73	7.8	7.4	8.2

Table 4.3: H_{m0} and T_p with their 90% confidence intervals for a storm of 48 hours and a wave threshold of 1.3 m. Note that $T_{1/3}$ from Figure 4.9 is transformed to T_p according to Equation 3.4

4.2.6. Tide

Tas et al. (2020) measured the water level in front of a chenier along a transect with three pressure sensors. In their tidal analysis they found the following constituents, see Table 4.4. These give a form factor of 1.72 and can be classified as mixed, mainly diurnal and the tide is characterized by two distinct spring neap cycles overlapping twice a year. Smits (2016) shows in the same table slightly different tidal constituents and thus a different form factor of 2.4, but indicates also that the tides have a mixed signal with mainly diurnal characteristics and small semi diurnal components.

Tidal constituents:	M_2	S_2	N_2	K_2	K_1	O_1	P_1	M_4	MS_4
Amplitudes in [cm]:									
according to Tas et al., 2020	0.10	0.08	-	-	0.22	0.08	-	-	
from Smits, 2016	0.075	0.059	0.02	0.013	0.214	0.11	0.07	0.006	0.01

Table 4.4: Tidal constituents from two studies, (Tas et al., 2020; Smits, 2016)

Tas et al. (2020) indicates a mean spring tidal range of 1 m and Smits (2016) indicates a spring tidal variation of 0.6 m and a neap tidal variation of 0.4 m.

So the predicted signals in the following figures are based on the measured signals at transects E and A, see Figure 3.3, at a latitude of -6.8982 with the four tidal constituents from Tas et al. (2020): O1, K1, S2 and M2.

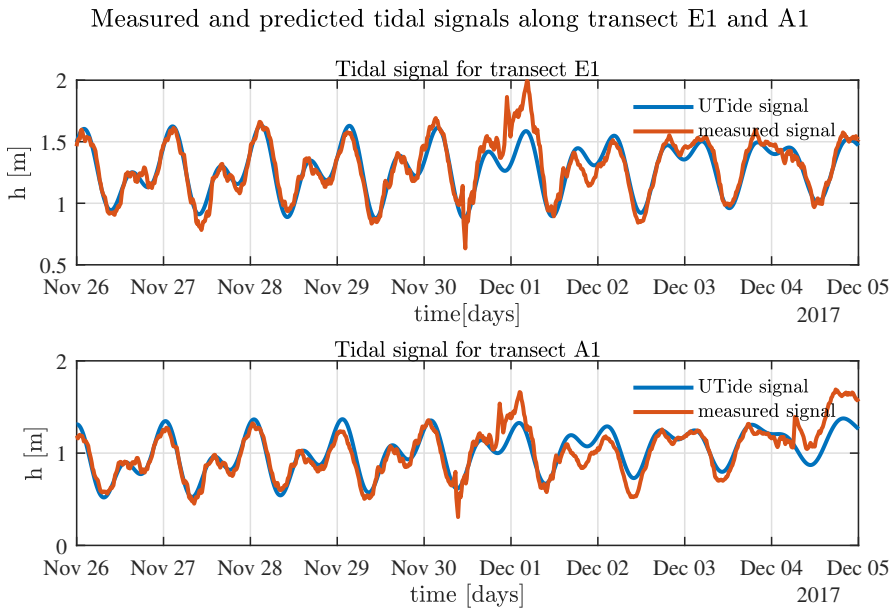

Figure 4.10: Tidal signals at the most seaward point of transects E and A, see Figure 3.3

Figure 4.10 shows a good agreement between the measurements and predicted signal by UTide. Around 1st of December the storm event can be clearly seen in the water level: first in the drop in the water level just before the storm and then the increased water level during the storm.

When simulating the tidal signals for a duration of 3 months with the tidal coefficients in Utide, the maximum tidal variation is 0.85 m and the minimum is 0.50 m. This is in the same order as Tas et al. (2020), Smits (2016), and Ningsih et al. (2011). The tidal levels are summarized in Table 4.5.

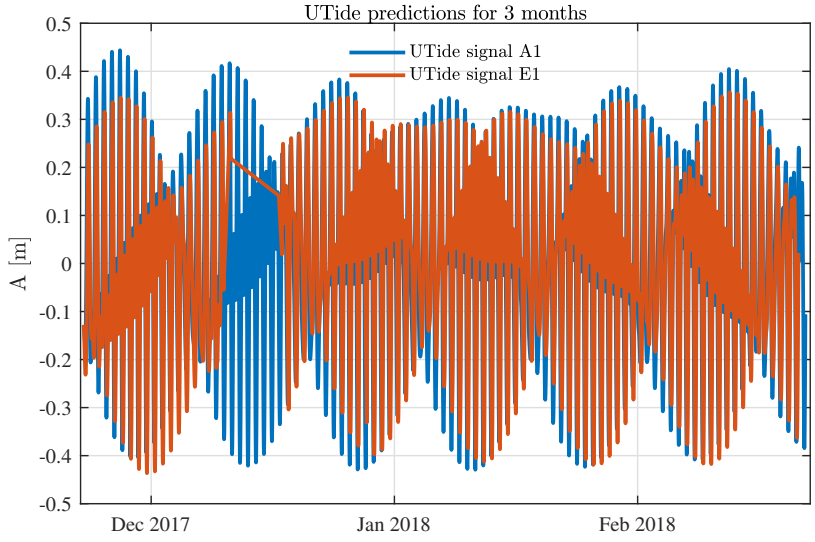

Figure 4.11: Predictions of a tidal signal along two transects by Utide (Codiga, 2011)

Tidal levels	MHWS	MHW	MHWN	MLWN	MLW	MLWS
[m] w.r.t. MSL	+0.42	+0.35	+0.25	-0.25	-0.35	-0.42

Table 4.5: The tidal design levels with from left to right, in consecutive order from high to low.

4.2.7. Surge

In Figure 4.12 before the peak of the storm there is a sharp decline visible in the water level, this is caused due to high pressure area in front of the storm. Whereas during the time of the storm the highest water level coincides with a peak in the tidal level. To determine a surge from this signal the difference between the predicted and measured signal is used, as Utide is not capable of determining surge levels and ignores those high peaks as long those do not occur with the same frequency as the tides. The average extra water level during the storm at A1 is 0.2 m with a peak of 0.5 m. The average extra water level during the storm at E1 is slightly higher than at A1 and is estimated as 0.25 m with a peak of 0.6 m.

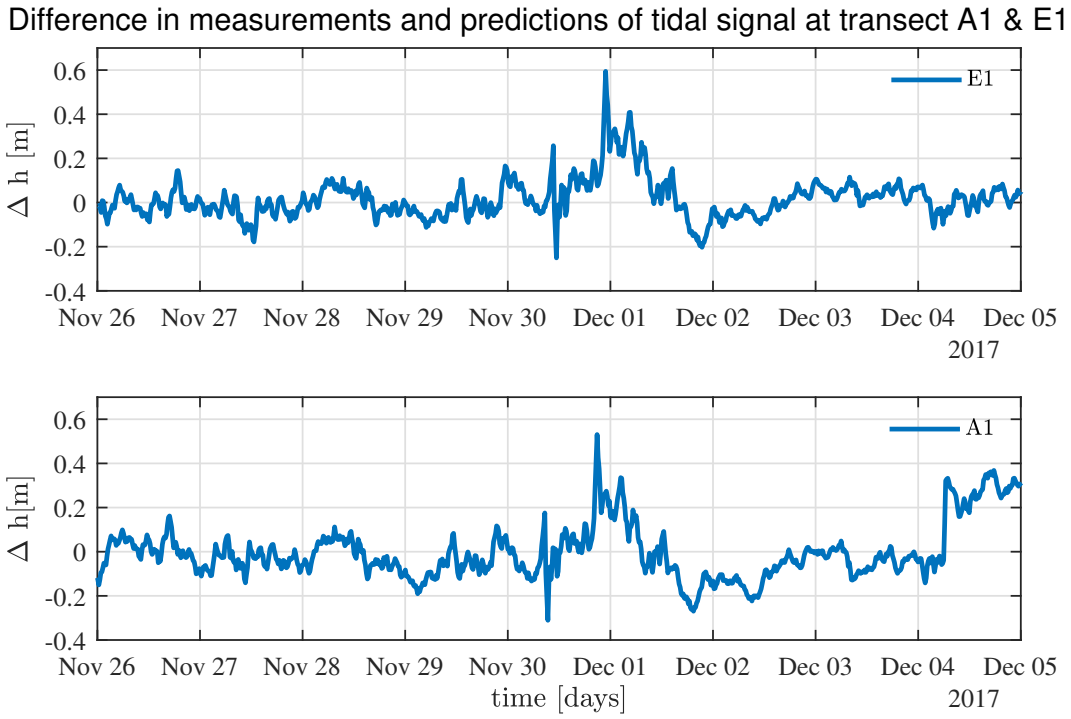

Figure 4.12: Difference between the predicted and measured tidal signal along the two transects from Figure 3.3 to distinguish the surge.

Suroso and Firman (2018) suggests a value of 41 cm. As part of a risk assessment of the North coast of Java (Willemsen et al., 2019) translated oceanic surge levels from the DIVA model (Hinkel & Klein, 2009) to segments along the coast of Java. In Figure 4.14 the surge level with respect to return period of three of those segments near Semarang is shown.

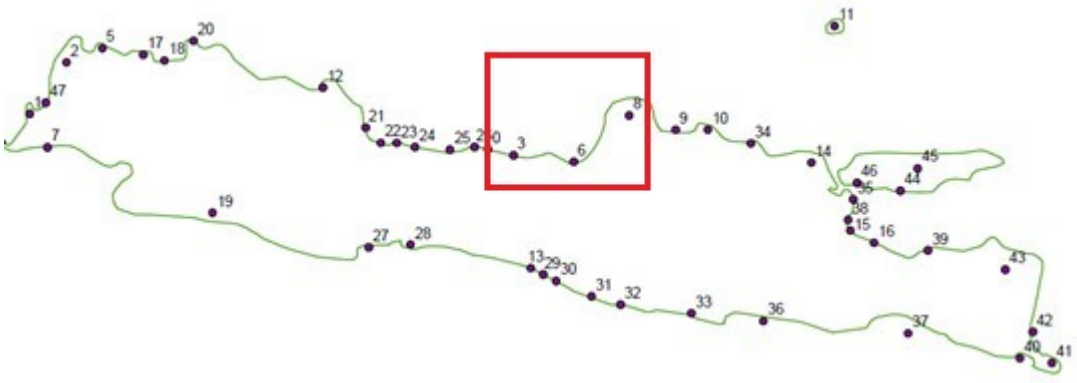

Figure 4.13: Locations output stations with in red the project location, number 6 is the station in Semarang

Subsidence

Abidin et al. (2013) suggests an average subsidence rate of 6 a 7 cm per year in the city of Semarang but states that the subsidence rates are higher 7 to 11 cm a year to north of the city, as the soil is mainly composed out

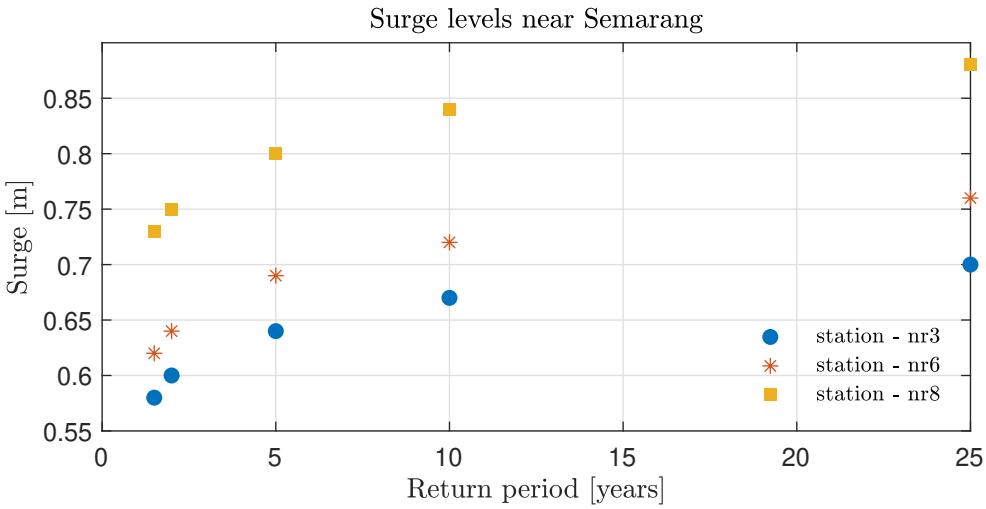

Figure 4.14: Surge levels for three stations around Semarang from Hinkel and Klein (2009), where station nr 6 is the station at Semarang, as is shown in Figure 4.13

of alluvial deposits. For the structures to be build this would mean, for a lifetime of 5 to 10 years, an increased water level or decreased bottom level of 45 or 90 cm.

4.2.8. Nearshore wave measurements

The waves in the nearshore are measured along transects A and E, see Figure 3.3. Figure 4.15 shows the measured wave height, water depth and wave period offshore at A1 and E1. A small time delay is observed between the measurements at E1 and A1 approximately equal to 2 hours. This could in principle be caused by the distance between the two measurement locations, but this is not realistic for the separation which in this case is in the order of hundreds of meters. Secondly, the duration of high wave heights offshore is clearly longer than in the nearshore this can be explained by the decrease in water level at 1 December around 04.00 at E1, which limits the maximum waves that can propagate across the profile. Next to this the offshore highest wave height occurs quite late in storm whereas in the nearshore this happens earlier as the waves are depth limited and actually during the lowest wave height during the storm. Thirdly, the peak period offshore during the storm is in general smaller than at E1 at A1 as should be due to the effect of a smaller depth. As during the propagation of the waves in shallow water, the peak frequency shifts to a lower frequency due to the wave – wave interactions, bottom friction and depth – induced breaking.

As the waves at the location are depth dependent an estimate has to be made for case of the joint probability of high waves and high water levels. In the Java sea swell waves cannot exist so the high waves can only be generated by local storms. The mean spring tidal amplitude at the location is in the same order, 0.5 m, as the predicted surge levels for a return period of 1 year as is shown in Figure 4.14. Therefore the high waves can only exist with a high tide and a certain surge level, as with low tide the surge and tide cancel each other out. As the high waves and surge are generated by the same source, a storm, they are strongly correlated. The joint probability of high waves and high water narrows thus down to occurrence of storms and high tides. As the tides in Demak are mainly diurnal, see section 4.2.6, and the storm duration is usually 12 hours or longer, the probability that they would coincide on the same day is 1. As result of this, the joint probability of high waves and high water is only depended on the number of storms per year. Practically speaking this means that a wave with a return period of 1 year occurs with a surge level with a return period of 1 year, which is shown in Table 4.6.

Return period (years):	1	5	10	15	20
Offshore Waves (H_{m0})	2.08	2.39	2.47	2.51	2.53
Surge	0.63	0.68	0.72	0.74	0.76

Table 4.6: Wave heights and surge levels for return period from 1 to 20 years.

4.2.9. Daily wave conditions

In the earlier sections the storm wave conditions were identified to determine the design wave conditions, in this section the daily wave conditions are determined. In a measurement period from the 22nd to 29th November 2018 in the BioManCo project, Jansen (2019) H_{m0} = 0.05 -0.015 m and $T_{1/3}$ = 3-5 s around an

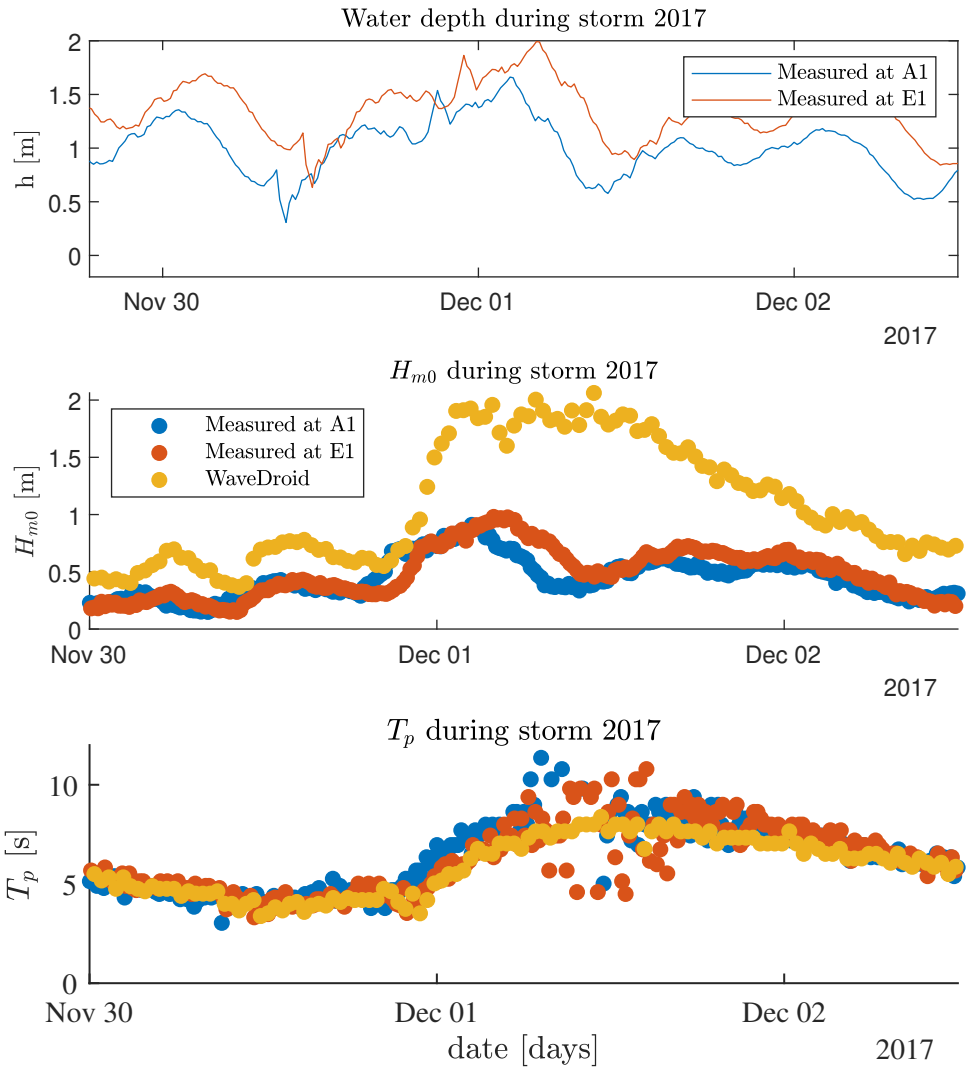

Figure 4.15: Comparison between offshore and nearshore measurements. Up) waterdepth in the nearshore along transects A and E, see Figure 3.3. Middle) H_{m0} offshore measured by WaveDroid Tas et al. (2020) and nearshore along transect E and A. Lower) Peak period offshore by the WaveDroid and nearshore along transects E and A.

average depth of 1.2 m in front and behind a structure made of vertical poles without brushwood. In this period it can also be seen that the highest waves in this period still have low wave periods, indicating that these are locally generated. The timing of these high waves often occurs in the late afternoon, indicating that this may be caused by the sea breeze, in agreement with the observations by Tas et al. (2020) who measured a week later in the same area. She also observed that in this period the only onshore waves were the waves that were generated by the seabreeze. For the onshore directed waves she observed slightly higher waves than Jansen (2019) reported, namely H_{m0} = 0.15 - 0.3 m and T_p = 2-3 s. Therefore, from now on the following values are used as design values for the daily wave conditions:

- H_{m0} = 0.25 m
- T_p = 3 s

4.3. Process techniques: Performance with an imposed reflection

In able to process the outcome of SWASH accurately two methods are evaluated to determine which method provides the best measurement of an imposed situation. The first one is based on the surface elevation and the second method is based on surface elevation and flow velocities.

4.3.1. Process techniques based on surface elevation

For evaluating the methods based on surface elevation, five situations are created: linear waves, nonlinear waves, the wave conditions of the experiment of Jansen (2019), daily wave conditions and design wave conditions. These five situation are evaluated with the methods of Goda and Suzuki (1976) and Mansard and Funke (1980).

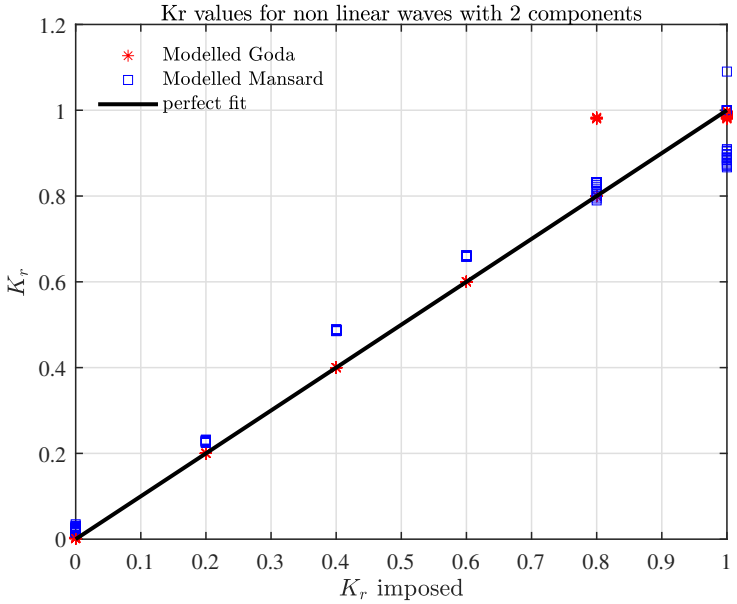

Figure 4.16: Comparison for the case of non-linear waves between Goda and Suzuki (1976)and Mansard and Funke (1980)

Figures 4.16 and 4.17 show that the script of Mansard and Funke (1980) tends to give consequently higher values than the exact value. Goda and Suzuki (1976) does give the exact value even when the non-linearity of the waves increase, except for one case.

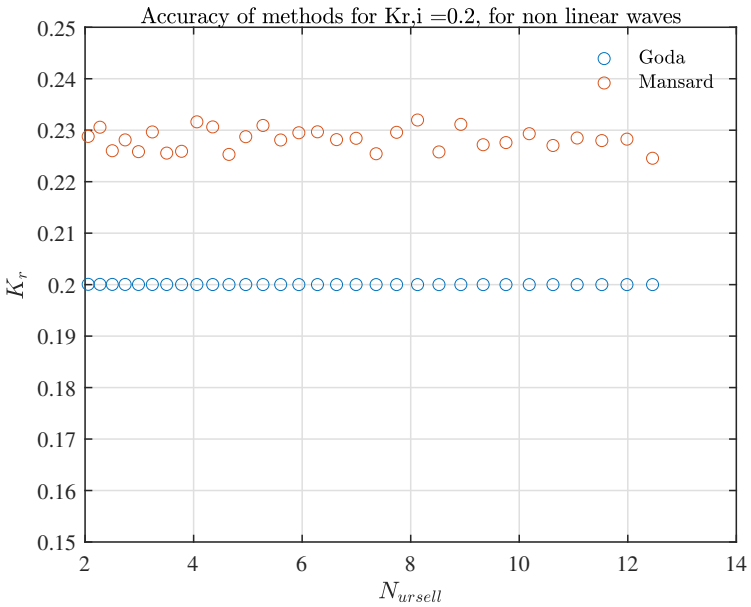

Figure 4.17: Comparison for the case of non linear waves, for an imposed K_r = 0.2 between Goda and Suzuki (1976) and Mansard and Funke (1980)

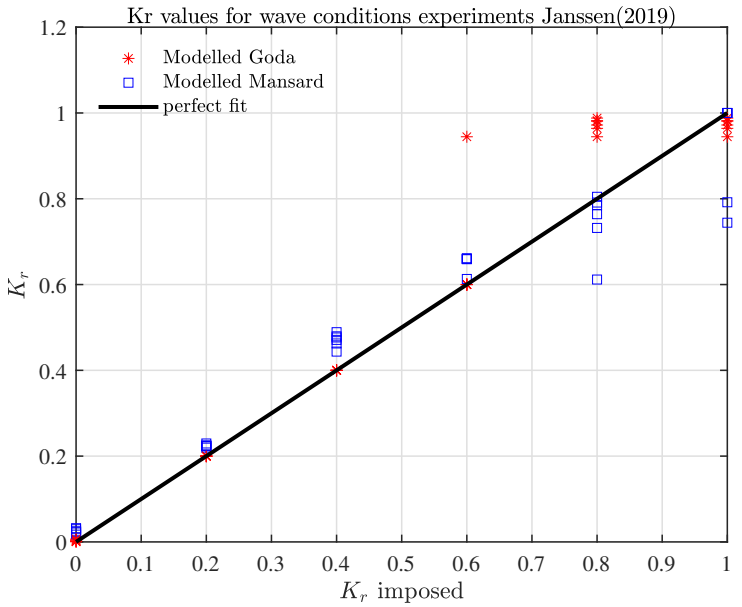

Figure 4.18: Comparison for the case of waves of experiment by Jansen (2019) between Goda and Suzuki (1976)and Mansard and Funke (1980)

Figure 4.18 shows that for:

- $K_{r,i}$= 0 both methods perform well
- $K_{r,i}$= 0.2 up to 0.6, predicts the exact value for most of the cases and Mansard and Funke (1980) is slightly higher than the exact values
- $K_{r,i}$= 1, both methods predict lower values than the exact ones.

4.3.2. Conclusion

In the range of interest, K_r = 0.0 - 0.4, Goda and Suzuki (1976) has the best performance for both linear and non linear waves. Mansard and Funke (1980) estimates in this range consequently a higher value than the imposed reflection coefficient both for linear and non linear waves. For a highly reflective structure in the

range of K_r = 0.6 -1 both methods could be used for linear waves but for non linear waves the results should be carefully considered. For the design stage, the waves are cnoidal and cannot be measured accurately with either Goda and Suzuki (1976) or Mansard and Funke (1980). Therefore the method of Dekkers (2018) is used.

4.4. SWAN Calibration

4.4.1. Introduction

SWAN is calibrated to reproduce the same wave characteristics during the storm event around 1 December 2017. In Section 4.4.2 the results are shown. In Section 4.4.3 the results of a sensitivity analysis of the used parameters in Section 4.4.2 is shown.

4.4.2. Calibration on storm event

The parameters that have been used in the calibration are: the breaking parameter, wind velocity, directional spreading and friction. See Table 4.7 for the values. The result of this calibration is shown in Figures 4.19 and 4.20. From 30 Nov 12.00 to 1 December 0.00 the measurements don't match, this is probably due to a different wind speed as the water levels do match well. As the wind velocity is kept constant at 12 m/s in SWAN, whereas in reality the wind velocity would fluctuate more. From 1 December 0.00 to 12.00 the measurements and SWAN results have a good agreement.

Parameter	Sign	unit	value
Dir. spreading	$\Delta\theta$	θ	15
Breaking	γ	-	0.55
	α	-	0.1
Friction	C_{bfr}	$\frac{s}{m}^{(1/3)}$	0.019
Wind	U10	m/s	12

Table 4.7: Calibration parameters used as input in SWAN

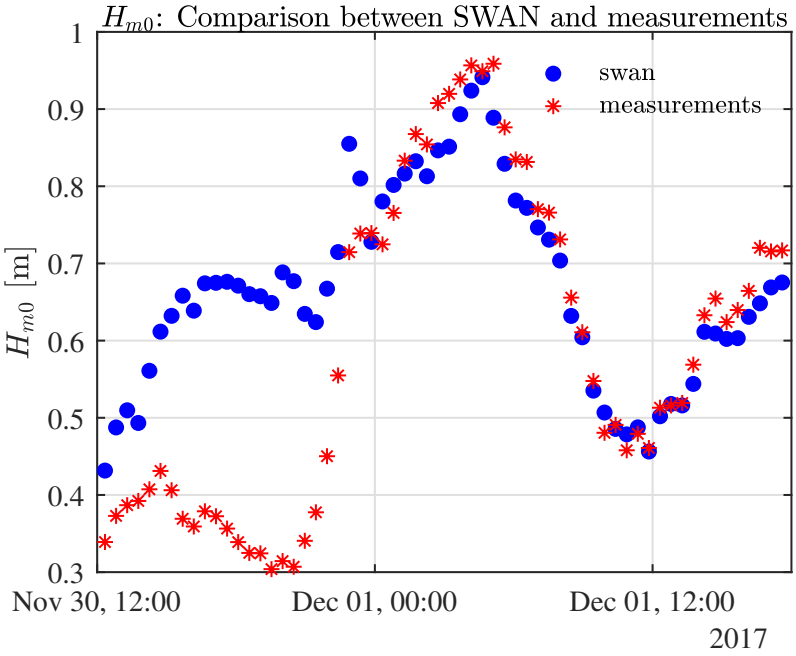

Figure 4.19: Comparison between a measured H_{m0} and calculated by SWAN at the measurement location as in Figure 3.4. It can be observed that the agreement between simulations and measurements after 1 Dec, 00:00 good is. Before that time the wind velocity in reality is significantly lower than the constant wind velocity that was used as input in SWAN.

4.4.3. Sensitivity analysis

During the calibration of SWAN a sensitivity analysis of the physical parameters was carried out. The parameters and values that are used in the sensitivity analysis are presented in Table 4.8.

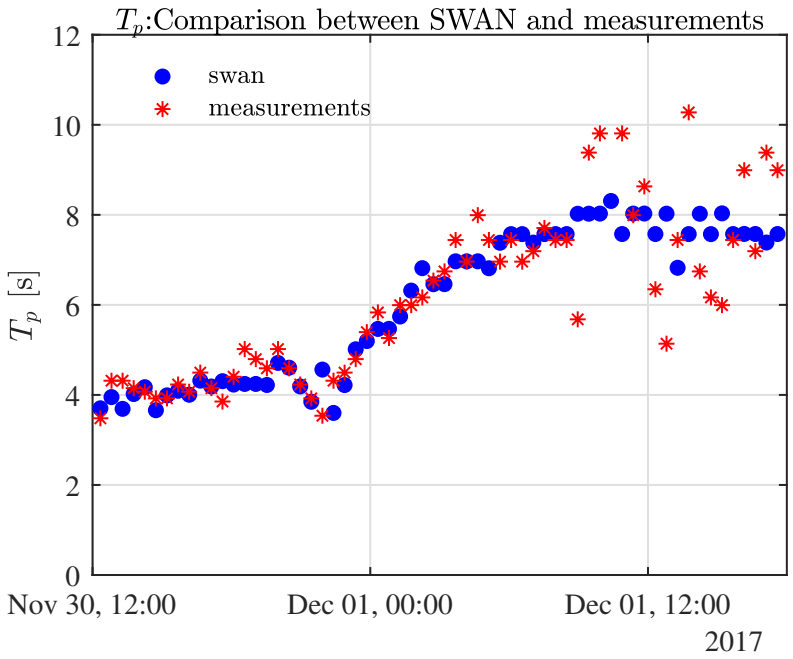

Figure 4.20: Comparison between a measured T_p and calculated by SWAN at the measurement location as in Figure 3.4. There is a good agreement between simulations and measurements up to 1st December, 12:00 where the measurement become scattered but the SWAN simulations are the mean of it.

Parameter	sign	unit	value(s)
Dir. spreading	$\Delta\theta$	°	10 and 25
Breaking	γ	[-]	0.5 and 0.6
	α	-	0.05 and 0.2
Friction	$c_{b,fr}$	$\frac{s}{m}^{(1/3)}$	0.038
Wind	U10	$\frac{m}{s}$	10 and 15

Table 4.8: Used parameters in the sensitivity analysis of SWAN.

Breaking

Wave breaking can be modelled by a tuneable factor α and constant breaking parameter(γ) or based on the wavenumber and the slope. The dissipation by wave breaking is schematized as the dissipation of a bore (Holthuijsen, 2007):

$$D_{surf,wave} = -1/4\alpha\rho_w g f_0 H_{max}^2 \tag{4.1}$$

Where:

- α is a tuneable factor with a default of 1
- f_0 is the frequency of the wave
- $H_{max} = y_{br}(d+\zeta)$
- y_{br} is the breaking parameter
- d is the still water depth in [m]
- ζ is the wave setup in [m]

For gentle slopes the breaking parameter never exceeds $\gamma = 0.55$ (Holthuijsen, 2007), so that is used as a first estimate as the slope is very gently (1:500). It is varied between $\gamma = 0.5$ and 0.6. In Figure C.4 it can be seen that during the peak of storm a higher $\gamma = 0.6$ does not lead to higher waves but the values stay equal to that of $\gamma = 0.55$, the lower γ does result in lower wave heights. The tuneable factor α has a default value of 1, this proved to be too high and therefore a lower value of 0.1 was used. To see how sensitive this factor is, it is varied to values of 0.05 - 02. In Figure C.5 it can be seen that this factor is highly influential as the range between under the peak of the storm is 30 cm, whereas for instance around 30 November 18.00 this is only 0.10 cm.

Friction

The sediment type determines the amount of friction and is therefore an important factor of wave dissipation. The default bottom friction coefficient in SWAN is a Manning coefficient of 0.038 s/m1/3 for all kinds of sea states, for smooth seafloors a value of 0.019 is suggested in the Manual. A value of 0.019 is used as first estimate and compared with the higher default value of 0.038, next to this also a frictionless case is studied.

Wind velocity

The wind velocity is chosen such that the waves are constant along the deep water part of the bathymetry. To check the sensitivity of the wind velocity, a higher and lower value of 15 and 10 m/s is used. In Figure C.2 it can be seen that during the peak of the storm the wave height is not that sensitive to a different wind velocity. At the start of the storm, between 30 November 14:00 to 20:00, the variability in wave height is larger.

Directional spreading

The directional spreading is dependent on the sea state, the peak of storm can be either be classified as young swell or a developed wind sea.Smits (2016) uses a directional spreading of 10 degrees during a storm event and 15 for non monsoon events in his SWAN model for the wave modelling at the coast of Demak. This seems to narrow for the Javasea, as it would correspond with long or young swell. As this is only an indication two directional spreadings are compared with the base case of 15 °, 10 and 25 degrees, respectively.

In Figure C.3 it can be seen that a different directional spreading, either $\Delta\theta$ = 10 or 25 ° does not change the wave height during the peak of storm, the largest variability can be seen at the start of the timeseries.

4.5. SWASH: Validation of wave transformation through structures

4.5.1. Introduction

As setup for the design stage of this thesis, the experiments of Jansen (2019) are used to validate SWASH in the performance of the wave transformation through structures. In Section 4.5.2 the boundary conditions are evaluated. In Section 4.5.3 the use of the vegetation module in SWASH is explained and how to use it to find a good agreement with the experiments.

4.5.2. Boundary conditions

There are two methods to describe the wave conditions of Jansen (2019): Stokes' theory and the streaming theory by Fenton (1988).

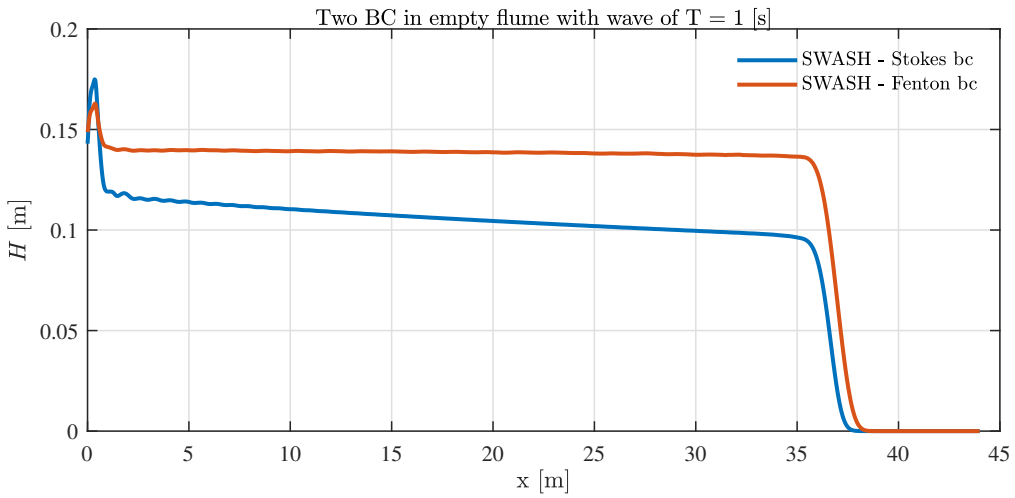

Figure 4.21: Comparison between boundary conditions(BC) generated by Stokes' theory and Fenton (1988) for T = 1 s

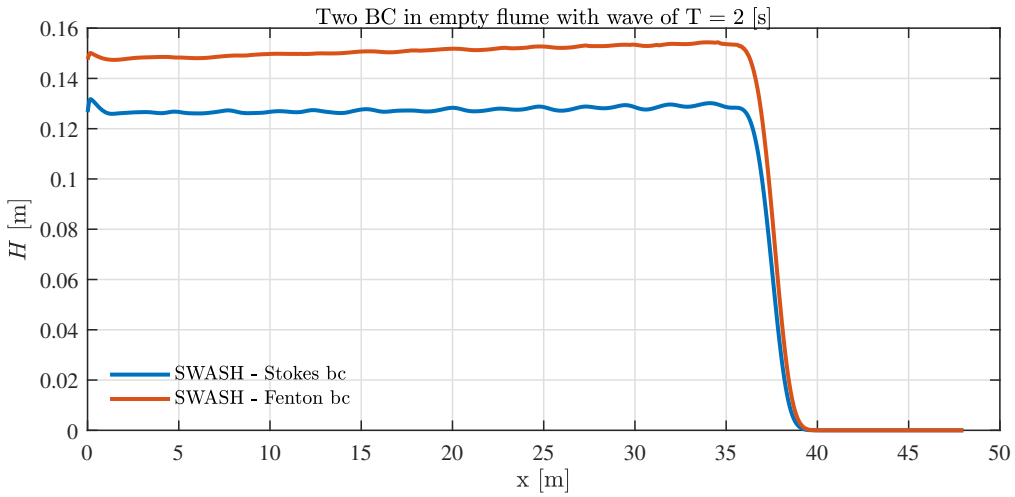

Figure 4.22: Comparison between boundary conditions(BC) generated by Stokes' theory and Fenton (1988) for T = 2 s

For T = 1 s the boundary condition (BC) by Fenton (1988) shows a better result than that by Stokes' Theory, see Figure 4.21, as the results obtained by using Stokes' theory show an artificial decrease that cannot be explained by natural propagation behaviour as the friction is not activated in SWASH. This decrease can also be seen for T = 1.25 s in Figure B.1 of Appendix B. For T = 2 s, see Figure 4.22, the wave height by Fenton (1988) is approximately 2 cm bigger than the imposed wave height of 13 cm, this is also observed for T = 1.5 and T = 1.75 in Figure B.2 and B.3 of Appendix B. Both BC's have the same pattern in the sense that the wave height increases along the flume. For T = 3 s Stokes theory does not apply and only Fenton (1988) is used to generate a timeseries, this looks well in Figure B.4 of Appendix B.

As there is not one theory that provides a good agreement with the aimed wave height of 13 cm for all the wave conditions, the different theories are compared to model wave transformation through the permeable

structures of the experiments. Figure 4.23 shows that the boundary condition from using the timeseries as calculated with Fenton's theory has slightly higher dissipation rates, as the waves are a bit steeper as can be seen in Figure 4.22. The same is observed for other configurations, as is shown in Figures B.5 and B.6 of Appendix B.

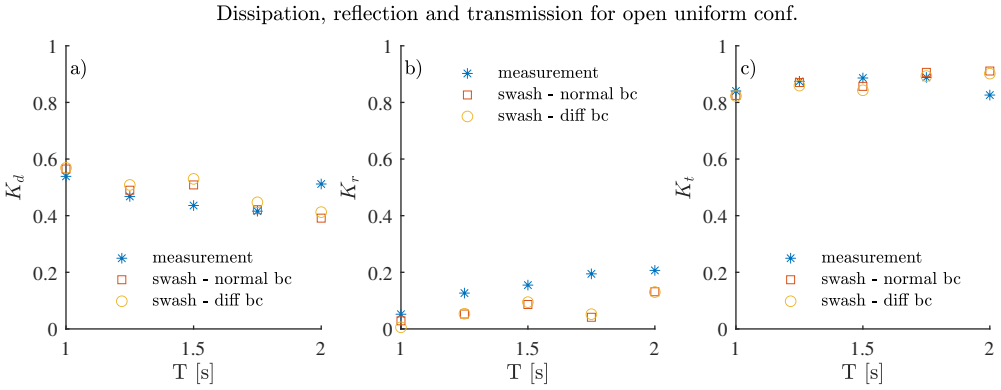

Figure 4.23: a) Dissipation, b) Reflection and c) Transmission coefficients for the case of a open uniform configuration with two BC's, where H = 0.13 [m] and T = 1 - 3 [s]. Where normal bc = Stokes and diff bc = Fenton.

4.5.3. Wave transformation through structures: use of the vegetation module

When using the vegetation module in SWASH to implement vegetation, or in this case a permeable structure, there are three important variables that can be adjusted to schematize a structure: the drag coefficient, the cylinder density and the way to describe the conservation of mass. There are other factors that also play a role, see section 3.4.3, however these are kept constant for all wave conditions and all configurations.

Influence of drag coefficient

In this section the results of the simulations of the three configurations are presented for the case of a bulk drag coefficient obtained from Gijon Mancheno et al. (2021) and this is compared with the result of using a drag coefficient value of a single cylinder. The effect of porosity is not included in the simulations as this is the subject of the next section. The structures are implemented as a block.

T [s]	1	1.25	1.5	1.75	2	3
KC	10.43	11.17	12.32	13.65	15.14	21.47
f_{KC}	0.56	0.57	0.59	0.60	0.62	0.70
$C_{d,s}$ single cylinder	2	2	2	2	2	2
$C_{d,b}$ longitudinal conf.	3.87	4.05	4.35	4.71	5.14	7.27
$C_{d,b}$ open uniform conf.	0.48	0.51	0.54	0.59	0.64	0.91
$C_{d,b}$ dense uniform conf.	1.01	1.06	1.13	1.23	1.34	1.90

Table 4.9: Full C_b values for the three configurations, where the $C_{d,s}$ is based on the experiments of Keulegan and Carpenter (1958)

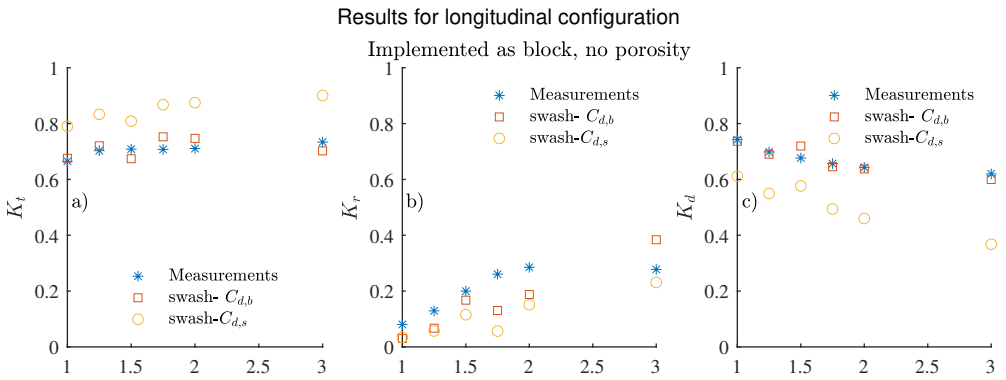

Figure 4.24: Result for the longitudinal configuration when it is implemented as a block without porosity. A comparison between the measurements and two simulated situation with the full $C_{d,b}$ and $C_{d,s}$

From Figure 4.24 the following is observed:

- the $C_{d,b}$ provides a better agreement with the measured transmission coefficient (K_t) than $C_{d,s}$ as was also observed in the experiments of Gijon Mancheno et al. (2021)
- the reflection is too low for most of wave periods except T = 3 s
- there is a slight deviation observed at T = 1.5 s

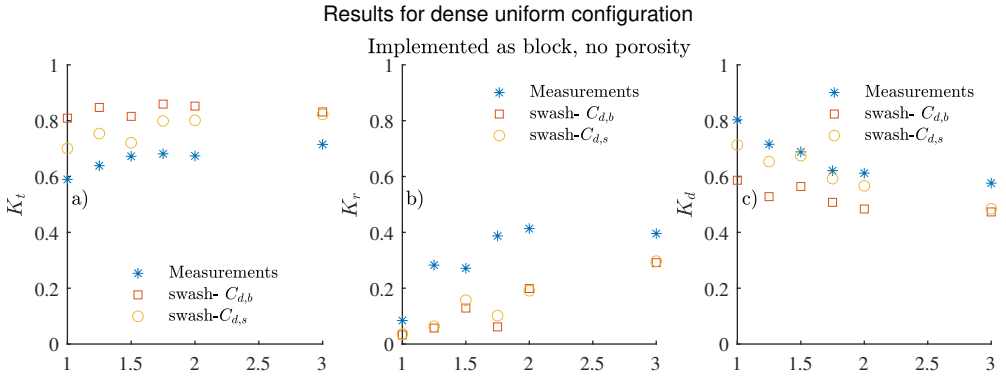

Figure 4.25: Result for the uniform dense configuration when it is implemented as a block without porosity. A comparison between the measurements and two simulated situation with the full $C_{d,b}$ and $C_{d,s}$

In Figure 4.25 the following is observed:

- the values for the $C_{d,s}$ are closer to the measurements for K_t, K_r and K_d than for $C_{d,b}$, whereas in Gijon Mancheno et al. (2021) $C_{d,b}$ has a better comparison than the $C_{d,s}$, so there is clearly something not well described yet in SWASH
- the reflection is again under predicted
- the same deviation at T = 1.5 s is observed as in Figure 4.24

It is expected that by including the porosity, the simulations will have a better comparison with measurements for the case of the dense uniform configuration.

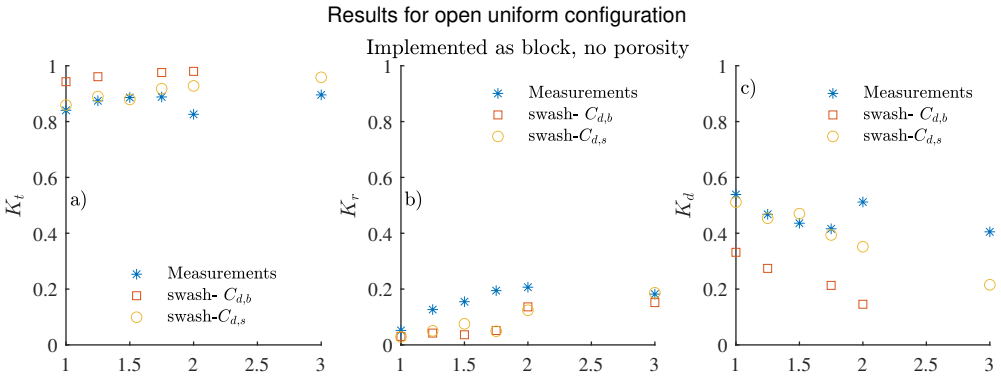

Figure 4.26: Result for the uniform open configuration when it is implemented as a block without porosity. A comparison between the measurements and two simulated situation with the full $C_{d,b}$ and $C_{d,s}$

In Figure 4.26 the following is observed:

- as observed in the experiments of Gijon Mancheno et al. (2021) the $C_{d,s}$ has a better agreement than the $C_{d,b}$. It should be noted that the measured drag coefficient should be similar to the bulk drag coefficient as the structure is very sparse but the bulk drag coefficient is in the range of 0.48 - 0.9 for the wave conditions, whereas the drag coefficient for a single cylinder is 2. So it could be that the sheltering factor as it is now reduces too much of the bulk drag coefficient.
- at T = 1.5 and 3 s, the K_t value for the $C_{d,b}$ are larger than 1 and is therefore not in the Figure. This is strange because in the other configuration there is a typically a lower value at T = 1.5 s, instead of a higher value.
- the measured K_d values are for both T = 2 and 3 s quite large

The deviation for T = 1.5 is observed in all of simulations of all the configurations but not in the measurements. Therefor it should be something that SWASH inaccurately describes but which in reality does not happen. It is not in the bulk drag coefficient as both the $C_{d,s}$ and $C_{d,b}$ have the same bump.

Implementation as block versus row by row

In the previous section the average amount of cylinders over the whole structure was used, instead of taking the cylinders per row which should come closer to the real live situation for the uniform open and longitudinal configuration as there is quite some space in between the rows. Therefore the effect of this locally changed number of cylinders is studied for the longitudinal configuration as this is the most non uniform configuration. In this section results are presented for either describing the longitudinal configuration as a block or row by row.

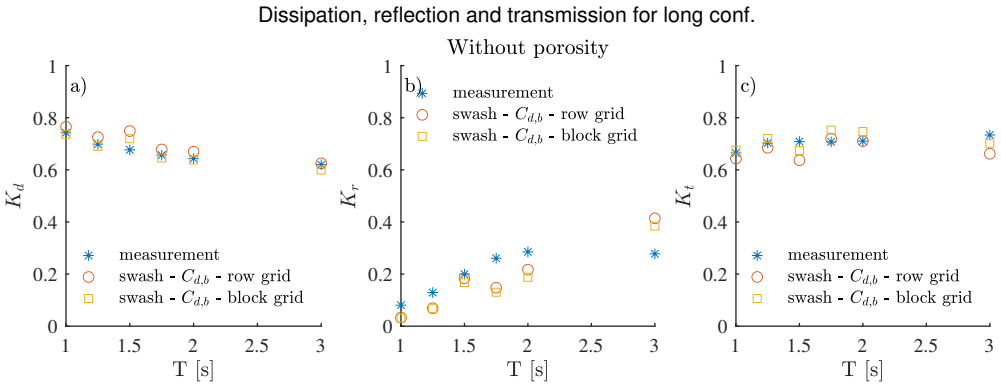

Figure 4.27: Result for the longitudinal configuration when it is implemented row by row or as a block, without porosity.

In Figure 4.27 it can be seen that there is hardly any difference between the two cases, the row by row grid has slightly higher dissipation and reflection rates and therefor lower transmission rates.

Conservation of mass: three methods

In this section the results of three different cases are compared for the longitudinal configuration and the single row configuration. The cases are the following:

1. use of a full $C_{d,b}$: $C_{d,b} = C_{d,s}(f_b f_s f_{KC})^3$
2. use of a reduced $C_{d,b}$ with only f_s and f_{KC} in combination with POROSITY activated. $C_{d,b} = C_{d,s}(f_s f_{KC})^3$
3. use of $C_{d,b}$ with f_b,f_s and f_{KC} reduced by a factor n^2, with POROSITY thus activated. $C_{d,b} = C_{d,s}(f_b f_s f_{KC})^3 n^2$

The longitudinal configuration is studied as it resembles the double fence and extended fence configurations from section 4.6. The single row configuration is studied as it resembles the single fence and mussel pole configurations from section 4.6. The longitudinal configuration is implemented as row by row as this is a non uniform configuration. The drag coefficients that are used are given in Table 4.10.

Case:	f_b	f_s	n	T :	1	1.25	1.5	1.75	2	3
full $C_{d,b}$	3	0.73	0.46	$C_{d,b}$	3.87	4.05	4.35	4.71	5.14	7.27
reduced $C_{d,b}$	1	0.73	0.46	$C_{d,b}$	0.14	0.15	0.16	0.17	0.17	0.17
$C_{d,b}$ n^2	3	0.73	0.46	$C_{d,b}$	0.82	0.86	0.92	0.99	1.09	1.54

Table 4.10: Drag coefficients for the three cases per wave period.

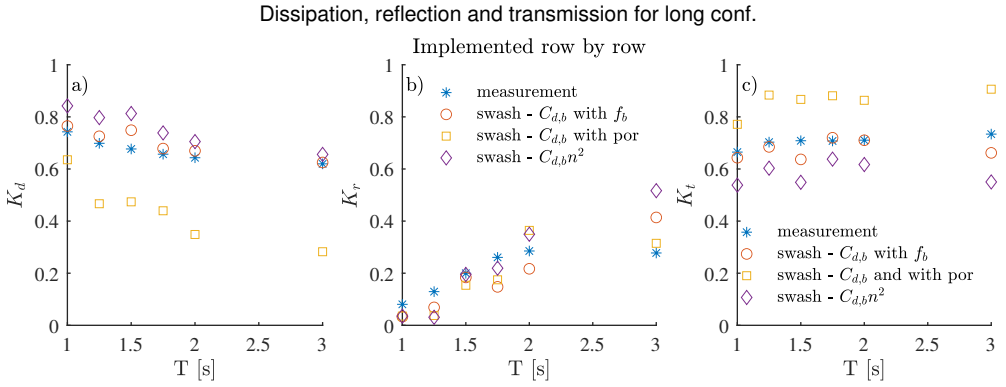

Figure 4.28: Result for the longitudinal configuration when it is implemented as a row by row . A comparison between the measurements and three simulated cases:the full $C_{d,b}$, reduced $C_{d,b}$ and $C_{d,b}n^2$

Figure 4.28 shows the simulations with the longitudinal configuration, implemented by seven rows of cylinders, the following is observed:

- the results with the full $C_{d,b}$ shows the best agreement with the measurements for all the wave periods in all of the three coefficients (K_d,K_r and K_t)
- the results of the case with a reduced $C_{d,b}$ are in terms of transmission and dissipation are far off the measured values. In terms of reflection it is in same order as the other cases.
- the results of the case with a $C_{d,b}n^2$ have slightly higher values than for $C_{d,b}$ in terms of transmission. In terms of reflection the $C_{d,b}n^2$ has higher values for T > 1.5 s than $C_{d,b}$.
- the same deviation as early mentioned at T = 1.5 is observed.

The drag coefficients that are used for the single row configuration are given in Table 3.9.

T	1	1.25	1.5	1.75	2	3
$C_{d,b}$	9.48	10.0	11.59	11.66	11.66	11.66
reduced $C_{d,b}$	0.35	0.37	0.41	0.43	0.43	0.43

Table 4.11: Drag coefficients for the single row configuration, where $C_{d,b} = C_{d,s}(f_b f_{KC})^3$ and a reduced $C_{d,b} = C_{d,s}(f_{KC})^3$. Note that the factor f_s drops out as there is no sheltering possible.

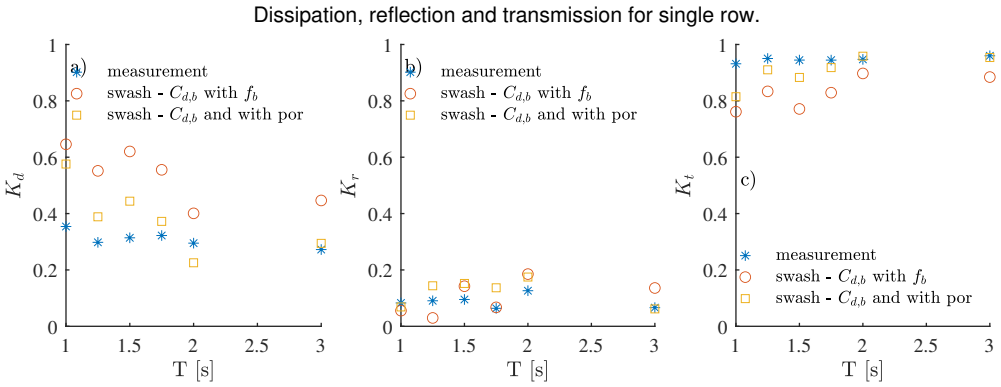

Figure 4.29: Results of the single row configuration. A comparison between the measurements and two kinds of simulations: a full $C_{d,b}$ and a reduced $C_{d,b}$ without the blockage factor but with porosity activated.

Figure 4.29 shows the result of the simulations with a single row configuration, the following is observed:

- the measured coefficients are quite constant over the different wave periods
- both mass conservation methods do not predict the dissipation well, for most of the wave periods they give higher dissipation rates than what is measured
- in terms of reflection both methods are in the same order as the measured values
- the measured transmission values have the best agreement with the case of a reduced $C_{d,b}$

Note that there is no third case like for the longitudinal configuration in Figure 4.28, as a $C_{d,b}$ times n^2 will give higher drag coefficients compared with the best fit case of a reduced $C_{d,b}$(yellow squares) and therefore higher dissipation rates, which does not improve the results.

4.6. Design

4.6.1. Introduction

This section starts with a description of the design wave conditions in Section 4.6.2. Section 4.6.3 explains what the design goal is. Section 4.6.4 shows the different designs. Section 4.6.5 explains how the wave propagation by SWASH can be improved. Section 4.6.6 explains how the maximum forces are calculated and the results of that. Sections 4.6.7,4.6.8, 4.6.9 and 4.6.10 explain the four different designs.

4.6.2. Wave conditions

The structures used for mangrove restoration in Demak have a lifetime between 2 and 5 years. Thus, either a return period of 1 or 5 years can be used for the design conditions. This has to be further specified as for the transmission the H_s is the limiting condition but for the forces the maximum waves are the limiting conditions. As the waves are depth-dependent, the water depth largely influences the conditions at the structures. However the surge height only changes by 5 cm between a return period of 1 and 5 years, whereas the wave height changes by 40 cm. The choice of tidal water level thus has the largest influence on the results, as the difference between MHW and MHWS is 7.5 cm. For the maximum forces on the structures the maximum wave height is usual approximated as $H_{max} = 1.8-2H_s$, however due the relatively long shallow foreshore the wave spectrum becomes quite narrow so this rule of thumb would be inappropriate and unrealistic. Therefore the maximum forces are evaluated in terms of the maximum water level possible, as this is suspected to have a larger effect. This means that a combination of the maximum value of the tide, MHWS, and the surge level of 5 years is used. In addition to this not the H_{m0} is be used but a $H_{0.1\%}$ as maximum wave height, more about this in Section 4.6.6. The transmission on the other hand is evaluated as a combination of a tidal water level of MHW and wave conditions with a return period of 1 year.

Return period [years]:	1	5	10	15	20
H_{m0} [m]	2.08	2.39	2.47	2.51	2.53
T_p [s]	6.9	7.5	7.7	7.7	7.7
Surge [m]	0.63	0.68	0.72	0.74	0.76

Table 4.12: Offshore design waves and surge levels for a return period from 1 to 20 years

The maximum wave, H_{max} is estimated using Battjes and Groenendijk (2000) and is chosen to be the $H_{0.1\%}$, as this seems representative for forces. First the H_{tr} has to be determined, using the following equation:

$$H_{tr} = (0.35 + 5.8tan(\alpha_{bot}))d = (0.35 + 5.8tan(0.002))1.91 = 0.69m \tag{4.2}$$

Where

- α_{bot} is the bottom slope [-], which is 1/500 as shown in Figure 3.4

Then the H_{rms} is determined using the following equation:

$$H_{rms} = (0.6725 + 0.2025\frac{H_{m0}}{d})H_{m0} = (0.6725 + 0.2025\frac{0.92}{1.91})0.92 = 0.71m \tag{4.3}$$

Using Table 2 of Battjes and Groenendijk (2000) the H_{tr}/H_{rms} gives a $\tilde{H}_{0.1\%} = 1.869$ and when multiplied with H_{rms} it gives the real $H_{0.1\%} = 1.32$ m.

The characteristics are summarized in Table 4.13.

Condition	R	H	T_p	surge	tide	d	L	N_{Ur}	KC	Re
	[years]	[m]	[s]	[m]	[m]	[m]	[m]	[-]	[-]	[-]
Daily:	0	H_{m0} =0.25	3	0	0	0.8	7.9	30.5	10.0	4.90* 10^4
Transmission										
Storm	1	H_{m0}= 0.80	6.88	0.63	0.35	0.8 + 0.35 + 0.63 = 1.78	29	111	47.3	1.01 *10^5
Stability:										
Storm :	5	H_{max} =1.32	7.47	0.68	0.425	0.8 + 0.425 + 0.68 = 1.91	32	189	81.7	1.61* 10^5
	5	H_{m0} = 0.92						132	56	1.12 10^5

Table 4.13: Nearshore design wave conditions and parameters. KC and Re are determined using the maximum orbital velocity using linear wave theory

4.6.3. Design goal

The goal of the structure is to create a sheltered place where the sediment can settle. When enough sediment has settled the mangrove seedlings are able to grow there, as there are enough propagules in the area available BioManCo (2018). The mangroves grow between MSL and MHW, which covers a range of approximately 35 cm, where the mean tidal range is 0.70 m, see section 4.2.6.

To obtain calm water where sediment can settle a certain amount of wave energy has to pass the structures to transport the sediment there. There is no specific information about which amount of energy has to be transmitted through the structures to transport enough sediment. However there is a field measurement campaign carried out in Vietnam which has comparable circumstances (Albers et al., 2013), where they reported transmission coefficients of K_t = 0.7 -0.8 for submerged and 0.5-0.6 for emerged stiff brushwood structures. The corresponding sedimentation rates are up to 17 cm in 7-8 months. Where the transmission coefficient,K_t is defined as $K_t = \frac{H_t}{H_i}$.This however does not provide a relation between a certain combination of water depth, wave height and transmission as it only gives an average.

There is a number of limitations to applying this value directly for the case of Demak. First of all, the structures were built with the fence height at MSL, whereas in Demak the current structures were initially built with the fence height above MHW but are now intertidal. The water depth at which they measured is not given but it cannot exceed than 2 - 2.4 m, so this corresponds with the used water depths in this study. However the waves in this study are slightly higher than that of Albers et al. (2013), see Table 4.13. The wave periods are unfortunately not described in (Albers et al., 2013). This also does not indicate if the sedimentation has happened during submerged or emerged situations. As higher waves transport more sediment and waves are higher with a larger water depth, it is possible that the majority of the sedimentation would take place during the submerged situation as this would also coincide with the incoming tide. This would actually relax the transmission goals of the design structures. The design structures are for most of the wave conditions be submerged. Next to this there are also be no horizontal bars in the configuration to limit the use of materials.

In terms of energy this gives the following range of transmitted energy:

- $\frac{E_t}{E_i}$ = 0.49 (say 0.50) - 0.64 or in K_t = 0.7 -0.8

As the transmission goal requires that a certain amount of energy is dissipated due to structure, the forces on the poles need to be studied to have an idea of how stable the structures are.

4.6.4. Design implementation

The current designs are made of poles that are approximately 3 m long and are driven in the ground by a team of men up to a depth of 1.5 -2 m. The maximum length of the poles is longer, up to 6 m, however longer poles are harder to handle. The pole length in this study is limited in such that the fence height coincides with the water level of MHW in combination with a surge height with a return period of 1 year. Which means that the pole length is 1.78 + 2 = 4 m. This makes them longer than the current design and also provides extra length to mitigate some of the subsidence that can be substantial in the area (Abidin et al., 2013).

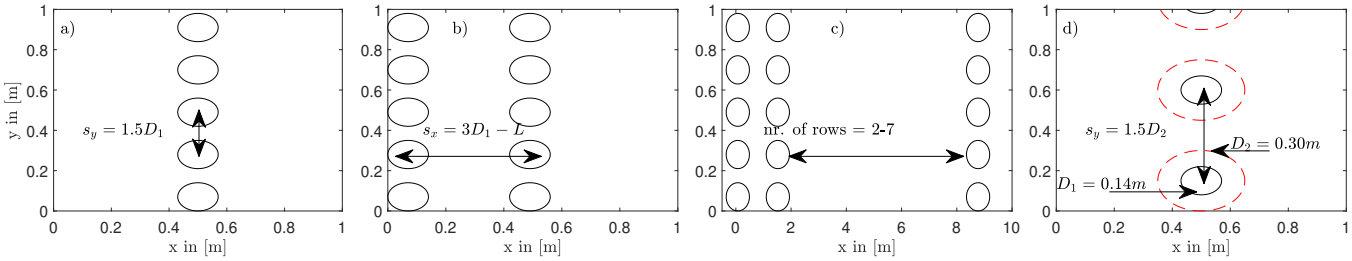

Figure 4.30: Topviews of the designs, with from left to right: Single fence, Double fence, extended fence and Mussel poles. Waves are coming from the left.

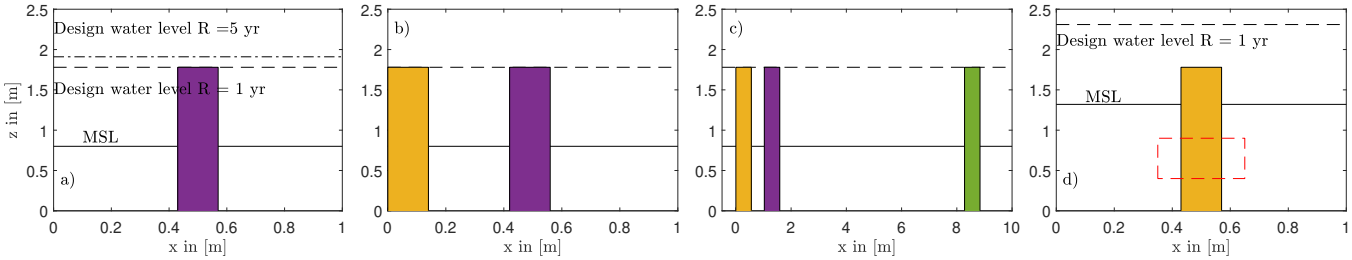

Figure 4.31: Side views of the designs, with from left to right: Single fence, Double fence, extended fence and Mussel poles. Waves are coming from the left. Note that the water depth of the mussel poles is larger as the mussels cannot grow at the depth where the other designs are placed.

4.6.5. Modelling parameters

When modelling highly non-linear waves with SWASH is it important to accurately model the higher harmonics well, especially when using a weakly reflective boundary as this might re-reflect higher harmonics. In Figure 4.32 it can be seen that at t = 34 T there are some wiggles visible in the troughs of waves. This effect is even more pronounced when we look at the $C_{d,b}$ instead of the $C_{d,s}$, as is shown in Figure 4.33. This can be improved by increasing the dx or the amount of layers, however the dx is limited to the size of the bamboo poles. So therefore the dx is kept at 5 cm while the amount of layers is set to two layers in the vertical.

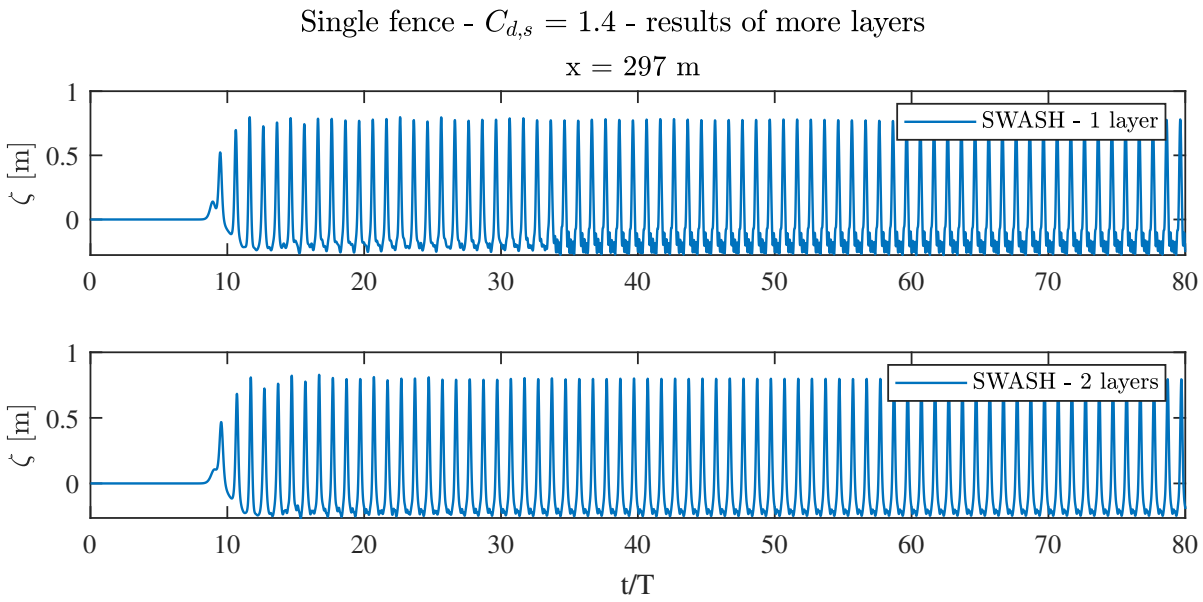

Figure 4.32: Surface elevation for 1(up) and 2(lower) equidistant layers, with the interaction with the single fence for a drag coefficient of a single cylinder

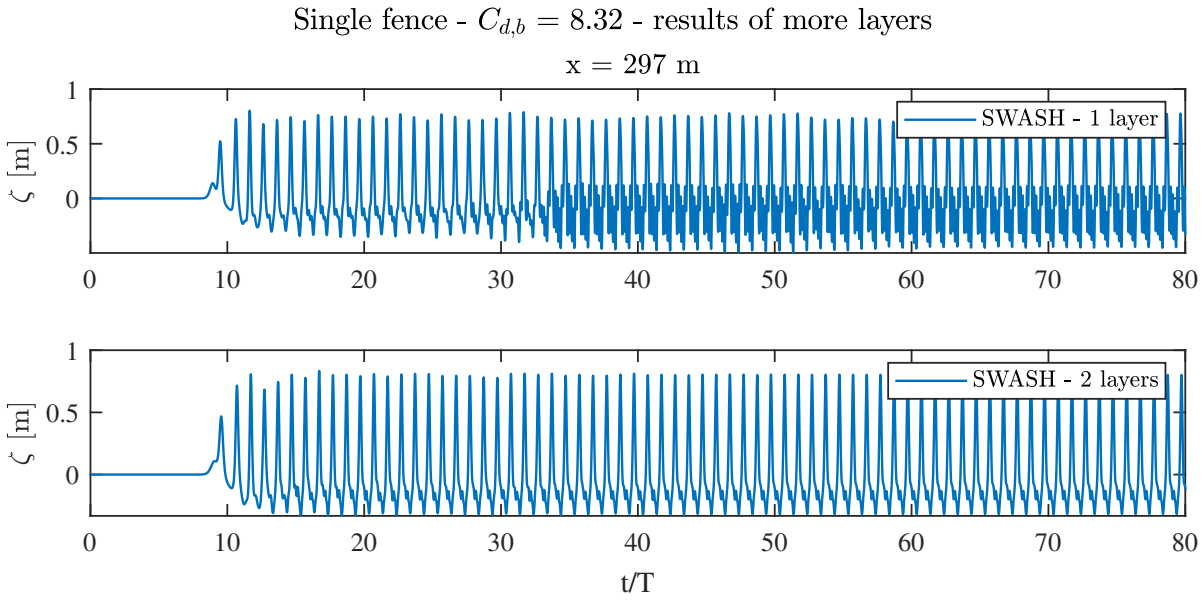

Figure 4.33: Surface elevation for 1(up) and 2(lower) equidistant layers, with interaction with a single fence for a full bulk drag coefficient. Note that this full bulk drag coefficient is not used for determining the transmission rate but only to show the effect of a higher reflection rate due to higher drag coefficient.

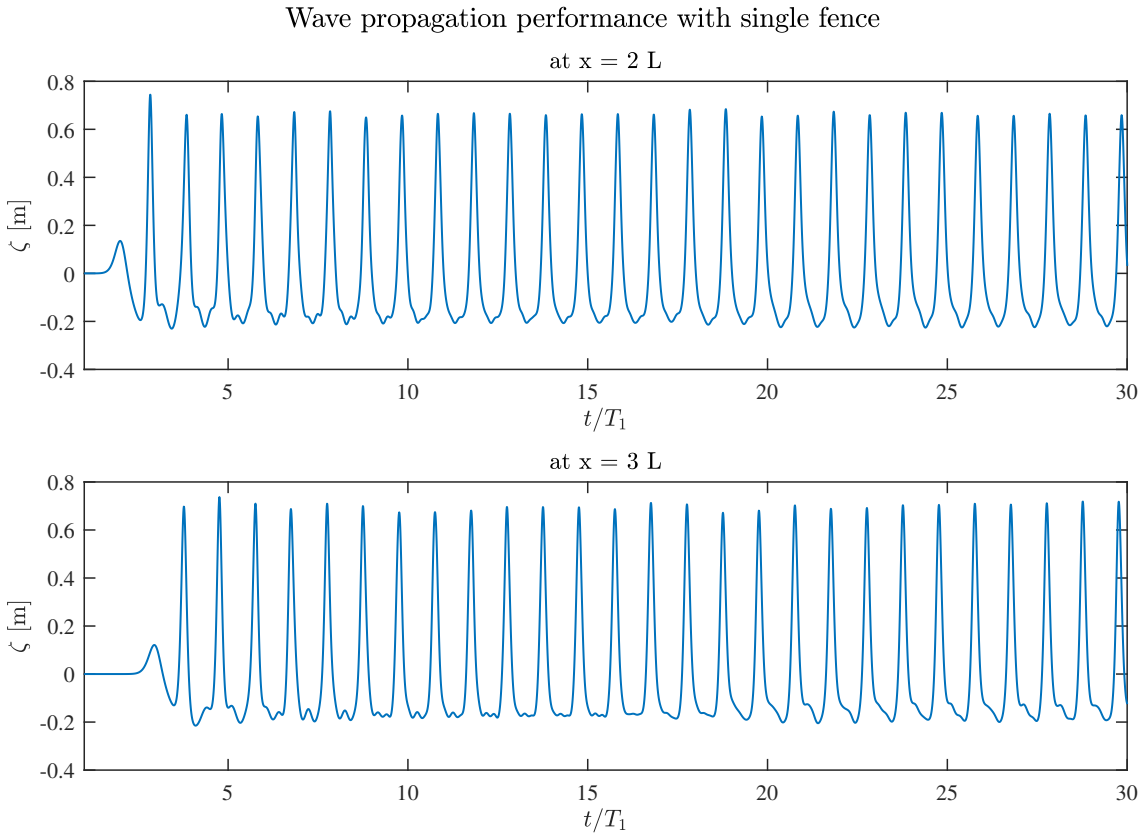

Figure 4.34: The water elevation at two locations, x= 2 L (64 m) and x = 3 L (96 m), for the wave conditions of 5 years.

As the waves that are simulated are cnoidal, the waves should not deform and the wave height should be constant along the grid up to the point where the structure is located. This is tested in the Figure 4.34 with the following output locations: x = 2 L (64 m), 3 L(96 m).

It can be seen in Figure 4.34 , that for x = 3 L between t = 8 - 16 T the wiggles slowly die out, to a point at t =16 T where they are not visible anymore. The same can be observed for x = 2 L. From t = 17 T for x = 3 L the troughs start to tilt, due to the reflected primary wave that reaches x = 3L, this occurs up to approximately t = 27 T where after the waves take on a constant form. This is a few periods later than the time that the first higher wave periods should arrive, see Table E.3, which is probably due to the friction.

4.6.6. Maximum forces

The maximum forces on the structures are calculated for two designs: the single fence and the double fence with a s_x = 3 D. To verify if it has also effect on the transmission and dissipation, it is compared with the result of using a H_{m0} as wave height instead of $H_{max} = H_{0.1\%}$. In Table 4.14, the results of two designs with a H_{max} and a H_{m0} are shown. It can be seen that the only difference is in the maximum forces and therefore the dissipation and transmission of H_{m0} can also be related to a $H_{0.1\%}$. It was expected that due to a steeper wave and higher N_{ursell}, using H_{max} would cause more dissipation (Phan et al., 2019) however this cannot be observed.

Design	Single Fence		Double fence (s_x = 3 D	
H =	H_{m0}	H_{max}	H_{m0}	H_{max}
E_t/E_i [-]	0.93	0.926	0.76	0.75
E_r/E_i [-]	0.01	0.0125	0.027	0.031
E_d/E_i [-]	0.06	0.06	0.21	0.21
F_d [N]	50.6	72.5	454	750

Table 4.14: Comparison for single fence and double fence designs, where wave height in SWASH is varied between H_{max} and the H_{m0}, the wave period is kept constant.

4.6.7. Single fence

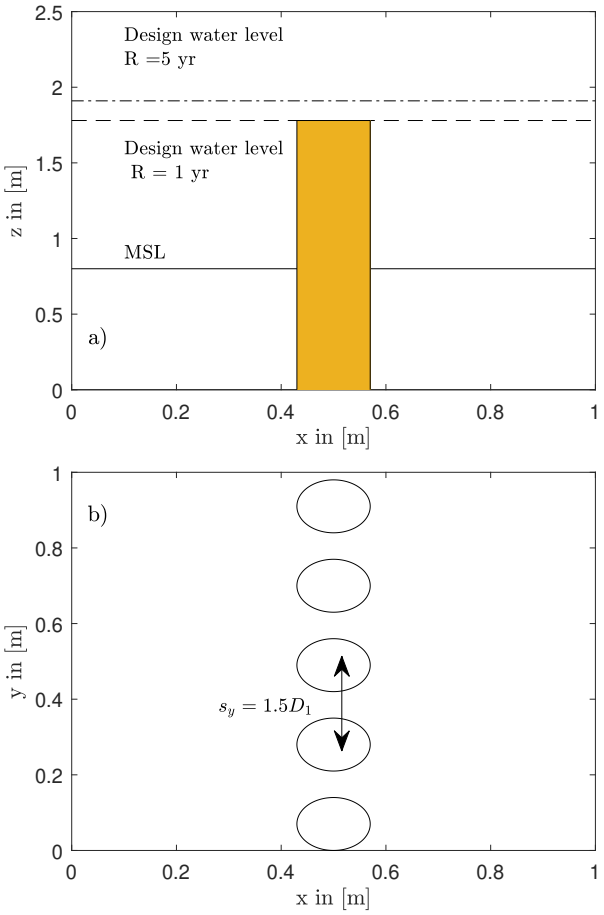

Figure 4.35: Design of the single fence, with in a) the sideview and b) the topview. The poles have a lateral distance of s_y = 1.5 D = 1.5 14 = 21 cm

The first case is a simple fence, one row of cylinders, with a center to center distance of $s_y = 1.5 * D$, like is shown in Figure 4.35. The fence height is at the design water level (R=1 yr).

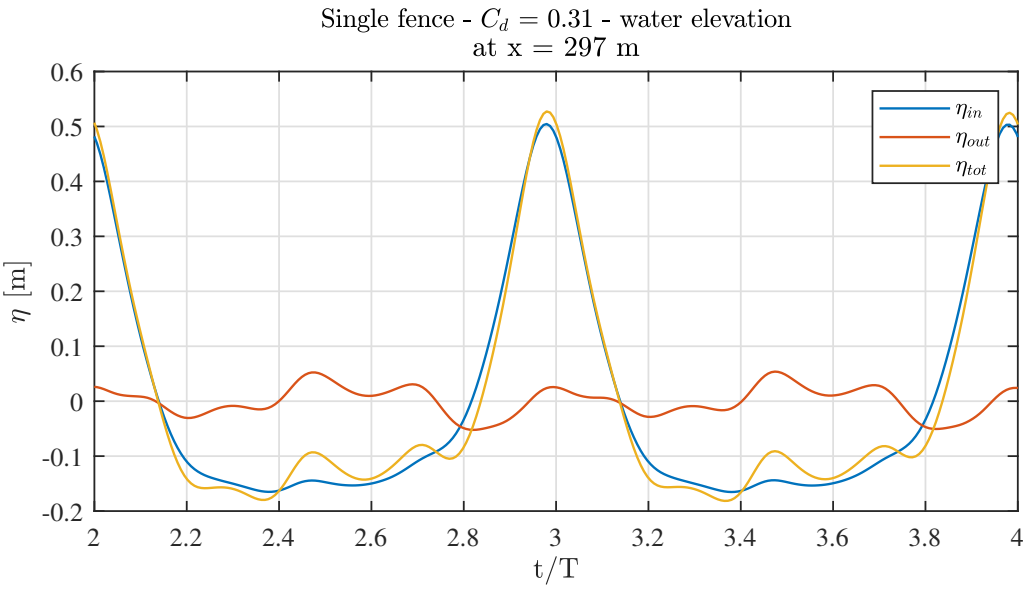

Figure 4.36: The total, incoming and outgoing surface elevation for a bulk drag coefficient of $C_{d,b}$ = 0.31 after 50 waves.

Results: Single fence

It can be seen in Figure 4.36 that the incoming surface elevation is nearly equal to the total surface elevation, in front of the structure. This indicates that there is hardly any reflection.

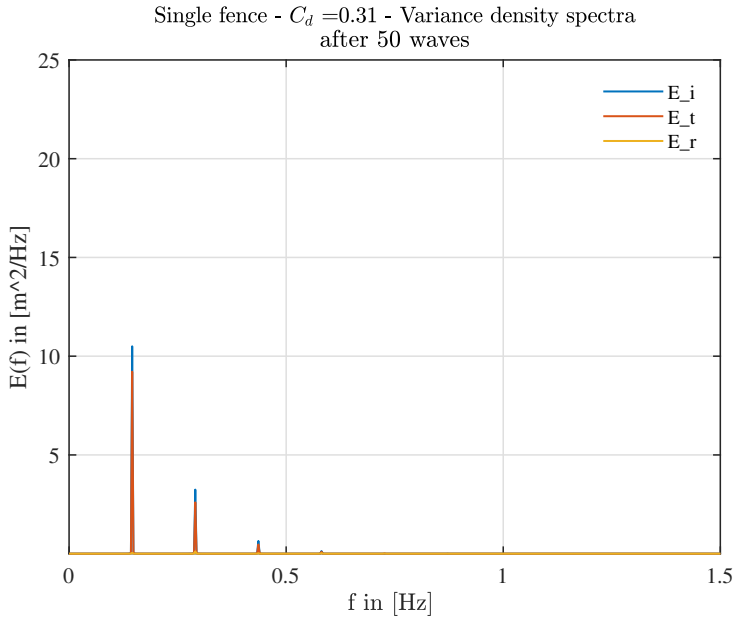

Figure 4.37: The variance density spectra of the incident, transmitted and reflected surface elavation of Figure 4.36

In Figure 4.37 it can be seen that the primary wave frequency and the first two higher harmonics contain the visible wave energy. Along the frequencies, it can be observed that ratio of incident over transmitted wave energy is approximately the same and reflection is not observed. Thus this leads to the following transmission, dissipation and reflection rates, see Table 4.15.

	E_t/E_I	E_r/E_i	E_d/E_i	F_d (N)
R = 0 years	0.82	0.028	0.15	3.7
R = 1 year	0.85	0.014	0.11	30
R = 5 years	0.93	0.01	0.06	72.6

Table 4.15: The transmission, reflection, dissipation rates and maximum forces for the daily wave conditions (R=0) and storm conditions(R = 1 and 5 yr)

4.6.8. Double fence

For the double fence design the lateral distance is $s_y = 1.5 * D$, the longitudinal distance s_x between the successive rows is varied between s_x = 3 D - L, to reduce sheltering and increase wave dissipation. s_x = 3 D is the longitudinal distance of the longitudinal configuration of the experiments of Jansen (2019), this gave for the longest wave period (T=3 s) a K_t = 0.8 or in terms of energy E_t/E_i = 0.64, however for the designs a lower transmission rate is desired and instead of 7 rows 2 rows are used. Therefore the distance s_x is increased to design an efficient structure with the least amount of rows as that saves material and thus costs less money. The distance s_x is also varied in order of the wave length as from s_x = L/4 or larger a resonance pattern is expected.

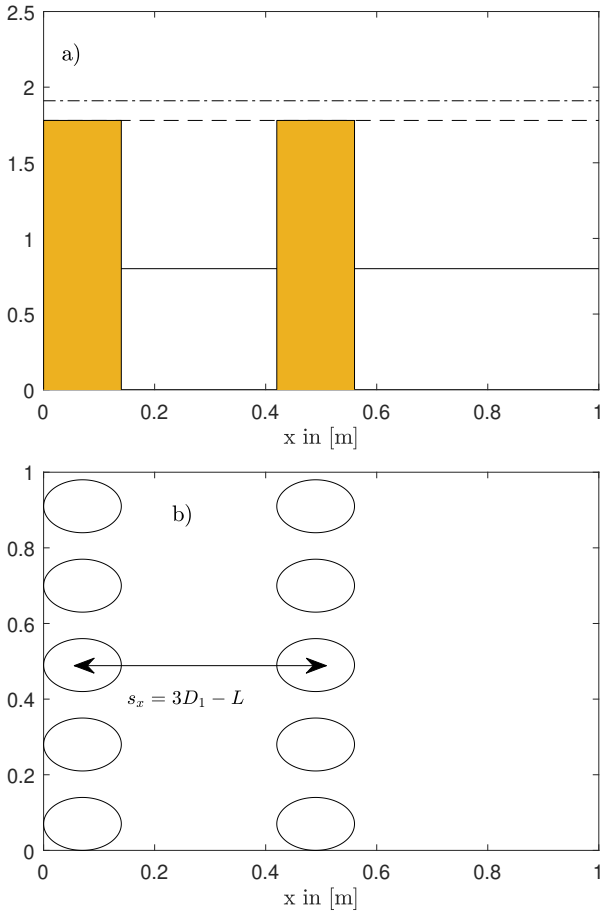

Figure 4.38: The double fence design, with in a) the sideview and b) the topview. The lateral distance s_y = 1.5 D = 21 cm. The distance s_x is varied between 3 D and $L_{R=1}$ to find an optimal distance in terms of wave transmission

The drag coefficients that are used are presented in Table E.4

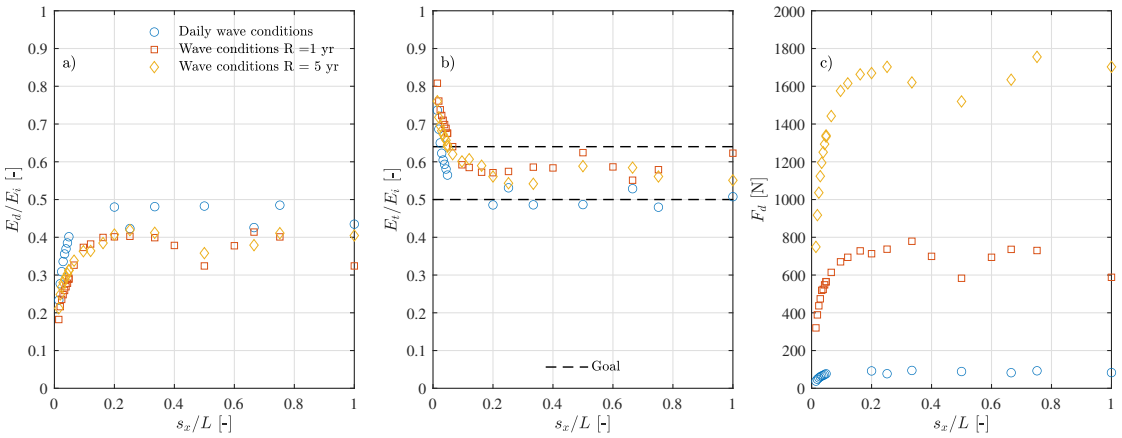

Figure 4.39: The results of varying the center to center distance s_x as function of the diameter. With from left to right: a) dissipation rates, b) transmission rate and c) maximum forces for the three wave conditions.

The reflection rates are in the order of 5 % and can be seen in Figure E.3, in Appendix . The dissipation, transmission and maximum drag forces are shown in Figure 4.39. From Figure 4.39 the following is observed:

- the dissipation rates (E_d/E_i) of the daily wave condition are for all distances s_x larger and stabilize at 50%, this due to that the drag coefficient for the daily wave conditions is higher and that the crest of the wave hits the pole whereas for the storm conditions it travels over the poles.
- the maximum forces for the storm wave conditions vary around F_d = 1600 N. For the return period of 1 there are clearly 2 lower forces, around $s_x = L_{rp1}/2$ and $s_x = L_{rp1}$

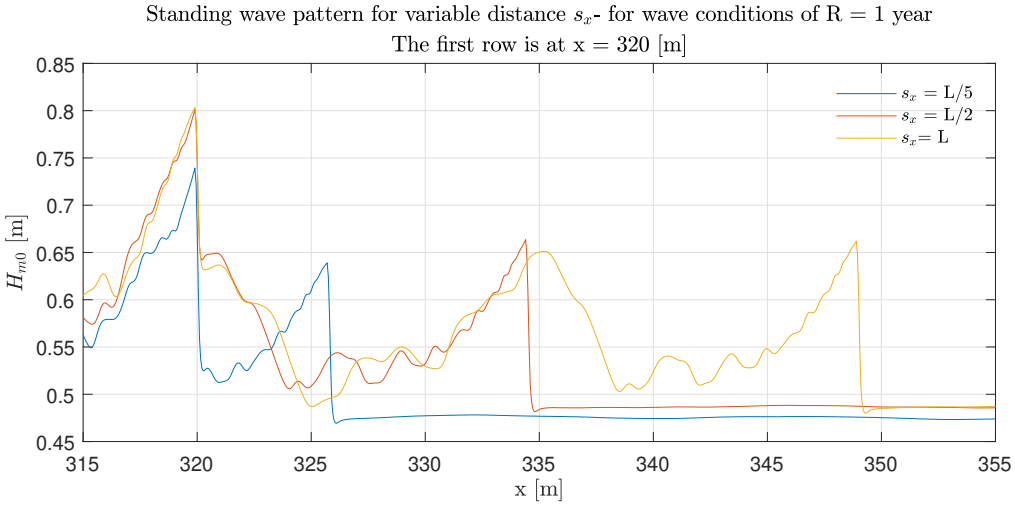

Figure 4.40: H_{m0} for three simulations where the second row is placed at s_x = L/5, L/2 or L, over the distance x. The second rows can be clearly observed by the sharp peaks an for s_x = L/2 and L there is also a clear peak in between.

In Figure 4.39 it could be seen that for the cases of s_x = L/2 and L, the transmission rates increased and the forces are significantly smaller than for other distances s_x. In Figure 4.40 three distances are shown s_x = L/5, L/2 and L,where s_x=L/5 is added for the perspective. The reflection at the first row can be observed clearly for the three cases, for s_x = L/2 and L the wave height is 5 cm higher than for s_x = L/5. The reflection at the second row can also be clearly observed and for the s_x = L/2 and L there is a peak visible at x = 321 m and 335 m, respectively. This is an anti-node, which should occur at a distance of L/2 seawards (to the left) from the second row according to theory. The nodes which should occur at x = L/4 or 3/4 L are less clear due to the presence of the higher harmonics. Due to the anti-node at the first row, the horizontal velocities become also smaller which in term give less dissipation and therefor higher transmission rates. This can be observed in Figure 4.41, where the velocities and forces at x = 320 m are shown. Aside from the maximum forces that occur in the shorewards direction, it can be observed that for s_x = L/5 during the trough of the wave the dragforce reaches up to a negative value of F_d = 200 N approximately. This is approximately 25% of the maximum drag force, indicating that it would be unwise to neglect this in a further stability analysis as a repeated pull and push movement on the poles may give settlement issues.

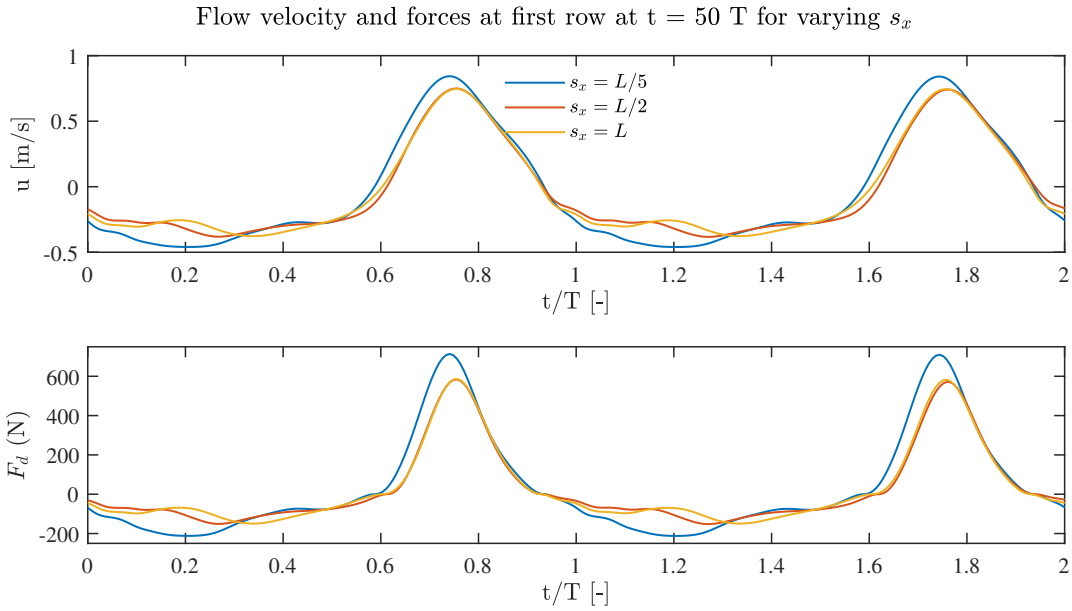

Figure 4.41: Horizontal flow velocity (above) and forces(lower) for three simulations: S_x = L/5, L/2 and L. With on the x axis two wave periods

4.6.9. Extended fence

The extended fence configuration is used to study effect of more rows after in the previous section an effective distance is found of s_x = L/5. Extra rows could be more dissipative although this effect decreases with the amount of rows.

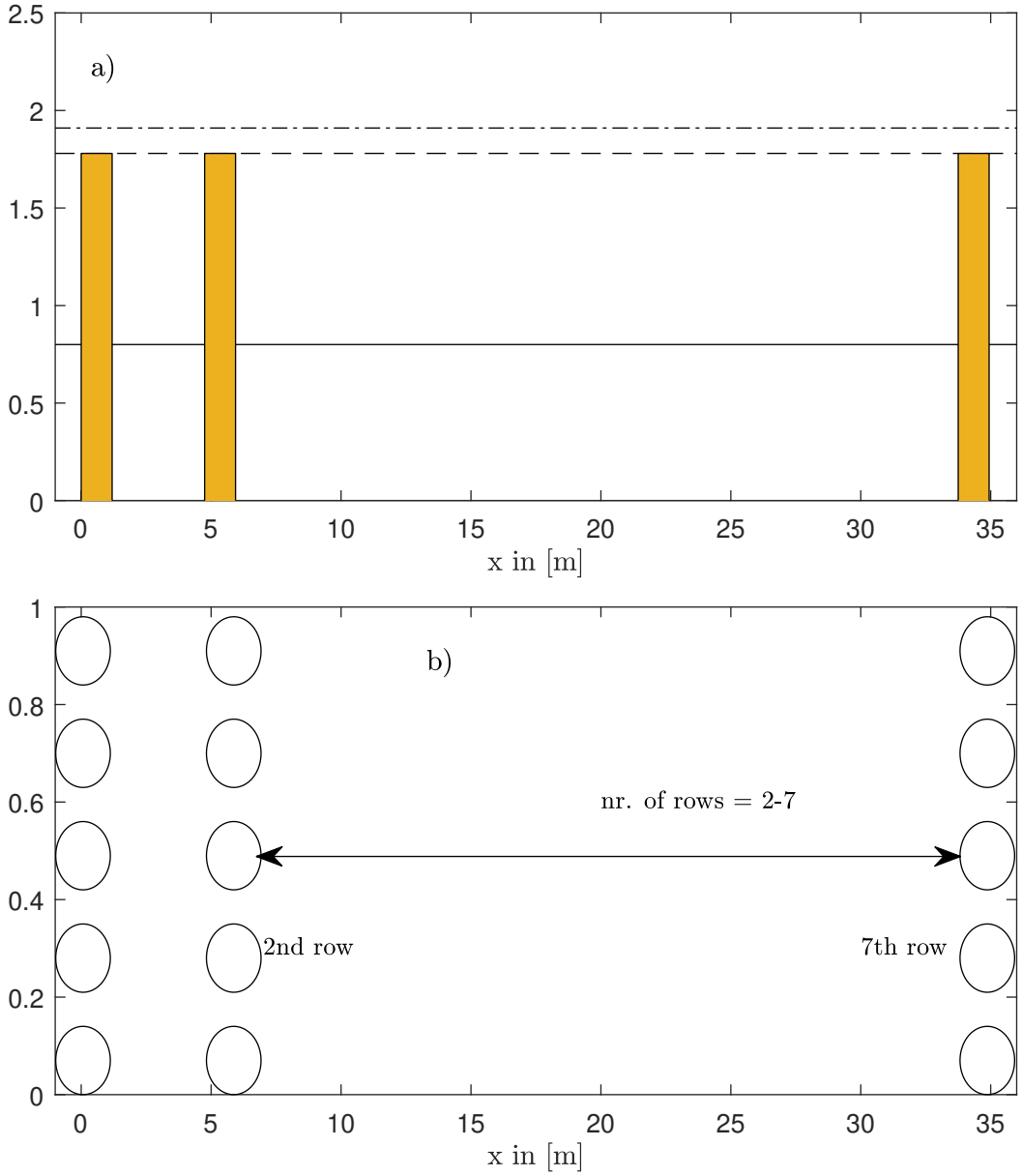

Figure 4.42: The design of the extended fence, where the distance between the rows is kept constant and the number of rows increases from 2 - 7.

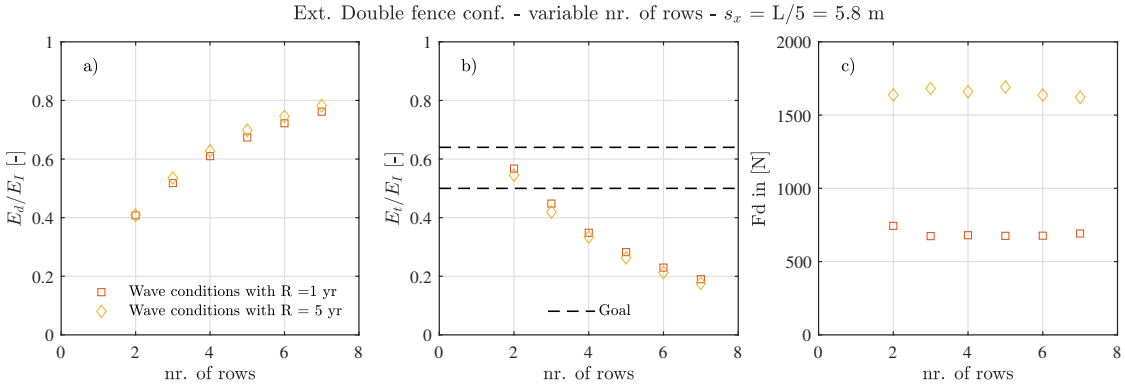

Figure 4.43: a) Dissipation, b) transmission and c) forces against a increasing number of rows. The distance between the rows is kept constant at s_x = L/5

From Figure 4.43 the following is observed:

- the transmission goal of E_t/E_i = 50 - 64 % is achieved after 3 rows
- the dissipation rate for R = 5 years is initially the same as R = 1 year but after 3 rows it becomes slightly higher.
- by increasing the amount of rows, the added extra dissipation decreases. For instance if we look at the effect of 2 to 3 rows, the E_t/E_i changes by 0.13. However if we look at the effect of 5 to 6 rows, the E_t/E_i changes by 0.07.
- the F_d stays approximately constant around 1600 and 600 N, for R = 5 and 1 year respectively.

The higher dissipation rates are probably due to that the waves of R= 5 yr interact with the full length of the pole during a wave period as the water level is higher. Whereas for R= 1 yr during the troughs of the waves a part of the pole becomes emerged, as the top of the fence is at the still water depth of the wave condition of R= 1 yr. This is shown in Figure 4.44

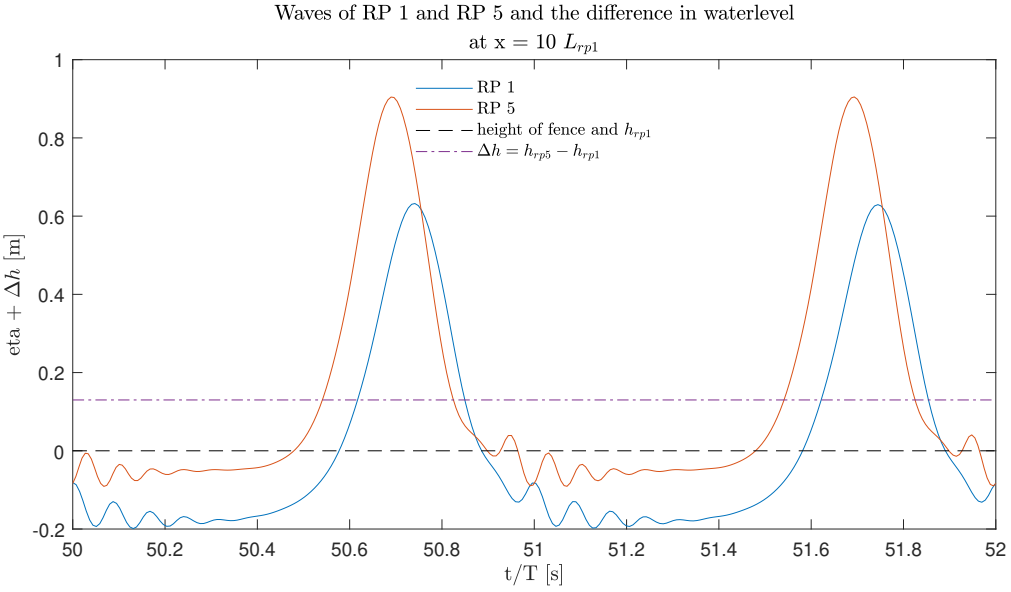

Figure 4.44: Surface elevations after 50 waves for a return period of 1 and 5 years and the relative distance between the surface elevation and the top of the poles.

4.6.10. Mussel poles

To study the effect of mussels on wave dissipation the size and added roughness are studied separately. The size is studied in three steps: D = 0.14, 0.22 and 0.30 m. Where D= 0.14 is the case without mussels, 0.22 is halfway grown and 0.30 is with fully grown mussels. Where the the center to center distance is kept constant. Due to the varying diameter, the blockage of the flow varies also over the year.

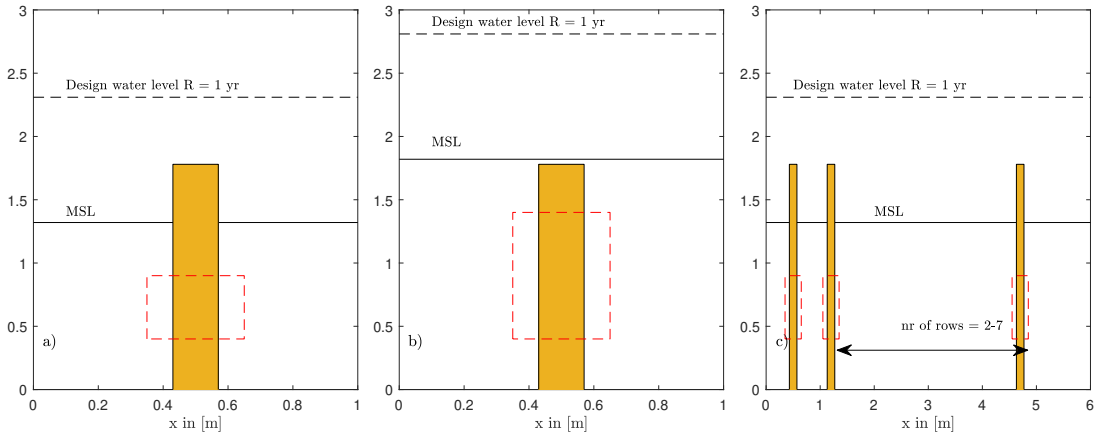

Figure 4.45: Design of mussel poles for a) a depth of 2.31 m, b) a depth of 2.81 m and c) multiple rows at a depth of 2.31.

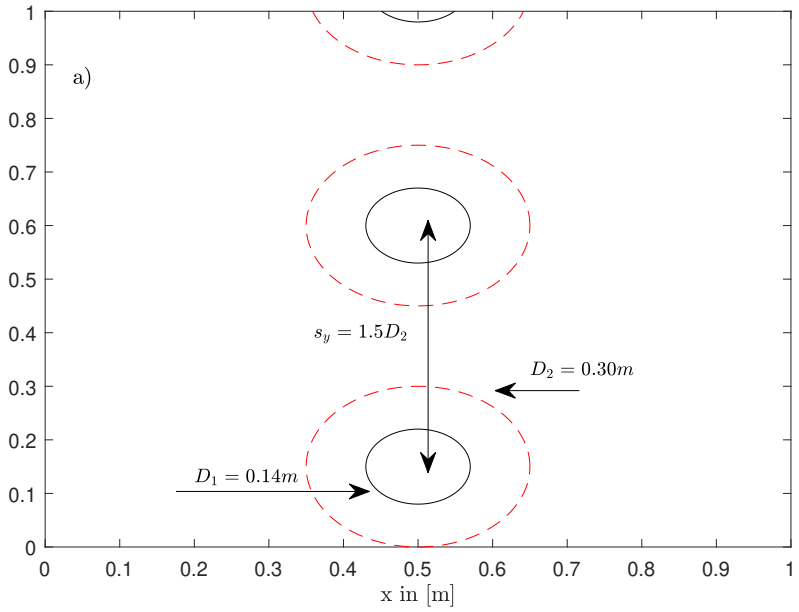

Figure 4.46: Topview of the musses poles, with in red the mussels and in black the bamboo poles.

The added roughness is studied by simply multiplying the computed bulk drag coefficient by an increasing factor: f_m. Where f_m is varied between 1.1 , 1.2, 1.3, 1.4, 1.5 and a maximum of 2.

As the mussels cannot stay dry for long, they are placed in such that they always stay under MLWS, -0.42 m MSL, see section 2.2.7. The mussels should also be 30 - 50cm from the bottom to avoid predation of the young mussels (Herman, 2021). Therefore multiple locations (depths) are studied as this also influences how much length of the poles is available for mussels. On the location of the other designs, around a depth of 80 cm, the mussels are not able to grow there. Thus two other depths are selected, a depth where 0.5 m of the pole is available : $d = 0.5 + 0.425 + 0.4 = 1.32m$ MSL and where 1 m of the pole is available $d = 1 + 0.425 + 0.4 = 1.82m$ MSL.

As result of this different depth the wave conditions also change slightly with respect to Table 4.13, therefore the new wave conditions are presented in Table 4.16.

As the mussels do not grow over the whole depth, the added area is evaluated in comparing the case of a fully covered pole with a partly covered pole, the last one is of course the realistic one. Where a fully covered means that the poles is covered from top to bottom with mussels.

Condition	Return period	H	T	surge	tide	d	L	N_{Ur}	KC (D = 0.14-0.3)
	[years]	[m]	[s]	[m]	[m]	[m]	[m]	[-]	[-]
Transmission									
depth 2	1	1.08	6.88	0.63	0.35	1.32 + 0.35 + 0.63 = 2.31	31.7	88	56.55-26.4
depth 3	1	1.31	6.88	0.63	0.35	1.82 + 0.35 + 0.63 = 2.81	34.7	71.1	62.6-29.24

Table 4.16: Wave conditions for the locations of the mussels. Note that KC is not one value anymore but a range as the diameter of the poles vary over time, with these wave conditions the structures are still drag dominated.

The drag coefficients that are used are the following:

1. Bottom: (0 - 0.4 m with respect to the bottom) the $C_{d,s}$ in combination with the porosity activated is used.
2. Mussel: (0.4 to MLWS), the drag coefficient of $C_{d,b} = C_{d,s}(f_{KC})^3$ is used in combination with porosity activated as this had the best agreement in Figure 4.29 for the case of single row.
3. Top: (MLWS - surface elevation), the $C_{d,s}$ as the same reason as the bottom part.

The rows are placed 1.40 m apart to provide enough space for nutrients and oxygen to reach the mussels.

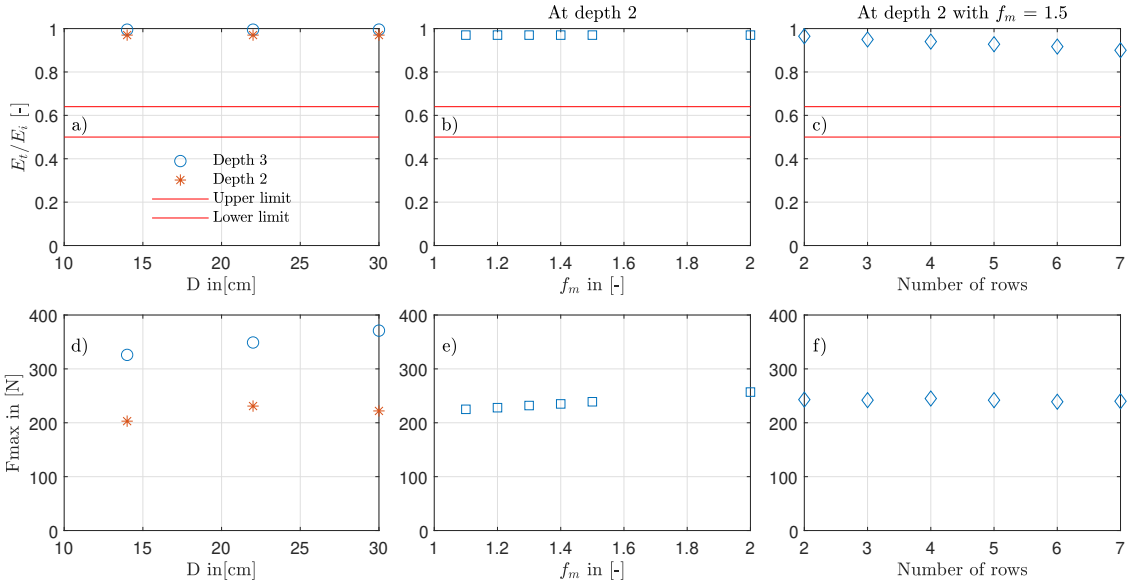

Figure 4.47: Transmission rates and maximum forces for three cases: a) and d) different depths, b) and e) a function of f_m factor, c) and f) as function of number of rows. f_m increases the drag coefficient as $C_d = f_m C_d$

In Figure 4.47, only the transmission rates and the forces are shown as the reflection and dissipation is negligible, see Figure E.2 in Appendix E. The following is observed:

- the transmission rates for Depth 3 are slightly larger due to the larger depth
- the drag forces there is a slight increase visible with increasing diameter, as expected.
- the forces stay constant over the increasing number of rows
- the forces do increase slightly with increasing f_m

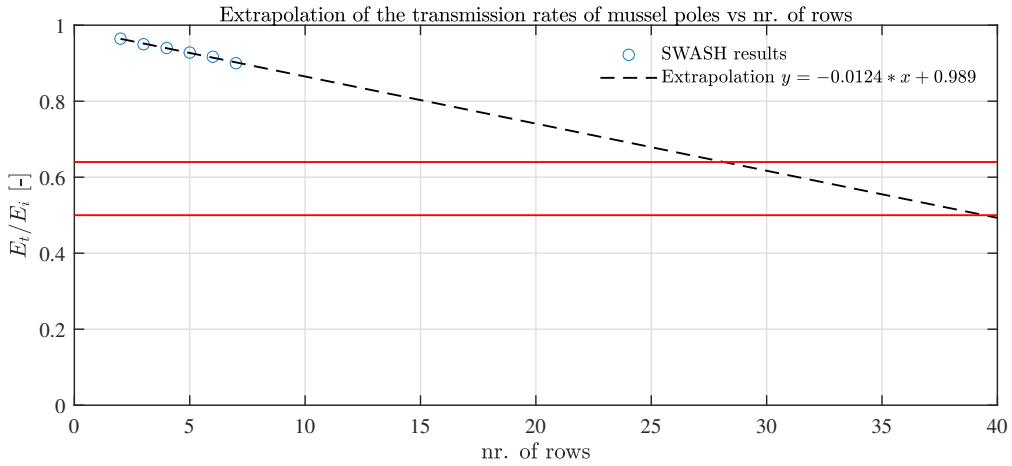

Figure 4.48: Extrapolation of the number of rows to find the required number of rows to achieve the transmission goal.

In Figure 4.47 it was shown that the transmission rates decrease slowly with an increasing amount of consecutive rows. Therefore the relation between transmission rate and number of rows is extrapolated to study how much rows of mussels poles are needed to fall in the range of 64-50 % transmission. In Figure 4.48 it can be seen approximately 28 to 38 rows are needed. With a center to center distance of 1.4 m, this requires an distance of approximately 40 to 50 m to place all these poles. This is not impossible as it the slope in Demak is very mild, providing enough space for these structures.

4.6.11. Sensitivity analysis

Most of the designs are submerged as the combination of high water levels due to surge and tides and a limited pole length. As the waves at the location are depth-dependent the sensitivity of the different water depths is studied, starting with a water level at MSL (so d = 80 cm). Then the water level is increased in consecutive steps up to the design water level:

- MSL, so d= 80 cm
- MSL + MHW, so d= 80 +35 = 115 cm
- MSL + Surge(R= 1 yr) - MHW, so d= 80 + 63 -35= 108 cm
- MSL + Surge(R = 1 yr), so d=80 +63 = 143 cm
- MSL + Surge(R = 1 yr), so d= 80 + 63 +35 =178 cm

This is studied for two distances s_x of the double fence design, s_x = L/5 and L/2 respectively. The wave height is scaled with the depth as, $H = 0.55d$, where 0.55 is the breaking parameter as in Section 3.3.

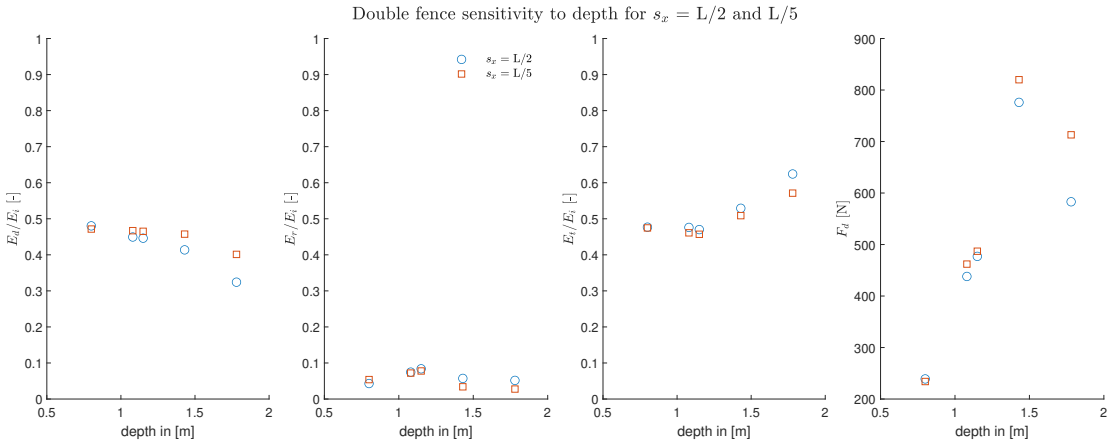

Figure 4.49: Sensitivity of the double fence design to different water depth for the distances of s_x = L/5 and L/2.

It can be seen in Figure 4.49 that the transmission decreases with the depth and that thus the design water level, d = 1.78 m, is an upper limit. However for the forces, the maximum forces occur not during the design water level but one step lower at d = 1.43, in this situation the poles are emerged and experience also the wave impact from the crest and not only the flow velocity in case of the design water level as the poles are submerged.

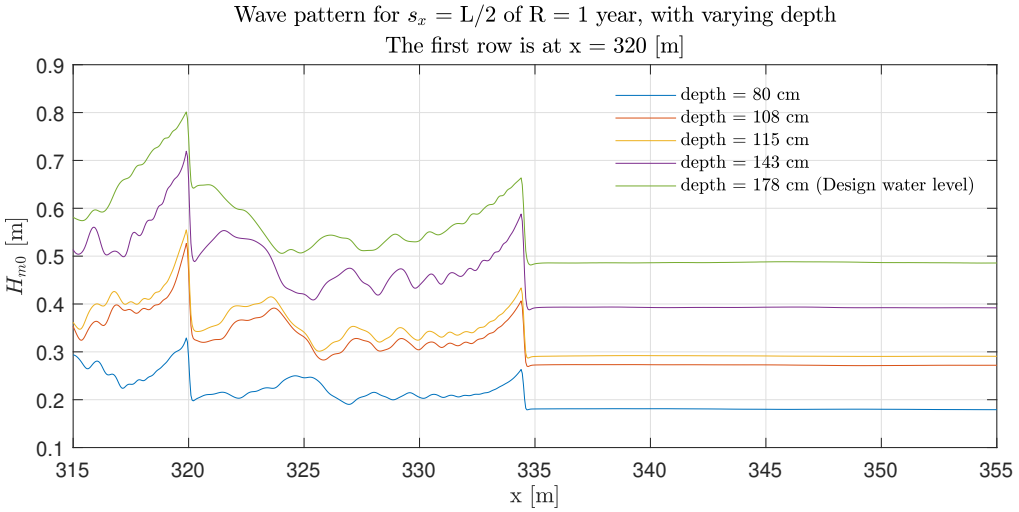

Figure 4.50: H_{m0} over the computational grid, with the wave height of 5 different depth ranging from d = 0.8 m to 1.78 m. It can be observed that the pronounced peak at d = 1.78 slowly disappears with the decreasing depth

It can be seen in Figure 4.50 that the pronounced anti-node at the first row disappears with decreasing depth.

5

Discussion

This chapter evaluates the limitations and results. The first section discusses the methods and limitations, followed by a discussion of the results in Section 5.2.

5.1. Limitations

5.1.1. Limitations of extrapolation methods

The design conditions for the structures are derived by extrapolating the WaveWatch III data. In Figure 4.6 it can be observed that most of the data has a return period of 1 year or lower, leaving only a small amount of data left in the range of 1 to 10 years. With the range of interest of this thesis between 1 -5 years this probably will not lead to substantially different results if for instance a longer timeseries is used, as having such low return periods (1 and 5 years) will place them relatively close to most of the data points (combination of wave height and return period), so changes will be minimal.

However the WaveWatch III data consists out of model results and not field measurements, which does not include the local generated waves so this could hypothetical lead to missing relevant data. However WaveWatch 3 does contain the monsoon waves as can be observed in Figure 4.2, which present the storm conditions and dominate the yearly wave climate and therefore could be used to determine the design conditions for the structure. What could make a difference is the fact that the data from WaveWatch III is only validated for one storm event, which has a good agreement but may not be representative for 12 years of data from WaveWatch III.

5.1.2. Water levels

The design water levels used in this study are the sum of the still water depth with respect to MSL, tidal levels and surge levels. The tidal levels are based on average levels during a measuring period of 3 months, where usually a tidal analysis is done for a year or longer. However as the spring-neap cycle has a period of 28 days, the important tidal levels can be determined within this 3 months.

The surge levels proved to be most influential on the total water level as the surge levels are in the order of the tidal range and as the waves are depth-dependent they also facilitate high waves. The surge levels that are used in this thesis are from Willemsen et al. (2019), where they transformed surge levels from a global model in the order of $1/2\,^{\circ}$ to a coastal model in the order of $1/20\,^{\circ}$. The global hydrodynamic model used by Willemsen et al. (2019) is obtained from Muis et al. (2016), where they reported that the average RMSE for the surge levels was below 0.2 m for 95 % of the stations with respect to measurements. As the error in surge levels in Willemsen et al. (2019) is unfortunately not mentioned, it is assumed that the error is the same. An error of 0.2 m could be substantial in surge levels of 0.6 -0.65 m.

5.1.3. Wave reflection processing techniques

The methods of Goda and Suzuki (1976) and Mansard and Funke (1980) derive wave reflection coefficients from water surface measurements. When these methods were compared against a signal from which the reflection was known beforehand, they proved to be accurate for the wave conditions of the experiments of Jansen (2019). However when we applied these two methods to SWASH results of the design wave conditions, they provided unrealistic values of reflection. This was attributed to the design waves implemented in SWASH being significantly more non-linear than the waves studied in the experiments of Jansen (2019). Thus was resorted to the method of Hughes (1993), which was extended by Dekkers (2018) to measure bores and cnoidal waves. The maximum N_{Ursell} was approximately 25, as he used this method for labaratory scale measurements, whereas the N_{Ursell} of the design waves were significantly larger around 119 -135. The requirements

of Dekkers (2018) still hold in SWASH, despite the higher N_{Ursell}.

5.1.4. Limitations using SWAN

SWAN was used to propagate the offshore design waves from deep water to the model boundary of SWASH. The storm event of the 1st of December 2017 is used to calibrate the SWAN model, as it was measured offshore and in the nearshore. It can be seen Figure 4.2 that there was another substantial but smaller storm event observed in the timeframe in which was measured, however the nearshore measurements did not prove to be accurately on this date. The measurement instrument had an extreme setoff after the 6th of December. Therefore the calibration of the storm wave conditions may not be so accurate. As can be seen in Section **??** the most influential factor proved to be the α, indicating that the wave breaking may not be well described in SWAN. However the results of SWAN proved to have a good fit with measurements. In relation to this, the dissipation by mud in SWAN is neglected as the focus of this thesis is on the interaction with the structures. However the study of Borsje (2019) suggests that including wave dissipation by mud may give a more complete view of the situation at Demak, however he also indicates that using this module in SWAN requires thorough validation of the behaviour of mud under influence of waves and as this is at the moment not available, excluding the wave dissipation by mud seems like a sound approach.

For the modelling in SWAN it is assumed that the waves travel in one direction, whereas in Figure 4.4 it could be seen that the waves do group around the shore normal but do certainly not come from one direction. This in term makes the waves refract and could lead to lower wave heights as the waves that come under an angle travel a longer distance. However it might occur that due to the crossing wave rays, the wave height will increase. If we take a look at the bathymetry, see Figure 3.4, the slope is fairly constant. However as this is only one transect the real bathymetry may be different and compared with the depth contours in Figure 3.5, the assumption of an alongshore uniform bathymetry does not describe the bathymetry completely as the lines are not fully parallel and it can be seen that at some locations the lines are relatively close to each other, which indicates abrupt changes in the bed level.

5.1.5. Design

The diameter, D, is assumed to be one value whereas in reality this will cover a certain range. This will mainly influence the blockage of the flow as small changes in s_y change blockage factor f_b considerable. In direction of the flow this effect is negligible as the distances s_x are significantly larger than the diameter.

The wave length in this study is constant in time, as is the case for regular waves, when in reality during a storm this will cover a range. Suppose the wave length is longer during a storm, then this combination of wave length and spacing would place it more to the left in Figure 4.39 resulting in higher transmission rates. However a longer wave length can only be result of or a higher wave period, or a larger water depth or both, but all imply a higher return period making it more unlikely to occur. Suppose the wave length is shorter during a storm, placing it more to the right in Figure 4.39 which give does not change transmission significantly after a certain point. This could be a result of a smaller water depth which in Figure 4.49 is shown will lead to lower transmission rates, which is favourable. It could also be due to a lower wave period which will result in a steeper or similar wave which will give reduced or equal transmission rates, but not larger.

5.1.6. Limitations to drag parameterization

The model of Gijon Mancheno et al. (2021) that is used to determine the $C_{b,d}$ has a factor f_{KC}, that describes a relation for between the drag coefficient and the KC number. However the C_D for a single cylinder is also dependent on a KC number, so this might be counted twice. The sheltering factor f_s reduces the effective bulk drag coefficient as it describes the effect of a wake on the downstream cylinders. This is determined by the turbulent intensity of the wake and is given by the factor c_s, which was fitted in the experiments of Jansen (2019). This value was however used outside of the calibration range for the design waves. As the waves are higher and longer then in the experiments, the Re changed from 6.7 - 11.9 10^3 to 1-1.6 10^5. It is expected that the turbulent intensity will be higher and therefore the wake will be longer, resulting in a lower bulk drag coefficient.

When comparing the forces acting on the single fence design the maximum force acting on the pole is 72 N whereas the largest forces of the double fence design is in the order of 1600 N. This difference cannot only be described by the effect of the downstream row on upstream flow velocity. Using a different method of describing mass conservation can lead to this large range in force even when the transmission rates are quite similar.

A large difference between the experiments of Jansen (2019) and the proposed designs is that the designs are submerged for the wave conditions of a return period of 1 and 5 years, whereas in the experiments all structures were emerged.

5.2. Evaluation of the results

The proposed designs, designed to achieve a transmission rate of 50 -64 %, are subject to uncertainties in the hydraulic loading, model schematization, building material and not the least the required transmission rate.

Drag coefficient: not one uniform method for different structural configurations

In Section 4.5.3 three approaches to describe mass conservation in the configurations from Jansen (2019) are evaluated in SWASH. It is found that there are multiple approaches needed to the describe the different configurations whereas it would be favourable to have one approach that compares well with all the configurations. This makes it also difficult to compare for instance the design of two rows of poles (double fence) with that of one row of poles (single fence).

Wave conditions and depth dependency

The focus of this thesis is on the high waves, as these limit the designs. As the designs are in shallow water the larger waves occur during the higher water levels. Therefore it was assumed that high waves and high water levels occur simultaneously. This would require that surge and MHW or MHWS occur at the same time, however these are not constant in time so this could also result in lower water levels and therefore lower wave heights. The sensitivity of this is shown in Section 4.6.11, where it can be observed that the transmission actually decreased instead of increased as one would expect for less steep waves, assuming that the peak wave period stays constant. However due to a lower water level the crest of the wave does not travel over the poles as is the case for the design waves but does travel through the bamboo resulting in thus extra dissipation and less transmission.

One could also argue that not the T_p but the $T_{m-1,0}$ should be the relevant wave period when describing the nearshore waves. In deep water conditions this the $T_{m-1,0}$ is usually 10 % smaller than the T_p, but nearshore this can be different. Assuming the $T_{m-1,0}$ is smaller nearshore, this will lead to a shorter and steeper wave which will probably dissipate more than using the T_p but also could give a shorter peak force with higher bed shear stresses.

Design goal

The transmission rate that the designs should achieve is based on a field measurement campaign in Vietnam of Albers et al. (2013). This is not the same conditions as in Demak, but has comparable circumstances. The structures that were used in that study are more like the current brushwood dams in Demak, whereas the designs in this study are more open as they only consist of vertical poles. Therefore the transmission rate and sedimentation rate may not be comparable.

This study focuses on the reduction in wave energy which should lead to sedimentation behind the structure and thus leads to an area which could be intertidal, which is necessary for mangrove seedlings to be able to settle. These mangrove seedlings require also a different design goal than the relative transmission rate that is used in this thesis, they require a limited bed shear stress and a window of opportunity to settle and survive the first few days (Balke et al., 2011; Rees, 2019).

Aside from the transmission rate of the structures the measurement campaign spanned a period of 7 - 8 months, so the long term effect of this structure are not well understood yet and likewise for the current design. As it is not likely that the bed level behind the structures rises from -0.8 m MSL to intertidal in one year, the transmission rate will also vary over the lifetime of the structures. It is therefor unsure if the initial sedimentation after one year, assuming that it traps sediment as the structures in Vietnam, is followed by more sedimentation in the successive years. One could argue that due to a smaller water depth and the effect of the structure the wave energy is even more reduced, leading to more sedimentation. However the sediment is mainly brought in by the incoming tide and could deflect by the structures, resulting in sediment not reaching the hinterlaying basin. In line with this, Borsje (2018) observed that at the existing permeable dams at places where the waves were more dominant the wave induced Stokes flow was stronger than the rising tide. This could prevent sediment from going through the dams. At the current dams this is solved by making gaps in the dams, in such that the sediment laden flow can enter the basin and this also facilitates the drainage of the basin. The proposed designs are more open and may not need these gaps but it is yet unsure how these designs interact with tide induced currents.

A significant way of sediment transport that is identified for the coast of Demak (Winterwerp et al., 2020; Borsje, 2019) is the streaming of mud. Structures could potentially disrupt this, the proposed designs are more porous than the current dams which is favourable but it is unknown how the proposed designs affect the streaming of mud.

6

Conclusions and recommendations

6.1. Conclusion(s)

This thesis aims to design structures formed by vertical poles, without brushwood filling, combined with mussel aquaculture and therefore investigates how the placement of rows of bamboo poles affects wave dissipation, and what could be the potential effect of integrating mussel growth on the structure performance. It evaluates the wave transmission by means of the results of Albers et al. (2013).

6.1.1. Sub - questions

The following sub-questions are used to support main research question:

What are the hydraulic design conditions for the structures in Demak, Indonesia?

First the boundary conditions are identified (sub-question 1). The structures are designed to remain stable during storm conditions while damping waves according to a target. These criteria depend on the wave height, wave period, water depth and the bathymetry. The design waves and water levels are a function of the return period. As the the lifetime of the structures is between 2 - 5 years, a return period of 1 year is chosen for the wave damping criteria and for the stability criterion a return period of 5 years is used. Next to the design wave conditions, the daily wave conditions are modelled to obtain an impression of the performance of the structures under calm conditions taking place most of the year. Note that these are not determined offshore but are based on nearshore measurements. For the waves data is used from WaveWatch III and this is then filtered and extrapolated to determine the offshore design waves. The offshore wave heights vary between H_{m0} = 2.08 and 2.53 m for a return period of 1 and 20 years, respectively. This is then transformed from an offshore point to a location in the nearshore with the numerical wave model SWAN, to determine the nearshore design wave conditions. For the water levels a minimum of the 80 cm MSL is considered, as this the water depth of the current structures, to which the tidal and surge levels are added. This results in the following design conditions, see Table 4.13.

How many rows are needed to have a transmission rate lower than 50 % of the incoming wave energy?

The effect of multiple fences can lead to less transmission (sub-question 2), but how much depends on the distance between the successive rows. This can be seen in Figures 4.39, where the distance is varied in order of a few diameters to a full wave length for the case of a structure with two rows. It can be seen that the transmission rate stabilizes around 55 %, when the distance between two rows is in the order of s_x = L/5 or larger. Therefore at least three rows are needed to cause a transmission of 50 % or lower,for the wave conditions of 1 and 5 years.

How does the reflection between rows change the transmission rates behind the structure?

In general the transmission rates stay quite constant when the distance between the rows is varied, except for two cases. Slightly larger transmission rates were observed for the distances s_x = L/2 and L, for both cases 4-6% larger transmission rates were observed. This can happen when the second row is placed at distance of s_x = L/2 and L, as this results in an anti-node at the first row. Due to the anti-node the horizontal velocities are lower and therefore the dissipative effect of the poles on the flow velocity is lower. This caused the higher transmission rates.

How does the structural stability change for different designs?

From all the designs, the double fence designs, with the largest s_x have the highest forces acting on the poles. As the rows are relatively far away, the effect of sheltering becomes negligible and leads to relatively high bulk drag coefficients which is one of the reasons that the forces are so high compared to the other designs.

How much do the mussels contribute to the wave damping and how does this effect the wave transmission of the mussels?

They do not contribute much as they are only partially present on the pole, which leads to that the higher and lower parts of the poles have a very high porosity and do not dissipate a lot of energy. Even when the bulk drag coefficient is increased, it does not result in a lower transmission rate. The only measure that did effect the wave transmission was increasing the number of rows, although the effect is minimal. Another factor is that the poles are located in deeper water, as the mussels cannot grow at a depth of 80 cm MSL, and the poles have a limited length so they are submerged by 1 m.

6.1.2. Final conclusion

The research question is the following:

Which structure designs consisting of bamboo poles can cause transmission rates of 50 to 64 % of the incident wave energy?

In total four different designs are studied, see Figure 4.31: single fence, double fence, extended fence and mussel poles. As result a structural design consisting of 2 rows of bamboo poles, with a lateral spacing of s_y = 1.5 D and a spacing in flow direction s_x = L/5 results in a transmission rate of 55 %. It could be observed in Section 4.6.11 that this actually an upper limit as for lower water depths the transmission decreased. Next to this, if one wants to include mussels at least 28 to 38 rows of mussels are required to be in the transmission range of 50 -64 %.

6.2. Recommendations

This section explains which subjects are recommended for further studying.

6.2.1. Modelling with SWASH

It is recommended to develop in SWASH the possibility to include different structures at the same time.Structures formed with different geometries (and drag coefficients) could provide more design alternatives. Being able to change the properties across the profile would be useful to model structures where for instance some rows have mussels, whereas others not.

Now it is possible to change the characteristics over the vertical, so for instance a different diameter at a height of 2 m, but this vertical layer is then constant over the whole x and y grid. In the current version, in the horizontal plane one could change the number of N_stems in the grid, to describe for instance a high density of plants in a certain area. This can be done by varying the changing the default value of 1 to for instance 2 or 0.5. However this does not change the drag coefficient or diameter. So to implement different structures at the same time in SWASH, it is needed to be able indicate for structure 1: from point A (x,y) to point B (x,y) the characteristics of the structure are D_1 = .. m, $N_{stems,1}$ =... and $C_{d,1}$ etc. and then for a second structure from point C(x,y) to point D (x,y) the characteristics of the second structure are D_2 = ... m, $N_{stems,2}$ =... and $C_{d,2}$ etc.

The sheltering factor f_s depends on the center to center distance between two poles in flow direction and the turbulent intensity. In the current study the turbulent viscosity is not activated but it could be interesting for modelling purposes if the shelter factor could be reproduced with the use of a certain turbulence model in SWASH.

6.2.2. Designing permeable structures

The blockage of the flow is a dominant factor in reducing wave transmission and therefore in enhancing sedimentation behind the structures, so if one wants to optimize this even further it should be considered that blocking the flow means to a certain extent also blocking the sediment transport. The proposed designs are in this sense more porous than the current designs with a brushwood filling, however one should consider that there is a limit to which extend you can block the flow and this is still not well understood.

In order to fully optimize the designs a cost-benefit analysis should be undertaken, especially for the mussel poles as they do not reduce the waves significantly as can be seen in Figure 4.48 whereas they can provide a income to the local community. This can give a better estimation in how much mussel poles are needed and if additional bamboo fences are required for the wave transmission. It is recommended to do a study to the stability of the poles with taking into account the soil properties. This can give a better indication of which designs can be build in Demak, Indonesia and how it may possibly influence the designs. In Figure 4.41 it could be seen that the forces in seawards direction are not negligible and this continuously pull and push movement on the pole could lead to settlement issues.

To obtain a better understanding of the presence of the mussels on the flow, laboratory experiments should be carried out as in this study the drag coefficient was based on the experiments of Jansen (2019) and these did not include a variable diameter over the height and used smooth poles.

6.2.3. Data collection

There are several studies which have studied the wave damping of permeable structures to obtain a relation what kind of structural element provides which amount of dissipation. However the goal of these structures is usual to protect the hinterlying coast and for Demak, to provide a certain amount of sedimentation. It was assumed in this study that a certain transmission target would provide enough sedimentation, but there is not a clear relation of which amount of transmission is needed to obtain a certain amount of sediment after a season. So the bottom profile behind the structures should be monitored when building the structures of the MuMaCo project in combination with wave measurements before and after the structures.

Aside from this, the drag coefficient along with conservation of mass proved to be most influential factors in describing the interaction between waves and structures. As some of the structures have been recently built (November 2021), it would be valuable to validate the work in this study by measurements. This could be done in a similar way like in Dao et al. (2021), where measured water elevations from a physical flume are used as input for SWASH. The method of Gijon Mancheno et al. (2021) can then be used to determine the drag coefficient and by having measurements available the empirical coefficient c_s can be refitted on this real scale structures and wave conditions.

Bibliography

Willemsen, P., van der Lelij, A. C., & Wesenbeeck, B. V. (2019). Risk Assessment North Coast Java, 25. https://www.ecoshape.org/app/uploads/sites/2/2020/02/1220476-002-ZKS-0007_v0.1-Risk-Assessment-North-Coast-Java-final.pdf

Van Domburg, T., Smits, I. B. P., & Van Bijsterveldt, C. E. J. (2018). Identifying Windows of Opportunity for Mangrove Establishment on a Mud Coast. http://repository.tudelft.nl/.

Codiga, D. (2011). The model , for raw input at a set of arbitrarily spaced times , is, 1–60. papers2://publication/uuid/C87EF698-E7AE-4579-816B-4E71F22E56B4

Jansen, W. J. (2019). Wave dissipation in a permeable structure. http://resolver.tudelft.nl/uuid:acce330d-968a-46a7-853f-73137b06002a

Gijon Mancheno, A., Jansen, W., Uijttewaal, W., Reniers, A., van Rooijen, A., Suzuki, T., Etminand, V., & Winterwerp, J. (2021). Wave transmission and drag coefficients through dense cylinder arrays: implications for designing structures for mangrove restoration. *Ecological Engineering*, (March, 2021). https://doi.org/10.1016/j.tifs.2019.11.018

Dalrymple, B. R. a., Asce, M, & Kirby, J. T. (1984). Wave Diffraction Due To Areas. *110*(1), 67–79.

Barbier, E. B., Hacker, S. D., Kennedy, C., Koch, E. W., Stier, A. C., & Silliman, B. R. (2011). The value of estuarine and coastal ecosystem services. *Ecological Monographs*, *81*(2), 169–193.

Temmerman, S., Meire, P., Bouma, T. J., Herman, P. M., Ysebaert, T., & De Vriend, H. J. (2013). Ecosystem-based coastal defence in the face of global change. *Nature*, *504*(7478), 79–83. https://doi.org/10.1038/nature12859

Quartel, S., Kroon, A., Augustinus, P. G., Van Santen, P., & Tri, N. H. (2007). Wave attenuation in coastal mangroves in the Red River Delta, Vietnam. *Journal of Asian Earth Sciences*, *29*(4), 576–584. https://doi.org/10.1016/j.jseaes.2006.05.008

Tonneijck, F., Winterwerp, H., Weesenbeeck, B. v., Bosma, R., Debrot, D., Noor, Y. R., & Wilms, T. (2015). Building with Nature Indonesia Securing Eroding Delta Coastlines, 1–65.

Hamilton, S. E., & Casey, D. (2016). Creation of a high spatio-temporal resolution global database of continuous mangrove forest cover for the 21st century (CGMFC-21). *Global Ecology and Biogeography*, *25*(6), 729–738. https://doi.org/10.1111/geb.12449

Abidin, H. Z., Andreas, H., Gumilar, I., Sidiq, T. P., & Fukuda, Y. (2013). Land subsidence in coastal city of Semarang (Indonesia): Characteristics, impacts and causes. *Geomatics, Natural Hazards and Risk*, *4*(3), 226–240. https://doi.org/10.1080/19475705.2012.692336

Winterwerp, J. C., Erftemeijer, P. L., Suryadiputra, N., Van Eijk, P., & Zhang, L. (2013). Defining eco-morphodynamic requirements for rehabilitating eroding mangrove-mud coasts. *Wetlands*, *33*(3), 515–526. https://doi.org/10.1007/s13157-013-0409-x

Primavera, J. H., & Esteban, J. M. (2008). A review of mangrove rehabilitation in the Philippines: Successes, failures and future prospects. *Wetlands Ecology and Management*, *16*(5), 345–358. https://doi.org/10.1007/s11273-008-9101-y

Kodikara, K. A. S., Mukherjee, N., Jayatissa, L. P., Dahdouh-Guebas, F., & Koedam, N. (2017). Have mangrove restoration projects worked? An in-depth study in Sri Lanka. *Restoration Ecology*, *25*(5), 705–716. https://doi.org/10.1111/rec.12492

Lewis, R. R. (2005). Ecological engineering for successful management and restoration of mangrove forests. *Ecological Engineering*, *24*(4 SPEC. ISS.), 403–418. https://doi.org/10.1016/j.ecoleng.2004.10.003

Winterwerp, J. C., Albers, T., Anthony, E. J., Friess, D. A., Mancheño, A. G., Moseley, K., Muhari, A., Naipal, S., Noordermeer, J., Oost, A., Saengsupavanich, C., Tas, S. A., Tonneijck, F. H., Wilms, T., Van Bijsterveldt, C., Van Eijk, P., Van Lavieren, E., & Van Wesenbeeck, B. K. (2020). Managing erosion of mangrove-mud coasts with permeable dams – lessons learned. *Ecological Engineering*, *158*(June), 106078. https://doi.org/10.1016/j.ecoleng.2020.106078

Rejeki, S., Debrot, A. O., van den Brink, A. M., Ariyati, R. W., & Lakshmi Widowati, L. (2021). Increased production of green mussels (Perna viridis) using longline culture and an economic comparison with stake culture on the north coast of Java, Indonesia. *Aquaculture Research*, *52*(1), 373–380. https://doi.org/10.1111/are.14900

Albers, T., Dinh Cong San, & Schmitt, K. (2013). Coastal Protection in the Lower Mekong Delta, 124. www.giz.de/en

Haage, S. S. (2018). Wave Flume Experiments on Permeable Structures, 1–127. http://repository.tudelft.nl/.

Morison, J., Johnson, J., & Schaaf, S. (1950). The Force Exerted by Surface Waves on Piles. *Journal of Petroleum Technology*, *2*(05), 149–154. https://doi.org/10.2118/950149-g

Sumer, D., B. Mutlu (Technical Unversity of Denmark, & Fredsoe, D., Jorgen (Technical Unversity of Denmark. (2006). *Hydrodynamics around cylindrical structures* (Revised Ed, Vol. 26). World Scientific Publishing Co. Pte. Ltd. https://doi.org/10.1016/s0378-3839(97)00031-8

Keulegan, G. H., & Carpenter, L. H. (1958). Forces on Cylinders and Plates in an Oscillating Fluid. *Journal of Research of the National Bureau of Standards*, *60*(75 -APMW-27).

Etminan, V., Lowe, R. J., & Ghisalberti, M. (2019). Canopy resistance on oscillatory flows. *Coastal Engineering*, *152*(November). https://doi.org/10.1016/j.coastaleng.2019.04.014

Gijón Mancheño, A., Jansen, W., Winterwerp, J. C., & Uijttewaal, W. S. J. (2021). Predictive model of bulk drag coefficient for a nature-based structure exposed to currents. *Scientific Reports*, *11*(1). https://doi.org/10.1038/s41598-021-83035-0

Suzuki, T., Hu, Z., Kumada, K., Phan, L. K., & Zijlema, M. (2019). Non-hydrostatic modeling of drag, inertia and porous effects in wave propagation over dense vegetation fields. *Coastal Engineering*, *149*(135), 49–64. https://doi.org/10.1016/j.coastaleng.2019.03.011

Mendez, F. J., & Losada, I. J. (2004). An empirical model to estimate the propagation of random breaking and nonbreaking waves over vegetation fields. *Coastal Engineering*, *51*(2), 103–118. https://doi.org/10.1016/j.coastaleng.2003.11.003

Suzuki, T., Zijlema, M., Burger, B., Meijer, M. C., & Narayan, S. (2012). Wave dissipation by vegetation with layer schematization in SWAN. *Coastal Engineering*, *59*(1), 64–71. https://doi.org/10.1016/j.coastaleng.2011.07.006

Phan, K. L., Stive, M. J., Zijlema, M., Truong, H. S., & Aarninkhof, S. G. (2019). The effects of wave non-linearity on wave attenuation by vegetation. *Coastal Engineering*, *147*(January), 63–74. https://doi.org/10.1016/j.coastaleng.2019.01.004

Dao, T., Stive, M. J., Hofland, B., & Mai, T. (2018). Wave Damping due to Wooden Fences along Mangrove Coasts. *Journal of Coastal Research*, *34*(6), 1317–1327. https://doi.org/10.2112/JCOASTRES-D-18-00015.1

Tas, S. A., van Maren, D. S., & Reniers, A. J. (2020). Observations of cross-shore chenier dynamics in Demak, Indonesia. *Journal of Marine Science and Engineering*, *8*(12), 1–18. https://doi.org/10.3390/jmse8120972

Smits, B. (2016). Morphodynamic optimisation of the design of semi-permeable dams for rehabilitation of a mangrove-mud coast.

Hu, Z., Suzuki, T., Zitman, T., Uittewaal, W., & Stive, M. (2014). Laboratory study on wave dissipation by vegetation in combined current-wave flow. *Coastal Engineering*, *88*(June), 131–142. https://doi.org/10.1016/j.coastaleng.2014.02.009

Borsje, R. M. (2018). Assessing current patterns behind hybrid dams, 79.

Siddal, S. E. (1980). A clarification of the genus Perna (Mytiliidae). *Bulletin of marine science*, *30*(4), 858–890.

Soon, T. K., & Ransangan, J. (2014). A Review of Feeding Behavior, Growth, Reproduction and Aquaculture Site Selection for Green-Lipped Mussel, Perna viridis. *Advances in Bioscience and Biotechnology*, *05*(05), 462–469. https://doi.org/10.4236/abb.2014.55056

Rajagopal, S., Venugopalan, V. P., Nair, K. V., Van Der Velde, G., Jenner, H. A., & Den Hartog, C. (1998). Reproduction, growth rate and culture potential of the green mussel, Perna viridis (L.) in Edaiyur backwaters, east coast of India. *Aquaculture*, *162*(3-4), 187–202. https://doi.org/10.1016/S0044-8486(98)00166-5

Soon, T. K., & Ransangan, J. (2016). Feasibility of green mussel, Perna viridis farming in Marudu Bay, Malaysia. *Aquaculture Reports*, *4*, 130–135. https://doi.org/10.1016/j.aqrep.2016.06.006

Sallih, K. B. (2005). Mussel Farming in the State of Sarawak, Malaysia: A Feasibility Study.

Theophanatos, A. (1988). Marine Growth and the Hydrodynamic Loading of Offshore Structures. (February), 276.

Plew, D. R., Enright, M. P., Nokes, R. I., & Dumas, J. K. (2009). Effect of mussel bio-pumping on the drag on and flow around a mussel crop rope. *Aquacultural Engineering*, *40*(2), 55–61. https://doi.org/10.1016/j.aquaeng.2008.12.003

Van Bijsterveldt, v. d. W. D. G. M. A. F. G. H. M., C., & Bouma, T. (2021). Can cheniers protect mangroves along eroding coastlines? – a study investigating the effect of different fore-shores on long-term stability of mangroves. *Coastal Engineering (under review)*.

Holthuijsen, L. H. (2007). *Waves in oceanic and coastal waters* (2009th ed.). Cambridge University Press.

Van den Bos, H., J.P.; Verhagen. (2018). *Breakwater design - lecture notes cie 5308* (2018th ed.).

Fenton, J. D. (1988). The numerical solution of steady water wave problems. *Computers and Geosciences*, *14*(3), 357–368. https://doi.org/10.1016/0098-3004(88)90066-0

Goda, Y., & Suzuki, Y. (1976). Estimation of incident and reflected waves in regular wave experiments. *Coastal Engineering*, *22*(1), 828–845. https://doi.org/10.1016/0029-8018(93)E0011-G

Mansard, E. P. D., & Funke, E. R. (1980). The measurement of incident and reflected spectra using a least squares method, 154–172.

Zelt, J. A., Skjelbreia, J. E., & Wave Technologies. (1993). Estimating incident and reflected wave fields using an arbitrary number of wave gages. *Proceedings of the Coastal Engineering Conference*, *1*, 777–788. https://doi.org/10.1061/9780872629332.058

Dean, D. R. A., Robert G. (1984). *Water wave mechanics for engineers and scientists* (1998th ed.). World Scientific Publishing Co. Pte. Ltd.

Dekkers, J. M. (2018). Undular bore development over coral reefs An experimental study. http://repository.tudelft.nl/.

Hughes, S. A. (1993). Laboratory wave reflection analysis using co-located gages. *Coastal Engineering*, *20*(3-4), 223–247. https://doi.org/10.1016/0378-3839(93)90003-Q

Guza, R. T., & Thornton, E. B. (1980). Local and shoaled comparisons of sea surface elevations, pressures, and velocities. *Journal of Geophysical Research*, *85*(C3), 1524. https://doi.org/10.1029/jc085ic03p01524

Chakrabarti, S. K. (1982). Hydrodynamic coefficients for a vertical tube in an array. *in: Dynamic Analysis of Offshore Structures: Recent Developments, C.L. Kirk, Southampton, U.K., C.M.L. Publications Ltd., 198*, *1) (ISBN*(1), 70–80.

Battjes, J. A., & Groenendijk, H. W. (2000). Wave height distributions on shallow foreshores. *Coastal Engineering*, *40*, 161–182.

Ningsih, N., Suryo, W., & Anugrah, S. (2011). Study on Characteristics of Residual Water Level in Jakarta, Semarang, and Surabaya Waters–Indonesia and Its Relation to Storm Events in November. *J Basic & App Sci*, *11*(5), 31–37. http://scholar.google.com/scholar?hl=en&btnG=Search&q=intitle:Study+on+Characteristics+of+Residual+Water+Level+in+Jakarta+,+Semarang+,+and+Surabaya+Waters+?+Indonesia+and+Its+Relation+to+Storm+Events+in+November+2007#0

Suroso, D. S. A., & Firman, T. (2018). The role of spatial planning in reducing exposure towards impacts of global sea level rise case study: Northern coast of Java, Indonesia. *Ocean and Coastal Management*, *153*(June 2017), 84–97. https://doi.org/10.1016/j.ocecoaman.2017.12.007

Hinkel, J., & Klein, R. J. (2009). Integrating knowledge to assess coastal vulnerability to sea-level rise: The development of the DIVA tool. *Global Environmental Change*, *19*(3), 384–395. https://doi.org/10.1016/j.gloenvcha.2009.03.002

Herman, P. (2021). Private communication.

Muis, S., Verlaan, M., Winsemius, H. C., Aerts, J. C., & Ward, P. J. (2016). A global reanalysis of storm surges and extreme sea levels. *Nature Communications*, *7*(May). https://doi.org/10.1038/ncomms11969

Borsje, R. M. (2019). Wave-Driven Set-Up of Fluid Mud, 100.

Balke, T., Bouma, T. J., Horstman, E. M., Webb, E. L., Erftemeijer, P. L., & Herman, P. M. (2011). Windows of opportunity: Thresholds to mangrove seedling establishment on tidal flats. *Marine Ecology Progress Series*, *440*, 1–9. https://doi.org/10.3354/meps09364

Rees, F. V. (2019). Mangrove ' s anchorage beyond opportunity. (August).

Dao, H. T., Hofland, B., Suzuki, T., Stive, M. J. F., Mai, T., & Tuan, L. X. (2021). Numerical and small-scale physical modelling of wave transmission by wooden fences. *1*, 1–19.

A

Appendix: distributions

The probability of exceedance for the Generalised Paretro distribution is the following:

$$Q = (1 + \alpha \frac{H - \gamma}{\beta})^{-1/\alpha} \tag{A.1}$$

With the inverse as:

$$H = \gamma + \beta \frac{Q^{-\alpha} - 1}{\alpha} \tag{A.2}$$

The linear regression of the inverse is in the form of:

$$H = A + B \frac{Q^{-\alpha} - 1}{\alpha} \tag{A.3}$$

The probability of exceedance of the Exponential distribution is the following:

$$Q = \exp(-\frac{H - \gamma}{\beta}) \tag{A.4}$$

The probability of exceedance of the Weibull distribution is the following:

$$Q = \exp(-\frac{H - \gamma}{\beta}) \tag{A.5}$$

The probability of exceedance of the Gumbel distribution is the following:

$$Q = 1 - \exp(-\exp(-\frac{H - \gamma}{\beta})) \tag{A.6}$$

These equations use the following parameters:

- Q is the probability of exceedance
- H, the wave height in m
- α is a shape parameter
- β is the slope
- γ is the point of interception in case of Q =1
- A and B are fitted parameters of the true parameters β and γ

The Exponential and Gumbel distribution have two parameters, A and B, which can be found by a linear regression. For the Weibull and General Paretro distributions have an additional parameter, α, thus a simple linear regression can not be applied only. Therefore the parameters A and B are fitted based on linear regression and α is guessed, this is than done in an iterative approach to lead to the lowest RMSE possible with the dataset.

B

Appendix: Extra results SWASH - experiments Jansen (2019)

Empty flume

To make sure the waves are well modelled before we implement structures in SWASH, the wave propagation is checked along an 'empty' flume in SWASH. This is shown in Figures B.1 to B.4. Table B.1 shows the different amplitudes that have been used to implement the waves by either Stokes' theory or the streaming theory of Fenton (1988).

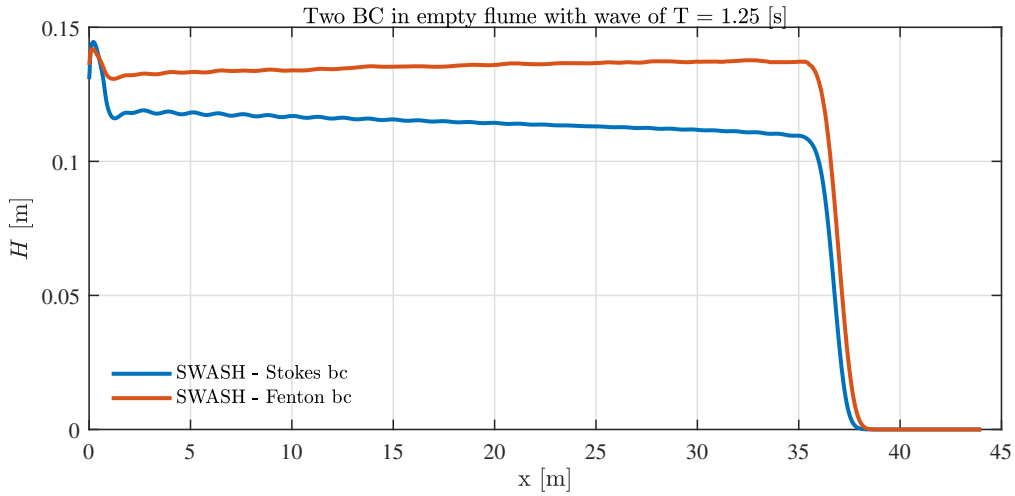

Figure B.1: The results of two BC for the simulation of T =1.25 s and H = 0.13m

T	H	Stokes:	a1	a2	Fenton	a1	a2	a3	a4
[s]	[cm]		[cm]	[cm]		[cm]	[cm]	[cm]	[cm]
1	0.13		6.5	0.94		6.28	0.95	0.22	0.05
1.25	0.13		5.8	0.67		6.35	0.85	0.15	0.03
1.5	0.13		5.8	0.73		6.34	0.92	0.16	0.03
1.75	0.13		5.7	0.83		6.31	1.06	0.19	0.035
2	0.13		5.8	1.1		6.26	1.24	0.24	0.05
3	0.13					5.84	2.05	0.66	0.17

Table B.1: The amplitudes that are used in applying the theories of Stokes and Fenton

In Figures B.5 and B.6 the results of using the different theories are shown, and as can be seen the results hardly differ.

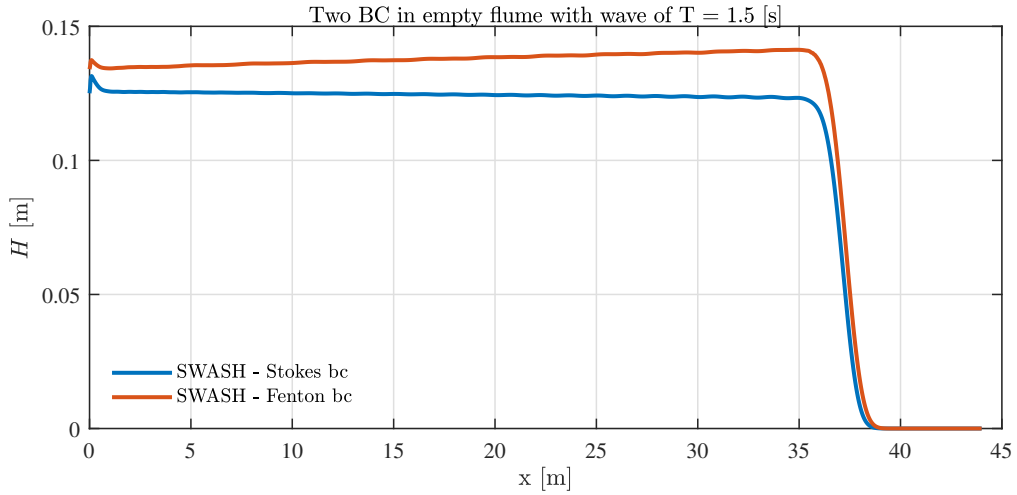

Figure B.2: The results of two BC for the simulation of T =1.5 s and H = 0.13m

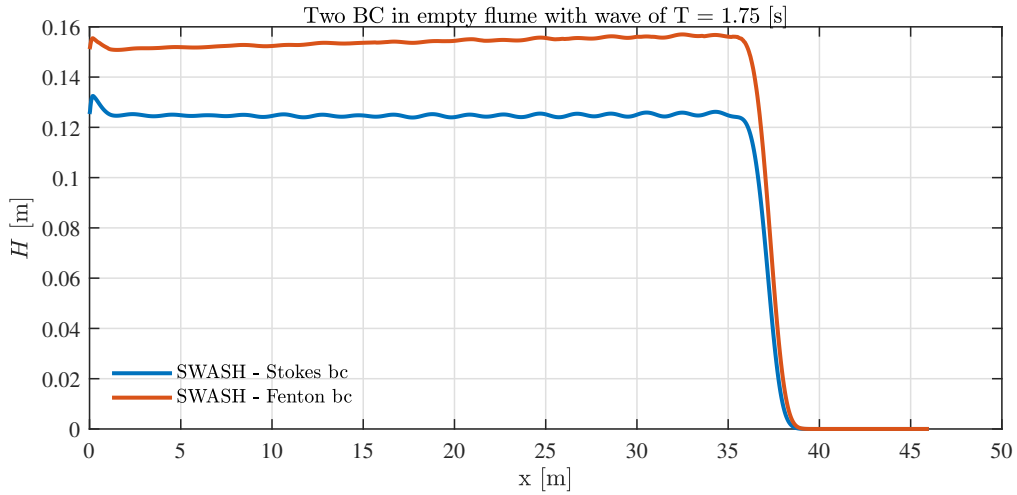

Figure B.3: The results of two BC for the simulation of T =1.75 s and H = 0.13m

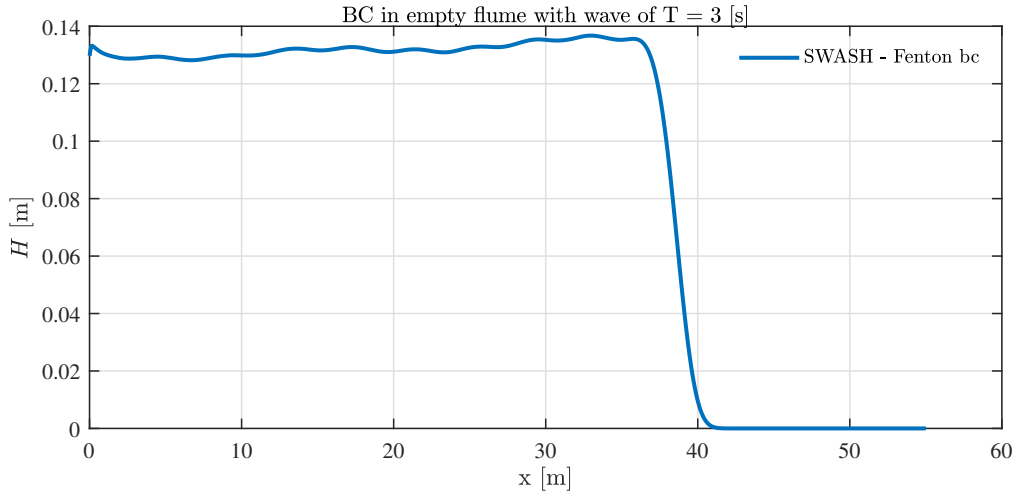

Figure B.4: The results of using Fenton (1988) streaming theory as BC for the simulation of T =3 s and H = 0.13m

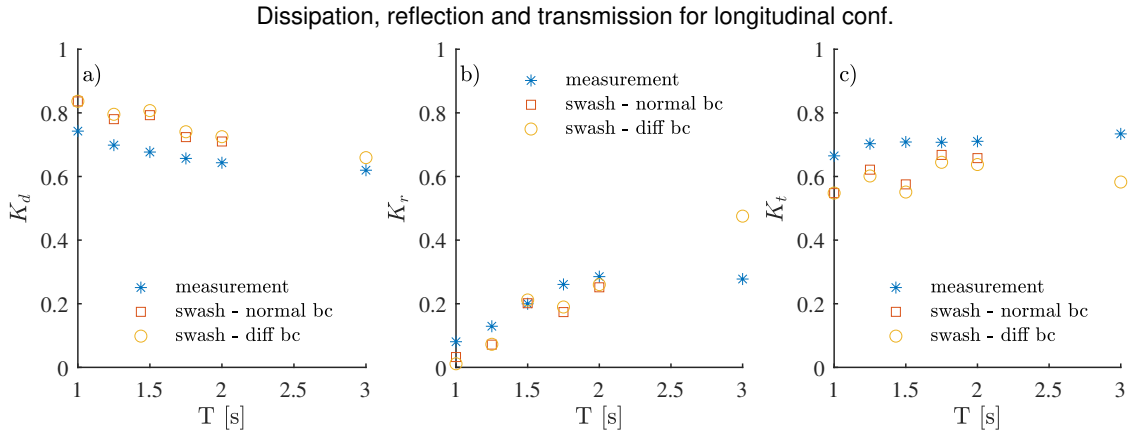

Figure B.5: Results of the longitudinal configuration for two different theories to generate the BC

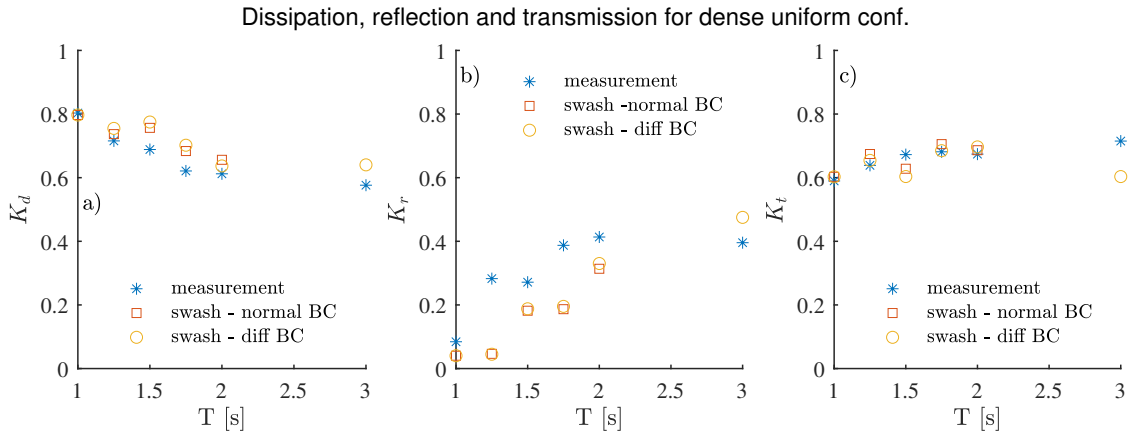

Figure B.6: Results of the uniform dense configuration for two different theories to generate the BC

Reflection at the back of the flume

Figure B.7 shows the reflection at the end of the flume in SWASH and the physical flume. The comparison is not so accurate, for the wave periods of T = 1 to 1.5 s SWASH lower values which is good and indicates that the sponge layer dampens the waves effectively. For the case of T = 1.75 to 3 s SWASH shows higher reflection rates, which is undesirable. Thus a longer sponge layer is used to check if this works betters and in combination with a radiation boundary. However, even when the spongelayer length is changed from 3 times the wavelength to 5 times the wavelength, the reflection coefficient for T =3 s is still 0.11. Another cause of the high reflection rate could be the non linearity of the waves, however in section 4.3 it can be seen that Goda and Suzuki (1976) should predict very close to the exact rate and would give thus a lower reflection than the value of 0.11.

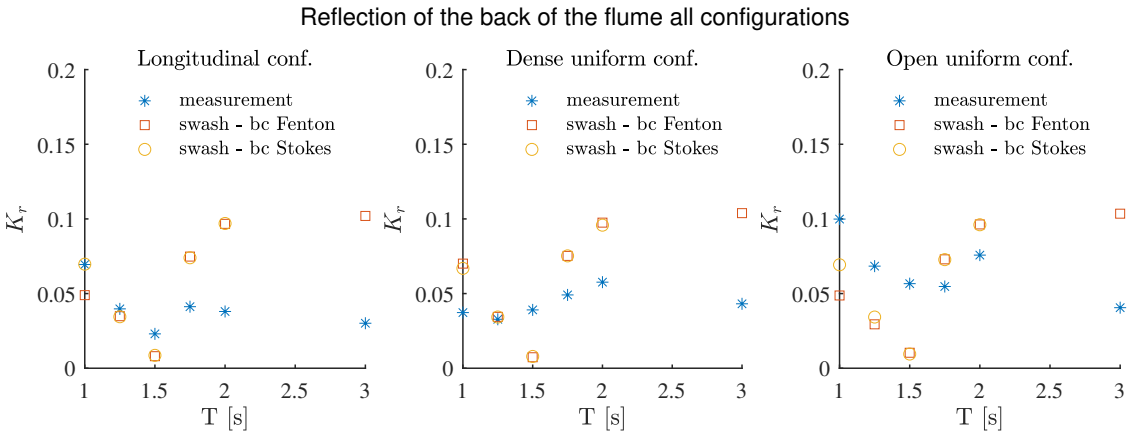

Figure B.7: Reflection rates for two boundary conditions, Stokes'theory or Fenton (1988), for: left) Longitudinal conf., middle) dense uniform conf. and right) open uniform conf.

Overview of runs

In Table B.2 the different cases that have been used for the four configurations from Jansen (2019) experiments.

Cases	Longitudinal	Uniform dense	Uniform open	Single row	no structure
BC by Stokes'	X	X	X	-	X
BC by Fenton (1988)	X	X	X	X	X
N_{stems} average(as one block), porosity off	X	X	X	X	-
N_{stems} locally increased, porosity off	X	-	-	-	-
$C_d = C_{d,s}$	X	X	X	-	-
$C_d = C_{d,b} = C_{d,s}(f_b f_s f_{KC})^3$, porosity off	X	X	X	X	-
$C_d = C_{d,b} = C_{d,s}(f_s f_{KC})^3$, porosity on	X	-	-	X	-
$C_d = C_{d,b} = C_{d,s}(f_b f_s f_{KC})^3 n^2$, porosity on	X	-	-	-	-
$C_d = C_{d,s}(f_b f_s f_{KC})^2$	X	X	-	-	-
Longer sponge layer	-	-	-	X	
Increased amount of vertical layers	X	-	-	-	-

Table B.2: Overview of case per configuration from the experiments of Jansen (2019)

C

Appendix: Calibration of SWAN

In Figure C.1 the depth that SWAN computes is shown with respect to the measurements, the measurements are used as input for the still water level in SWAN. The mean water depth is 1.3 m MSL, so the difference to this water level is used as input in SWAN. For instance a 1st December 00:00, the extra water levels 0.22 m. SWAN also computes the setup by wind so therefore the measurements and output from SWAN do not align perfectly.

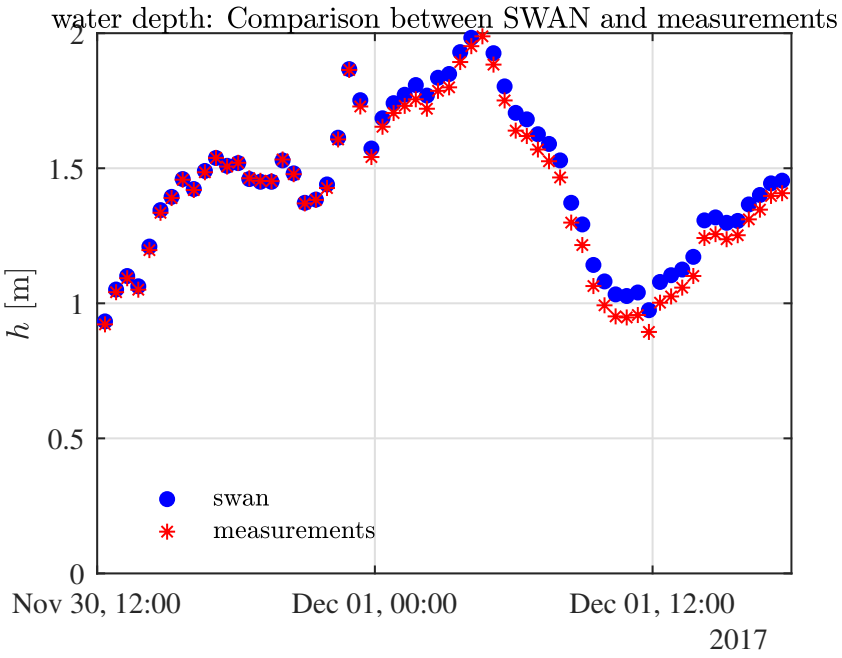

Figure C.1: Depth by SWAN and according to measurements during storm 1 December

Figures C.2 to C.5 are used for the calibration of the following parameters in Section 3.3:

- wind velocity U10
- directional spreading
- breaking parameter γ along with the proportionality parameter α

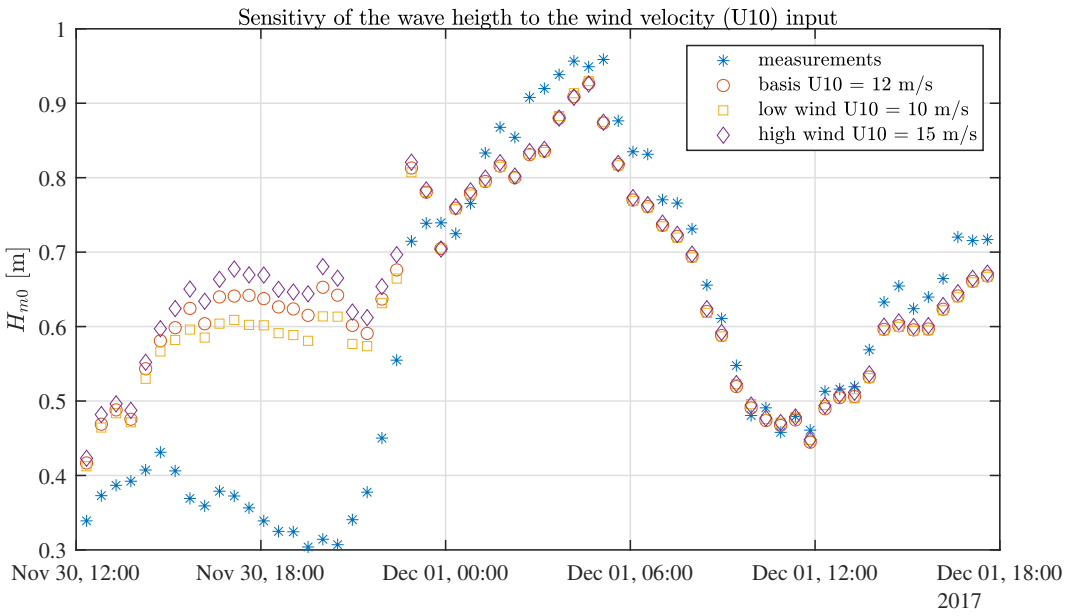

Figure C.2: Sensitivity to wind velocity U10, for three different wind velocities: U10 = 10,12 and 15 m/s

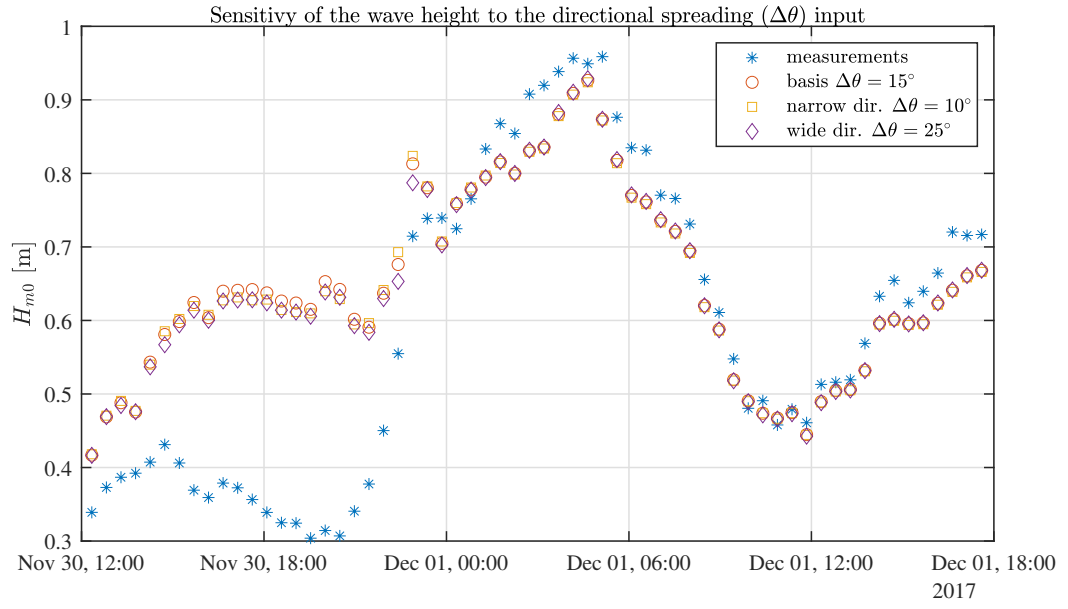

Figure C.3: Sensitivity to directional spreading of the waves, for three different angles: $\Delta\theta$=10,15 and 25 °

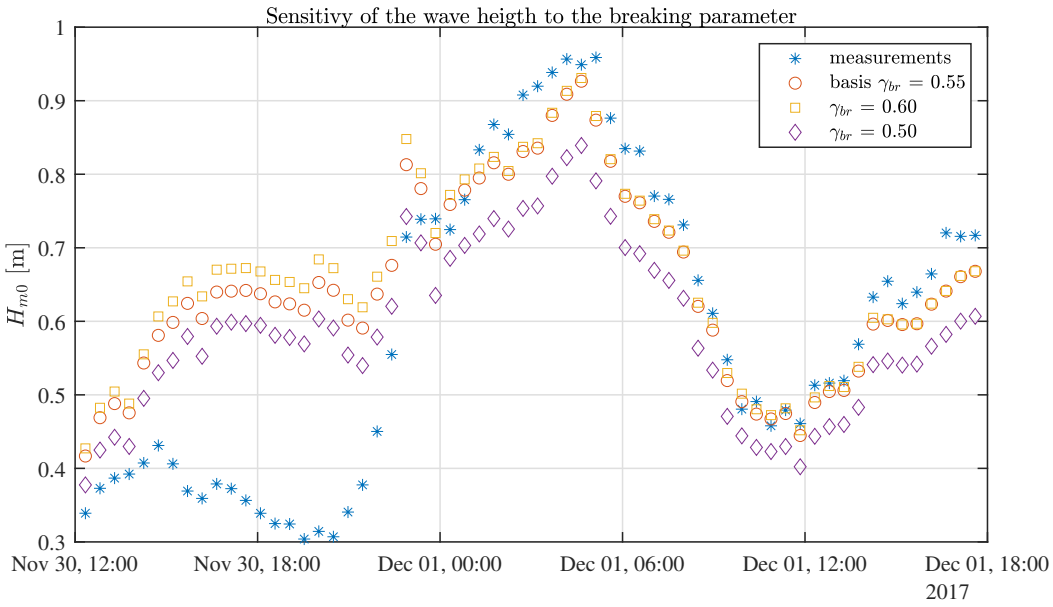

Figure C.4: Sensitivity to breaking parameter γ, γ = 0.5, 0.55 and 0.6

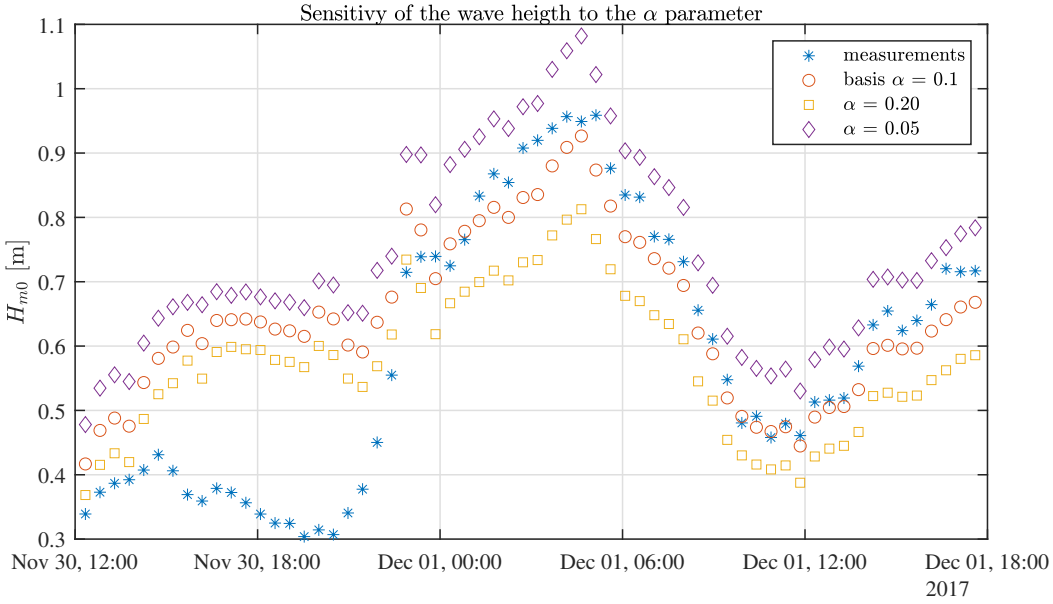

Figure C.5: Sensitivity to proportionality parameter α = 0.05,0.1 and 0.2

D

Appendix:Processing methods

D.1. Method of Goda and Suzuki, 1976

Goda and Suzuki (1976) requires that the separation between the wave gauges is in the range of $\Delta l = 0.05 - 0.45L$ with an optimum of L/4. Where L is the wave length of the regular wave. The incident and reflective wave can be described by the general form:

$$\eta_i = a_i cos(kx - \sigma t + \varepsilon_i) \tag{D.1}$$

$$\eta_r = a_r cos(kx + \sigma t + \varepsilon_r) \tag{D.2}$$

The total surface elevation at the two wave gauges can then be described as the sum of the super positioning of the incoming and reflected surface elevations:

$$\eta_1 = \eta_i + \eta_r = A_1 cos(\sigma t) + B_1 sin(\sigma t) \tag{D.3}$$

$$\eta_2 = \eta_i + \eta_r = A_2 cos(\sigma t) + B_2 sin(\sigma t) \tag{D.4}$$

Where:

$$A_1 = a_i cos(\phi_i) + a_r cos(\phi_r) \tag{D.5}$$

$$B_1 = a_i sin(\phi_i) - a_r cos(\phi_r) \tag{D.6}$$

$$A_2 = a_i cos(k\Delta l + \phi_i) + a_r cos(k\Delta l + \phi_r) \tag{D.7}$$

$$B_2 = a_i sin(k\Delta l + \phi_i) - a_r sin(k\Delta l + \phi_r) \tag{D.8}$$

$$\phi_i = kx_1 + \varepsilon_i \tag{D.9}$$

$$\phi_r = kx_1 + \varepsilon_r \tag{D.10}$$

The equation D.3 to D.10 can then be solved to get a_i and a_r

D.2. Method of Mansard and Funke, 1980

For the method of Mansard and Funke, 1980 a script is written. The waves at the wave gauges can be described as a summation of discrete Fourier components, where for wave gauge 1 the signal is described as the following:

$$\eta_x 1(t) = \sum n = 1^N A_{i,n} cos(-\frac{2 * \pi * t}{T_n} + k_n x_1 + \phi_{i,n}) + A_{r,n} cos(-\frac{2 * \pi * t}{T_n} + k_n (x_1 + 2x_{r,1}) + \phi_{r,n}) + \Omega(t) \tag{D.11}$$

Where:

- η is the water elevation
- $A_{i,n}$ and $A_{r,n}$ are the wave amplitude of the incoming and reflected wave for the n-th harmonic

- t is the time
- T_n is the wave period of the n-th harmonic
- k_n is the wave number of the n-th harmonic
- ϕ is the phase of the incoming and reflective wave for the n-th harmonic
- x_1 is the location of the wave gauge 1 and x_{r1} is the distance between the structure and wave gauge 1
- Ω is the cumulative effect of all the corrupting signals.

Where for the other wave gauges the phase angle for the incoming wave changes to:

$$(-\frac{2\pi t}{T_n} + k_n(x_1 + x_{1,2}) + \phi_{in,} \tag{D.12}$$

and for the reflected wave to:

$$(-\frac{2\pi t}{T_n} + k_n(x_1 + 2(x_{r,1} - x_{1,2}) + \phi_{r,n} \tag{D.13}$$

The Fourier coefficient and their exponents are obtained by Fourier transform of η for $0 \leq t \leq T$ than they can be given in the polar form: $B_{1,n} = A_{1,n} \exp i\alpha_{1,n}$

The Fourier transform of the η_1 gives than:

$$B_{1,n} = A_{i,n} \exp ik_n x_1 + iphi_n + A_{r,n} \exp ik_n(x_1 + 2x_{r,1} + iphi_{r,n} + \gamma_n \exp i_n \tag{D.14}$$

This can than be rewritten to:

$$B_{1,n} = Z_{i,n} + Z_{r,n} + Z_{N,1,n} \tag{D.15}$$

This can be also done for the other measured signals and incorporating the different phase signals as in equation x. This results then in a system of equations with as variables the following terms:

It can then be restated to:

$$Z_{i,n} + Z_{r,n} - B_{1,n} = \varepsilon_{1,n} \tag{D.16}$$

Where $\varepsilon_{1,n} = -Z_{N,1} + f_e(Z_{i,n}, Z_{r,n}$ With a least squares method the values of $Z_{i,n}$ and $Z_{r,n}$ can be found for which $f_e(Z_{i,n}, Z_{r,n})$ results in a minimum (=0).

$$\sum_{p=1}^{3} (\varepsilon_{p,n}^2 = \sum_{p=1}^{3} (Z_{i,n} \exp i\psi_{p,n} + Z_{r,n} \exp -i\psi_{p,n} - B_{p,n})^2 = \text{a minimum} \tag{D.17}$$

It is assumed that this minimum is reached when the partial derivatives are zero:

$$\frac{d(\sum_{p=1}^{3}(\varepsilon_{p,n})^2}{dZ_{i,n}} = \frac{d(\sum_{p=1}^{3}(\varepsilon_{p,n})^2}{dZ_{r,n}} = 0 \tag{D.18}$$

This results in expressions for $Z_{i,n}$:

$$Z_{i,n} = \frac{1}{D_n}(B1, n(R1 + iQ1) + B_{2,n}(R2 + iQ2) + B_{3,n}(R3 + iQ3)) \tag{D.19}$$

and for $Z_{r,n}$:

$$Z_{r,n} = \frac{1}{D_n}(B1, n(R1 - iQ1) + B_{2,n}(R2 - iQ2) + B_{3,n}(R3 - iQ3)) \tag{D.20}$$

Where:

$$D_n = 2 * (sin^2(\beta_n) + sin^2(\gamma_n) + sin^2(\gamma_n - \beta_n)) \tag{D.21}$$

$$R1 = sin^2(\beta_n) + sin^2(\gamma_n) \tag{D.22}$$

$$Q1 = sin(\gamma_n) * cos(\beta_n) + sin(\gamma_n) * cos(\gamma_n) \tag{D.23}$$

$$R2 = sin(\gamma_n) * sin(\gamma_n) * cos(\gamma_n) \tag{D.24}$$

$$Q2 = sin(\gamma_n) * cos(\gamma_n - \beta_n) - 2sin(\beta_n) \tag{D.25}$$

$$R3 = -sin(\beta_n) * sin(\gamma_n - \beta_n) \tag{D.26}$$

$$Q3 = sin(\beta_n) * cos(\gamma_n - \beta_n) - 2sin(\gamma_n) \tag{D.27}$$

$$\beta_n = k_n x12 \tag{D.28}$$

$$\gamma_n = k_n x13 \tag{D.29}$$

So the following steps are taken:

- Fourier transform all the signals to obtain the amplitude spectra, where in this case the peak of the spectrum is assumed to belong with the given wave period.
- determine the cross spectral density spectrum for η_1 and η_2, and for η_1 and η_3. This can be done with the function *cspd* in Matlab
- determine the relative phase spectra of wave gauges 2 and 3 with respect to the signal of wave gauge 1 in such that the coherence between the signals is at least 95 % . This last value is arbitrary but is assumed that such a level is appropriate.
- pair up the amplitudes and relative phase angles in polar form
- determine Z_i and Z_r
- $K_r = (Z_i)/(Z_r)$

D.3. Method of Hughes (1993) and Dekkers (2018)

Based on these assumptions, the total surface can then be approximated as the following:

$$\zeta = \zeta^+_{primary} + \sum_{n=2}^{N} \zeta^+_{n,bound} + \sum_{n=2}^{N} \zeta^-_{n,free} \tag{D.30}$$

Where:

- ζ^+ is the incident wave
- ζ^- is the reflected wave

As the incident waves are a sum of bound waves, the wave number k_n^+ for a certain frequency f_n is different than for the reflected free waves k_n^-. k_n^+ is a multiple of the primary wave, while for the reflected free waves k_n^- is determined by the linear dispersion relation.

The waves can be separated assuming linear superposition:

$$\zeta - \bar{\zeta} = \zeta^+ + \zeta^- \tag{D.31}$$

$$Q - \bar{Q} = Q^+ + Q^- \tag{D.32}$$

Where:

- ζ is the water level elevation
- Q is the discharge, as: $Q = c\zeta$

The Equations D.31 and D.32 lead then to expressions for ζ^+ and ζ^-:

$$\zeta^+ = \frac{Q - c^-\zeta}{c^+ - c^-} \quad \text{and} \quad \zeta^- = \frac{Q - c^+\zeta}{c^- - c^+} \tag{D.33}$$

Suppose $K^\pm$ is the velocity response function in such that

$$Q^+ = K^+ u \quad \text{and} \quad Q^- = K^- u^- \tag{D.34}$$

Where K for a linear wave is :

$$K = \frac{cosh(k(d+z)}{cosh(kd)} \tag{D.35}$$

and for a cnoidal wave is :

$$K = Q/u = \frac{sinh(k(d+z)}{kcosh(k(d+z))} \tag{D.36}$$

When combined with equations x,y z gives the following result for ζ^+ and ζ^-:

$$\zeta^+ = \frac{u - \frac{c^-}{K^-}\zeta}{\frac{c^+}{K^+} - \frac{c^-}{K^-}} = \frac{K^- u - c^-\zeta}{c^+\frac{K^-}{K^+} - c^-} \tag{D.37}$$

and

$$\zeta^- = \frac{u - \frac{c^+}{K^+}\zeta}{\frac{c^-}{K^-} - \frac{c^+}{K^+}} = \frac{K^+ u - c^+\zeta}{c^-\frac{K^+}{K^-} - c^+} \tag{D.38}$$

As K^+ is now depended on the free surface, the Fourier components cannot be be calculated directly in the frequency domain. The decomposition from a total surface to the separate components requires the following steps:

- De- trend the total free surface (and add $\bar{\zeta}$ to depth d).$\bar{Q}$ is assumed to be zero
- Fourier transform ζ and u
- Use the Inverse Fourier transform for each frequency to obtain timeseries of u and ζ
- Compute for each frequency the wave numbers, where k^+ is dependent on the cnoidal wave celerity c^+ and k^- is dependent on linear wave dispersion
- Compute the velocity response functions per frequency
- solve Equation in the time domain per frequency
- sum up the time series for each direction to get the total incident and reflected surface elevation

D.4. Evaluation of methods with different wave conditions

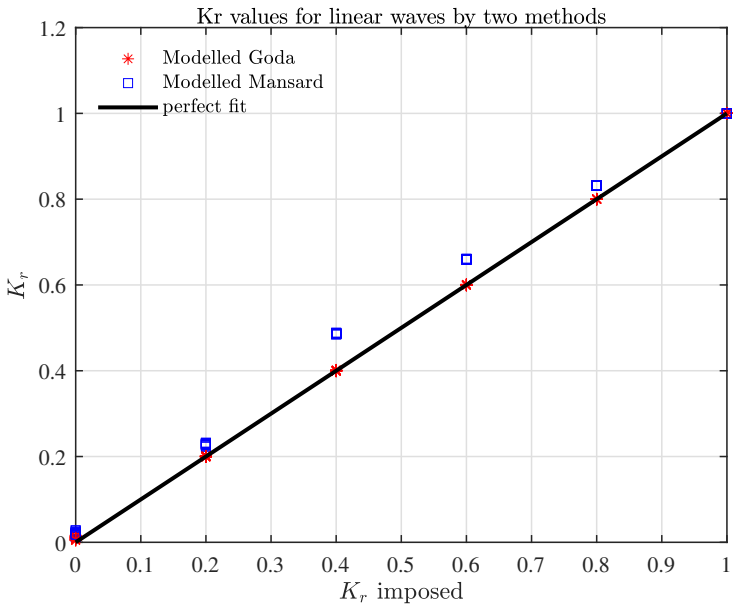

Figure D.1: Comparison for the case of linear waves between Goda and Suzuki (1976)and Mansard and Funke (1980)

Figure D.1 shows that for:

- $K_{r,i}$= 0, both methods perform well
- $K_{r,i}$= 0.2 up to 0.8 Mansard and Funke (1980) shows slightly higher values than the imposed value with highest difference at $K_{r,i}$= 0.4, wheres Goda and Suzuki (1976) shows the exact answer.
- $K_{r,i}$= 1, both methods perform well

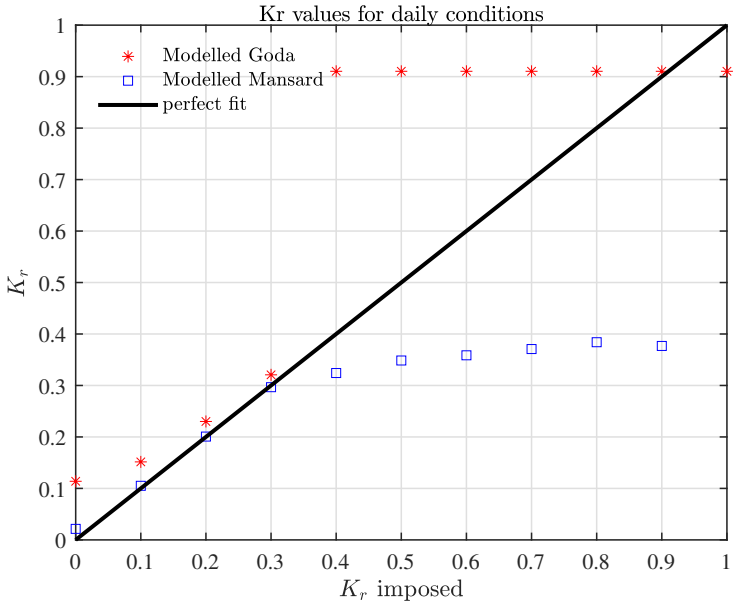

Figure D.2: Performance of Goda and Suzuki (1976) and Mansard and Funke (1980) for one of the daily wave conditions

Figure D.2 shows that for :

- K_r = 0 -0.3 Goda and Suzuki (1976) slightly overestimates the K_r values and Mansard and Funke (1980) has a good agreement with the imposed values

- K_r = 0.3 -1 Mansard and Funke (1980) and Goda and Suzuki (1976) do not follow the imposed values but stay between 0.3 - 0.4 and around 0.9 respectively.

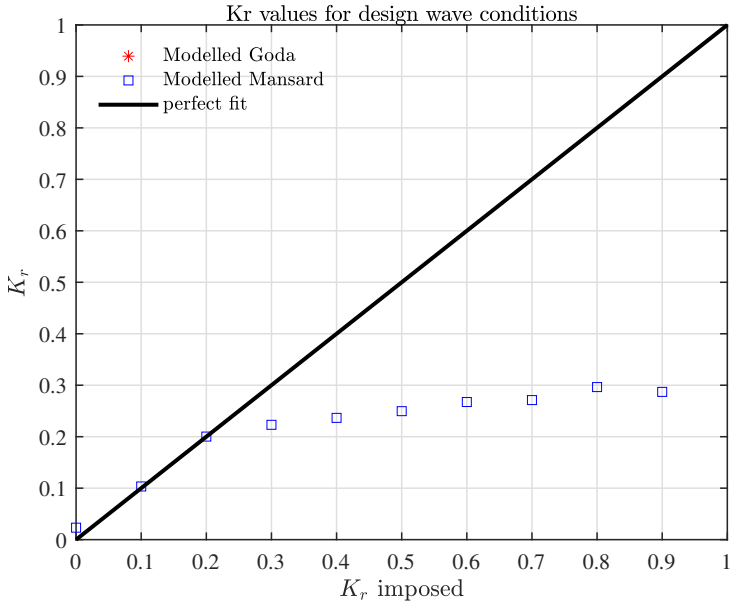

Figure D.3: Performance of Goda and Suzuki (1976) and Mansard and Funke (1980) for one of the storm wave conditions

Figure D.3 shows that for:

- K_r = 0 - 1 Goda and Suzuki (1976) is outside the range of the figure, the values are larger than 1.
- K_r = 0.0 -0.2 Mansard and Funke (1980) has a well comparison with the imposed K_r, however for higher imposed values the K_r does not follow the imposed K_r but stays between 0.2 and 0.3.

E

Appendix: Designs

E.1. Input SWASH

E.1.1. Performance of boundary condition

Figure E.1 shows the propagation of waves for the daily wave condition for the single fence design. At x = 5L, there are small bumps visible in the troughs of the waves, this is due to the interaction with the structure.

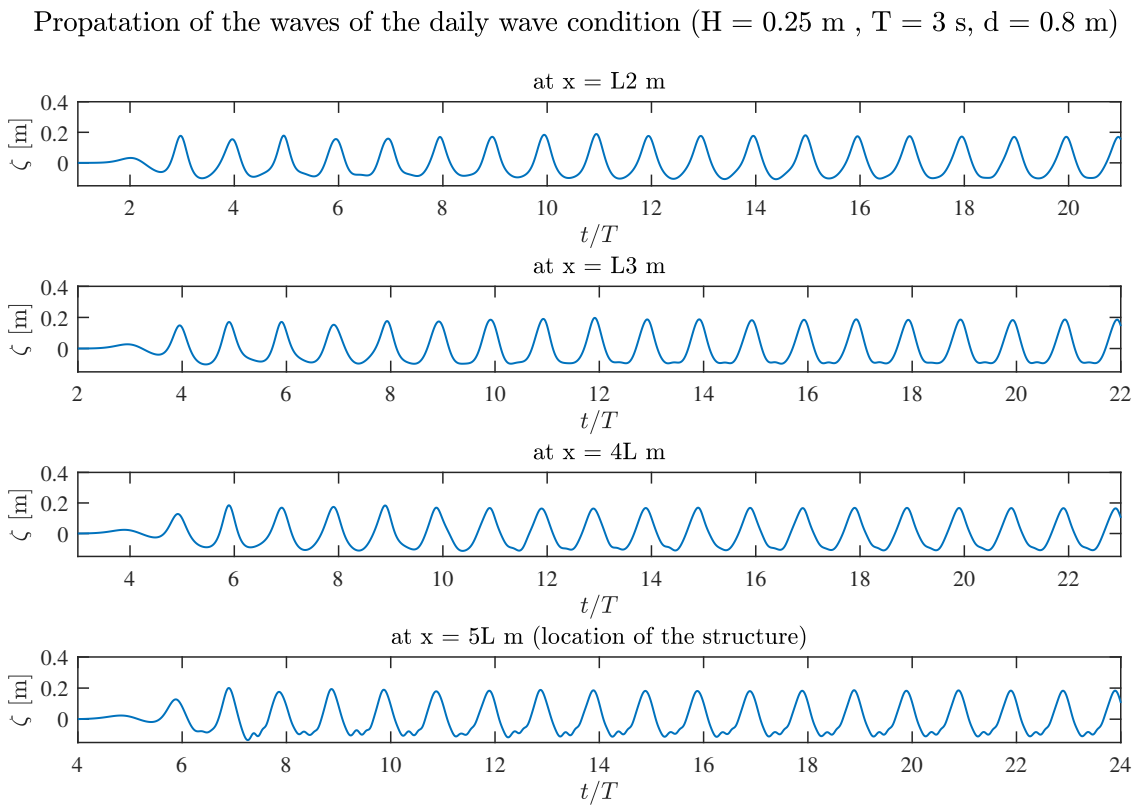

Figure E.1: The propagation of the waves of the daily wave condition and the interaction with the single fence design, along 4 locations: x = 2L, 3L, 4L, 5L.

n	T	omega	f	L	k	d	kd
units	[s]	[Hz]	[Hz]	[m]	[1/m]	[m]	[-]
1	3	2,094395	0,333333	7,9	0,79534	0,8	0,636272
2	1,5	4,18879	0,666667	3,2	1,963495	0,8	1,570796
3	1	6,283185	1	1,56	4,027683	0,8	3,222146

Table E.1: Reflected linear higher harmonics of the daily wave conditions.

n	T	omega	f	L	k	d	kd
units	[s]	[Hz]	[Hz]	[m]	[1/m]	[m]	[-]
1	6,88	0,913254	0,145349	29	0,216662	1,78	0,385658
2	3,44	1,826507	0,290698	12,92	0,486315	1,78	0,86564
3	2,293333	2,739761	0,436047	7,47	0,841123	1,78	1,497198
4	1,72	3,653015	0,581395	4,55	1,38092	1,78	2,458037
5	1,376	4,566268	0,726744	2,92	2,151776	1,78	3,830161
6	1,146667	5,479522	0,872093	2,03	3,095165	2,78	8,604559
7	0,982857	6,392776	1,017442				
8	0,86	7,306029	1,162791				
9	0,764444	8,219283	1,30814				
10	0,688	9,132537	1,453488				

Table E.2: Reflected linear higher harmonics of the wave conditions of 1 year.

n	T	f	ω	L	k	d	kd	c	$dx/(cT)$	$t = 10T_1 + ..T_n$	t/T_1
	[s]	[Hz]	[1/s]	[m]	[1/m]	[d]	[-]	[m/s]	[-]	[s]	[-]
1	7.47	0.133	0.84	32	0.19	1.91	0.375	4.28	7	127	17
2	3.73	0.267	1.68	14.68	0.43	1.91	0.82	3.39	15.25	131.7	17.63
3	2.49	0.401	2.52	8.57	0.73	1.91	1.40	3.44	26.13	139.8	18.72
4	1.87	0.534	3.36	5.29	1.19	1.91	2.27	2.83	42.34	153.8	20.58
5	1.94	0.669	4.20	3.46	1.82	1.91	3.47	2.31	64.74	171.42	22.94
6	1.24	0.803	5.04	2.4	2.61	1.91	5.00	1.93	93.33	190.9	25.56
7	1.06	0.93	5.88	1.75	3.59	1.91	10.44	1.64	128	211.29	28.28
8											
9											
10											

Table E.3: the primary wave and higher harmonics of the wave conditions with a return period of 5 year. dx in 9th column relates to the following distances: dx = 10- 3 L = 224 m

E.1.2. Drag coefficient - Double fence design

In Table E.4 are the drag coefficients and the distances between the two rows for the double fence design.

s_x	3 D	4 D	5 D	6 D	7 D	8 D	9 D	10 D
s_x [m]	0.42	0.56	0.70	0.84	0.98	1.12	1.26	1.4
$C_{d,b}$ (R = 1 & 5 yr)	3.30	4.28	4.95	5.43	5.79	6.08	6.30	6.49
$C_{d,b}$ (R = 0 yr)	3.75	4.86	5.63	6.18	6.59	6.91	7.17	7.38
s_x	$L_{rp1}/20$	$L_{rp1}/15$	$L_{rp1}/10$	$L_{rp1}/8$	$L_{rp1}/6$	$L_{rp1}/5$	$L_{rp1}/4$	$L_{rp1}/3$
s_x [m]	1.45	1.90	2.90	3.50	4.70	5.80	7.30	9.70
$C_{d,b}$ (rp1 & rp5)	6.49	6.92	7.37	7.55	7.74	7.85	7.94	8.04
$C_{d,b}$ Daily (rp0)	[-]	[-]	[-]	[-]	[-]	8.93	9.04	9.14
s_x	$L_{rp1}/2$	$\frac{2}{3}L_{rp1}$	$\frac{3}{4}L_{rp1}$	L_{rp1}				
s_x [m]	14.5	19.3	21.80	29.0				
$C_{d,b}$ (rp1 & rp5)	8.13	8.18	8.19	8.23				
$C_{d,b}$ Daily (rp0)	9.25	9.30	9.32	9.36				

Table E.4: Bulk drag coefficient for each s_x distance

E.2. Extra results

E.2.1. Mussel poles

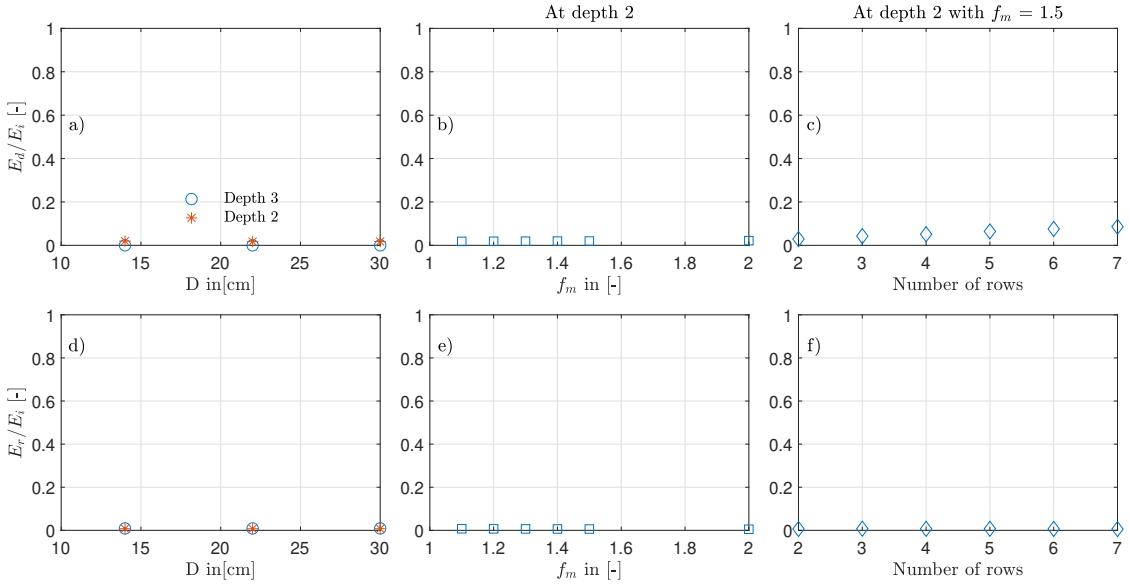

Figure E.2: Dissipation (a - c) and reflection (d - f) rates for the mussel poles for three situations: two depths, increased drag coefficient $C_d = C_d f_m$ and increasing number of rows.

In Figure E.2 it can be seen that the dissipation rates for all cases are negligible, only for an increasing number of rows with an increased drag coefficient by a factor f_m the dissipation rates are becoming visible. The reflection rates are in all cases negligible.

E.2.2. Double fence

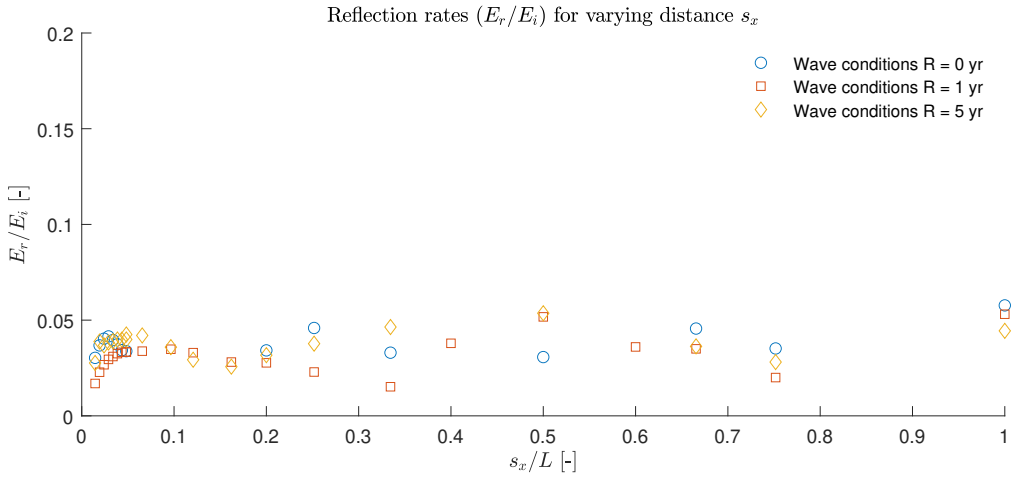

Figure E.3: Reflection rates for the double fence design, due to the low values the y axis is adjusted to a range between 0 -0.2 instead of 0-1

In Figure E.3 the reflection rates of the double fence are presented. It can be observed that

F

Appendix: Tidal water levels

The tidal water levels were analysed using the Matlab tool Utide from Codiga (2011). In Tables F.1 and F.2 the output of Utide is presented. The first three tidal coefficients are accurately predicted but the last one, O1, is not represented well.

Tidal constituents	A of Tas et al. (2020)	A by Utide	95% confidence A	Greenwhich phase lag	95 % confidence phase lag
Units	[m]	[m]	[m]	[°]	[°]
K1	0.22	0.228	0.00790	341	2.35
M2	0.10	0.132	0.00855	226	4.04
S2	0.08	0.0820	0.00928	121	5.55
O1	0.08	0.000645	0.00645	213	207

Table F.1: Results of Utide for the tidal signal along transect E1 for the four tidal constituents of Tas et al. (2020).

Tidal constituents	A of Tas et al. (2020)	A by Utide	95% confidence A	Greenwhich phase lag	95 % confidence phase lag
Units	[m]	[m]	[m]	[°]	[°]
K1	0.22	0.244	0.0115	308	2.44
M2	0.10	0.140	0.00856	178	3.33
S2	0.08	0.0881	0.00930	48.2	5.55
O1	0.08	0.0363	0.0113	202	17.7

Table F.2: Results of Utide for the tidal signal along transect A1 for the four tidal constituents of Tas et al. (2020).